THE DIJET CROSS SECTION MEASUREMENT IN PROTON-PROTON COLLISIONS AT A CENTER OF MASS ENERGY OF 500 GEV AT STAR

DISSERTATION

A dissertation submitted in partial
fulfillment of the requirements for
the degree of Doctor of Philosophy
in the College of Arts and Sciences
at the University of Kentucky

By
Grant Webb
Lexington, Kentucky

Director: Dr. Renee Fatemi, Professor of Physics
Lexington, Kentucky 2014

Copyright© Grant Webb 2014

ABSTRACT OF DISSERTATION

THE DIJET CROSS SECTION MEASUREMENT IN PROTON-PROTON COLLISIONS AT A CENTER OF MASS ENERGY OF 500 GEV AT STAR

Polarized deep inelastic scattering experiments play a vital role in the exploration of the spin structure of the proton. The polarized proton-proton collider at RHIC provides direct access to the gluon spin distribution through longitudinal double spin asymmetry measurements of inclusive jets, pions, and dijets. This thesis presents the measurement of the dijet double differential cross-section in proton-proton collisions at center of mass energies of $\sqrt{s} = 500$ GeV. The data represent an integrated luminosity of 8.7 pb^{-1} recorded by the STAR detector during the 2009 RHIC run. A comprehensive jet analysis was performed to determine the ideal jet algorithm and jet parameters used in $\sqrt{s} = 500$ GeV collisions at the STAR detector. The cross-section is measured as a function of the dijet invariant mass ($30 \leq M_{ij} \leq 152$ GeV) in the mid rapidity region with a maximum rapidity range of $|y_{max}| \leq 0.8$. This result shows agreement with theoretical next-to-leading order pQCD calculations, motivating the use of dijet asymmetries at STAR to further constrain the shape of $\Delta g(x)$.

KEYWORDS: Dijet Cross Section, Gluon Spin, STAR Detector, Jetography, Embedding

Author's signature: Grant Webb

Date: May 14, 2014

THE DIJET CROSS SECTION MEASUREMENT IN PROTON-PROTON COLLISIONS AT A CENTER OF MASS ENERGY OF 500 GEV AT STAR

By
Grant Webb

Director of Dissertation: Renee Fatemi

Director of Graduate Studies: Tim Gorringe

Date: May 14, 2014

ACKNOWLEDGEMENTS

I would like to thank Dr. Renee Fatemi, Dr. Capp Yess, Dr. Gene Van Buren, Dr. Stephen Trentalange, and Dr. Jerome Lauret for the motivation to be successful in my academic career. They have provided me with the knowledge and tools to allow me to pursue my career goals.

TABLE OF CONTENTS

Acknowledgements . . . iii

Table of Contents . . . iv

List of Figures . . . vii

List of Tables . . . ix

Chapter 1 Introduction . . . 1
1.1 The Spin on Life . . . 1
1.2 The Standard Model . . . 1
1.2.1 Fundamental Fermions and Bosons . . . 1
1.2.2 Fundamental Forces . . . 2
1.3 Quantum Chromodynamics . . . 4
1.3.1 Fragmentation and Hadronization . . . 6
1.3.2 Jets . . . 7
1.3.3 Underlying Event . . . 8
1.4 Parton Distribution Functions . . . 9
1.5 Polarized Parton Distribution Functions . . . 13
1.5.1 Gluon Spin . . . 16
1.5.2 Accessing the Gluon Spin . . . 19

Chapter 2 RHIC and The STAR Detector . . . 23
2.1 The Relativistic Heavy Ion Collider . . . 23
2.1.1 RHIC Layout . . . 23
2.1.2 Polarized Proton Injection . . . 24
2.1.3 Siberian Snakes . . . 25
2.1.4 Measuring Beam Polarization . . . 25
2.2 The STAR Detector . . . 27
2.2.1 Solenoidal Magnet . . . 29
2.2.2 Time Projection Chamber . . . 29
2.2.3 Space Charge and Grid Leak in the TPC . . . 33
2.2.4 The Time Of Flight and the pseudo Vertex Position Detector . 36
2.2.5 The Barrel Electromagnetic Calorimeter . . . 37
2.2.6 The EndCap Calorimeter . . . 38
2.2.7 Zero Degree Calorimeter . . . 38
2.2.8 Beam-Beam Counter . . . 42
2.3 Triggers . . . 43
2.4 Luminosity . . . 44

Chapter 3 Jet Algorithms . . . 48

3.1 Jet Definition . . . 48
3.2 Jet Algorithms . . . 48
3.2.1 An Ideal Algorithm . . . 49
3.2.2 Mid-Point Cone Jet Algorithm . . . 51
3.2.3 Anti-k$_T$ Jet Algorithm . . . 54
3.2.4 Comparison of Anti-k$_T$ and Mid-Point Cone Jet Algorithms . 55

Chapter 4 Dijets . . . 69
4.1 Event Selection . . . 69
4.1.1 Event-by-Event Quality Anaylsis . . . 69
4.2 Jet Quality Analysis . . . 72
4.3 Dijet Definition . . . 77
4.3.1 Two Leading p_T Jets . . . 77
4.3.2 p_T Thresholds . . . 78
4.3.3 BEMC Acceptance and Jet Rapidity y . . . 78
4.3.4 Neutral Energy Ratio and Background . . . 79
4.3.5 Vertex Requirement . . . 80
4.3.6 Back-to-Back Jets . . . 81
4.3.7 Triggered Jets . . . 81
4.3.8 Phase-Space . . . 81
4.3.9 Invariant Mass . . . 82
4.4 Monte Carlo Embedded Simulation . . . 82
4.4.1 Filters and their performance . . . 82
4.4.2 Filter Descriptions . . . 83
4.5 Environment . . . 84
4.6 Bias Tests . . . 84
4.7 Dijet Yields . . . 89
4.8 Data/Simulation Comparisons . . . 92
4.8.1 Vertex Re-weighting . . . 92
4.8.2 Jet Comparisons . . . 94
4.8.3 DiJet Comparisons . . . 95

Chapter 5 The Dijet Cross Section . . . 102
5.1 Unfolding . . . 102
5.1.1 Matching Dijets . . . 104
5.1.2 Bin-By-Bin Unfolding Methodology . . . 107
5.1.3 Iterative Bayesian Unfolding Methodology . . . 109
5.1.4 Singular Value Decomposition Methodology . . . 111
5.1.5 Unfolding Comparisons . . . 113
5.2 Dijet Cross Section . . . 116
5.3 Systematic Uncertainty . . . 119
5.4 Jetography . . . 121

Chapter 6 Conclusions . . . 124

Chapter 7 Appendix 126
7.1 Environment 126
7.1.1 GENERAL 126
7.1.2 Starsim Settings 126
7.1.3 BFC Settings 127
7.2 Error Calculations 127
7.2.1 Errors on an Inefficiencies 128

Bibliography 130

LIST OF FIGURES

1.1 The Standard Model . . . 2
1.2 Strong Coupling Constant at high Q . . . 5
1.3 Deep Inelastic Scattering . . . 6
1.4 The Underlying Event . . . 9
1.5 F_2^P VS Q^2 . . . 12
1.6 CT10NNL0 parton distribution functions . . . 13
1.7 g_1^P VS Q^2 . . . 15
1.8 Polarized Parton Distribution Functions . . . 17
1.9 P-P scattering . . . 18
1.10 Inclusive Jet A_{LL} Vs Q^2 . . . 20
1.11 The Gluon Helicity Distribution . . . 21

2.1 The Relativistic Heavy Ion Collider . . . 24
2.2 The Hydrogen Jet Polarimeter . . . 26
2.3 The STAR Detector . . . 28
2.4 The Time Projection Chamber . . . 30
2.5 The TPC Sector . . . 31
2.6 The TPC Multi-Wire Proportional Chamber . . . 32
2.7 Space Charge Potential and Distortions . . . 34
2.8 Grid Leak Residuals . . . 35
2.9 The TOF and VPD schematic . . . 37
2.10 A BEMC Tower . . . 39
2.11 The Endcap Calorimeter . . . 40
2.12 ZDC Module . . . 41
2.13 Front View of the BBC . . . 43

3.1 Infrared sensitivity . . . 50
3.2 Collinear sensitivity . . . 51
3.3 Collinear sensitivity . . . 52
3.4 Applied anti-kT Algorithm . . . 56
3.5 Algorithm Comparison: Number of jets . . . 57
3.6 Algorithm Comparison: Jet p_T . . . 58
3.7 Algorithm Comparison: Number of tracks . . . 58
3.8 Algorithm Comparison: Number of towers . . . 59
3.9 Algorithm Comparison: Track p_T . . . 59
3.10 Algorithm Comparison: Tower Energy . . . 60
3.11 Algorithm Comparison: Jet neutral energy . . . 61
3.12 Algorithm Comparison: Jet η . . . 62
3.13 Algorithm Comparison: Track η . . . 62
3.14 Algorithm Comparison: Tower η . . . 63
3.15 Algorithm Comparison: Jet ϕ . . . 63

3.16 Algorithm Comparison: Track ϕ . . . 64
3.17 Algorithm Comparison: Tower ϕ . . . 64
3.18 Particle and Parton Level Jet Matching . . . 66
3.19 ΔR vs. jet p_T . . . 67
3.20 Fractional Jets . . . 67
3.21 Fractional jet Vs. ΔR . . . 68

4.1 Average track p_T vs Run Index . . . 70
4.2 Gaussian $< p_T >$ . . . 71
4.3 Average track p_T vs Run Index . . . 71
4.4 Average Jet p_T vs Run Index . . . 74
4.5 Average Track p_T within Jet vs Run Index . . . 75
4.6 Average Tower Energy within Jet vs Run Index . . . 76
4.7 Detector η Vs Jet y . . . 80
4.8 Jet Resolution Vs Jet p_T . . . 90
4.9 Jet Resolution . . . 91
4.10 Vertex Z position . . . 93
4.11 Vertex Z position . . . 93
4.12 Re-Scaled Vertex Z Position . . . 94
4.13 Jet p_T . . . 95
4.14 Jet y . . . 96
4.15 Jet ϕ . . . 97
4.16 Invariant Mass . . . 98
4.17 $cos(\theta^*)$ . . . 99
4.18 Same-side jet neutral energy ratio . . . 100
4.19 Away-side jet neutral energy ratio . . . 101

5.1 Matching Jets . . . 105
5.2 Efficiency of "fake" jets . . . 105
5.3 Detector vs Particle Level Invariant Mass Spectra . . . 107
5.4 Unfolding Method Comparison . . . 115
5.5 The Dijet Cross Section . . . 118
5.6 Systematics . . . 121
5.7 Cross section ratio . . . 123

LIST OF TABLES

2.1 Trigger Conditions 44

3.1 Mid-Point Cone Parameters 53
3.2 Anti-k_T user parameters 55

4.1 Track and Tower Selection in Jet Reconstruction at the detector-level . . 73
4.2 Definition of jet_3 and jet_4 based upon the rapidity, y, of the two leading p_T jets. 78
4.3 Phase space of the dijet measurement 82
4.4 Results of a Simulation Only Filter Bias Test with an asymmetric pT cut at the pythia level of 7 and 10 GeV. These values are below our nominal asymmetric pT cut need for 500 GeV. 86
4.5 Results of an Embedded Filter Bias Test with an asymmetric pT cut of 10 and 13 GeV 86
4.6 Embedded Simulation Timing Test for Each pT bin with 11,701 events thrown and passing the dijet filter 87
4.7 Timing Table Continued 87
4.8 Second Draft of a Final Embedded and Filtered Simulation Request . . . 88
4.9 Final Embedded and Filtered Simulation Request 89
4.10 The raw dijet yields and the associated error, σ_Y, for each invariant mass bin for the JP2 trigger. 90
4.11 The estimated theoretical cross-section and the number events of thrown for the each partonic p_T bin 92
4.12 Table of fit parameters for the vertex z distribution 94

5.1 Different unfolding algorithms use different terminology when discussing the types of distributions. This table relates the terminology by row (true distribution = particle level dijets = cause). 103
5.2 The corrected yields, phase space and cross section values as a function of the dijet invariant mass. $\Delta|y_{max}| = 0.8$, PS = phase space = $\Delta M_{ij}\Delta|y_{max}|$, σ represents the double differential cross section and $\delta\sigma$ are the associated errors. 116
5.3 The calculated theoretical dijet cross section values using a renormalization scale of μ, 2μ, and 0.5μ without UE+HAD added on. The last column is the underlying event and hadronization corrections to the theoretical calculations. 117
5.4 The absolute systematic difference for each systematic error. The luminosity is not included in the overall total systematic. The systematic error range is determined σ_{orig} + $\delta\sigma^{sys}_{pos}$ and σ_{orig} - $\delta\sigma^{sys}_{neg}$, where $\delta\sigma^{sys}_{pos(neg)}$ is the systematic error added in quadrature with positive (negative) variations 120

Chapter 1 Introduction

1.1 The Spin on Life

The Earth's spin gives us day and night; a ballerina's spin provides beautiful movement, and the spin of fundamental particles determines the structure of matter. Fundamental particles are the most basic building blocks of our universe, making spin an integral part of our world. The Earth's rotation and a spinning ballerina are fundamentally different from the inherent spin of small particles. A particle's spin should not be interpreted as an object rotating about an axis, but instead as an intrinsic property, like mass and charge. Spin defines two classes of fundamental particles, those with half-integer spin (fermions) and others with integer spin (bosons).

1.2 The Standard Model

1.2.1 Fundamental Fermions and Bosons

Fundamental point-like fermions are grouped into two categories called quarks and leptons. Each group consists of six particles arranged into pairs or generations. The up and down quarks belong to the first generation, the strange and charm quarks form the second generation and the bottom and top quarks make up the third generation. Similarly, for the lepton sector there are the electron and electron neutrino, the muon and muon neutrino, and the tau and tau neutrino. These 12 particles and their antimatter counterparts comprise the known fundamental fermions in the universe.

Quarks are the building blocks of hadrons. Hadrons are separated into two groups: mesons and baryons, which are composed of two and three quarks respectively. For example the proton, a baryon, consists of two up quarks and a down quark. Hadrons containing higher generation quarks do decay into hadrons of the first generation.

Therefore, all stable detectable matter is made from first generation particles. The first generation leptons consist of the most stable and lightest particles. The other two heavier generations will quickly decay into the next most stable particle until they become part of the first generation. An exception to this rule are neutrinos, which do not decay but instead oscillate between flavor eigenstates.

Five fundamental bosons have been experimentally observed. The photon and gluon are massless, while the W, Z, and Higgs bosons have rest masses of 80.39 GeV, 91.19 GeV, 125.9 GeV [1] . The Standard Model is comprised of these 17 particles and their antiparticles as shown in Fig 1.1.

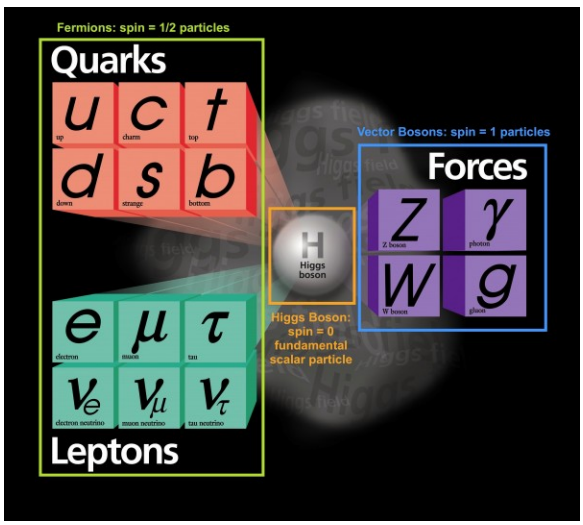

Figure 1.1: **The Standard Model** - The fundamental building blocks, as described by the standard model, of the universe including the newly discovered Higgs boson.

1.2.2 Fundamental Forces

There currently are four known fundamental forces in nature: the strong, weak, electromagnetic, and gravitational force. In the Standard Model forces are formulated in terms of a relativistic quantum field theory (QFT), which merges quantum mechanics and special relativity into one overarching theory. In this framework forces are generated by an underlying physical field and particles emerge as excited states of this field.

As a result the Standard Model the fundamental bosons function as force carriers. The strong, weak and electromagnetic forces are mediated by the exchange of gluons, W and Z bosons, and the photons, respectively. Hypothetically, the gravitational force could be mediated by the graviton, but it has yet to be detected. Furthermore, reconciling general relativity and relativistic quantum mechanics remains problematic, preventing gravity from being included in the Standard Model.

Particles experience different forces according to the associated charges they carry. The neutrinos, which are electrically neutral, interact only through the weak force. While the electron, muon, and tau leptons (anti-leptons) all have an electrical charge and can therefore interact via the weak and electromagnetic forces. Quarks have a fractional electric charge and couple to the electromagnetic and weak forces as well. In addition, quarks and gluons interact via the strong force, because they carry "color" charge. Color charge and its roe in strong interactions will be further discussed in section 1.3).

The strength of each force is characterized by a coupling constant, which is related to the charge of the interacting particle. For example, the dimensionless coupling constant for the electromagnetic force on an electron is

$$\alpha = \frac{e^2}{4\pi\epsilon_0\hbar c} \tag{1.1}$$

where e is the electric charge of an electron, ϵ_0 is the permittivity in free space, $\hbar$ is the Planck constant, and c is the speed of light. This is also known as the fine structure constant in electromagnetic interactions. However, the strength of each force, or the value of the coupling constant, varies with the distance between the particles experiencing the force. This distance is inversely proportional to the energy of the exchanged boson. At large distances, on the order of a fermi, the coupling constants for the strong, electromagnetic, weak, and gravitation forces are $\alpha_S \sim 1$, $\alpha \sim 1/137$, $\alpha_W = 10^{-7}$ and $\alpha_G \sim 10^{-40}$, respectively. The values of the coupling constants, however, do not truly remain constant. They change depending upon the

range of the force or the energy of the exchanged particle. This is referred to as the running of the coupling constants and has profound effects in physics, especially in the nature of the strong force.

1.3 Quantum Chromodynamics

Two particles carrying the same electric charge exert a repulsive force on each other. Why then do protons remain confined to atomic nucleus and not disperse due to their like sign charges? The reason: the strong force dominates at the nuclear scale.

Quantum Chromodynamics (QCD) is the theory that describes strong interactions and color is the conserved charge of the strong force. This color in no way refers to the hues seen by our eyes, but represents the degrees of freedom inherent in the strong force. A quark can be either "red", "blue", "green", "anti-red","anti-blue", or "anti-green". Gluons are bi-colored, carrying both a color and anti-color charge, allowing them to interact with themselves as well as quarks. This feature anti-screens the effective color charge of the quark. As one probes closer to the bare quark less color charge is seen because the color is being spread out by the colored gluon field.

This property of gluons results in the strong coupling constant α_S to exponentially rise at large distances or low energies. For very small separations, two quarks interact through a color field of reduced strength and asymptotically approach a state where they behave as essentially free, noninteracting particles. The progression of the strong coupling constant from low to high energies (large to smaller distances) is shown in Fig 1.2. The value of α_S approaches $\sim$0.118 at large energy $Q \sim 90$ GeV.

This behavior of the strong coupling constant results in asymptotic freedom at large energy scales, a property that facilitates the use of perturbation theory. Pertubative QCD expands the interaction terms in orders of α_S. At leading order (LO) only interactions sensitive to α_S are considered. At next to leading order (NLO) interactions with α_S and α_S^2 terms are considered and so on.

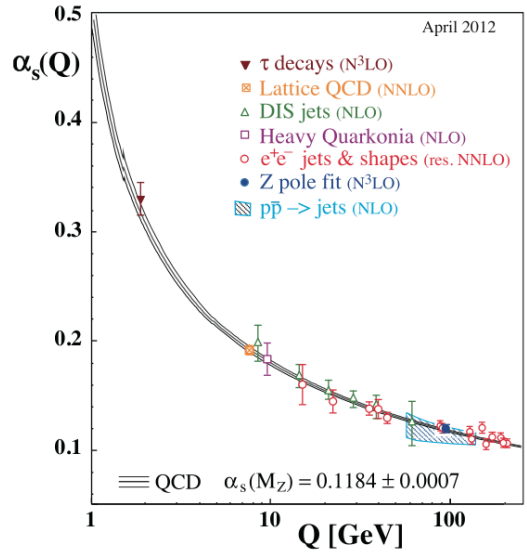

Figure 1.2: **Strong Coupling Constant at high** Q - Summary of measurements of α_S as a function of the energy scale Q. The respective degree of QCD perturbation theory used in the extraction of α_s is indicated in brackets [2]

Traditionally experimentalists have accessed quark and gluon properties through lepton-lepton, lepton-proton, proton-proton, and proton-antiproton scattering experiments. The first proton structure experiments [3] used lepton-proton scattering as diagramed in Fig 1.3. In this picture the incoming electron has a four-momentum p_1 and interacts with a proton carrying a four-momentum of p_2. The interaction is mediated by a virtual photon with a four momentum of q. The scattered electron carries four momentum p_3 and the proton final state has a four momentum of p_4. If the electron elastically scatters then the proton final state is just a proton. However, if q is large enough to destroy the original proton, and the photon interacts with only one quark, then the process is known as *Deep Inelastic Scattering* (DIS).

Experimentally, the conditions for deep inelastic scattering are met when the invariant mass of the proton final state, W, is outside of the resonance region (> 2 GeV) and the four momentum squared, Q^2, is large (> 1 GeV) . The four momentum

squared and the invariant mass are expressed by the following equations:

$$Q^2 = -q^2 = -(p_1 - p_3)^2 = 4E_1E_3\sin\left(\frac{\theta}{2}\right) \tag{1.2}$$

and

$$W^2 = p_4^2 = (p_2 + q)^2 = M^2 + 2M\nu - Q^2 \tag{1.3}$$

where $\nu = E_1 - E_3$, θ is the scattering angle, and M is the mass of proton. Not only does DIS describe the photon-quark hard scattering interactions in lepton-proton collisions, it is also applicable to parton-parton hard scattering interactions in proton-proton collisions. In both type of collisions the Q^2 characterizes the energy and distance scale of the interaction.

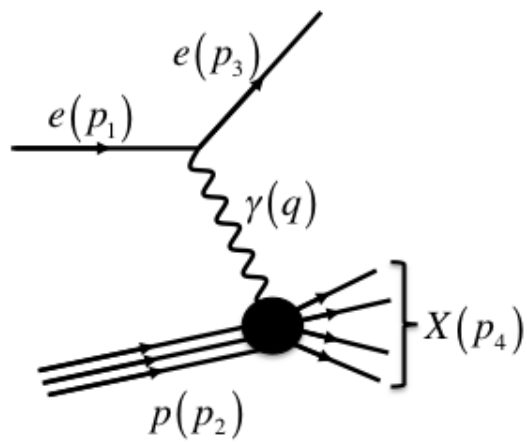

Figure 1.3: **Deep Inelastic Scattering** - A diagram of a lepton beam colliding into a proton target causing the proton to break apart.

1.3.1 Fragmentation and Hadronization

In DIS experiments quarks and gluons (collectively referred to as partons) experience large accelerations due to the momentum transfer from a virtual particle. These

accelerated partons will quickly begin to radiate soft gluons, which in turn may branch into pairs of gluons or quarks. If the scattering is caused by a color field, then the nature of the strong force will cause the energy of the field to increase as the parton is accelerated away from the interaction. At some point it is energetically favorable for the field to create q-qbar pairs, which continue to move outward, causing the field to spawn additional pairs [4].

Both of these mechanisms contribute to a process called fragmentation and result in a shower of partons emanating from the struck parton and it's interactions with the field. At some point the partons in the shower *hadronize* and form colorless baryons and mesons. This phenomena is referred to as color confinement and prevents experimentalists from directly detecting a free quarks and gluons. The mechanisms driving hadronization are not well understood and because the showers are formed from increasingly lower energy partons perturbative QCD calculations cannot be applied in this regime.

1.3.2 Jets

The nature of the strong forces prevents experimentalists from directly detecting colored quarks and gluons. Therefore jets are used as proxies for the scattered partons that participated in the hard interaction. Experimentally, a jet is the collective energy deposition in a detector from the stable final state particles that are produced in the hadronization process [5]. Jets may also be defined as the collection of the outgoing hadrons prior to detector interactions or the collection of outgoing partons after fragmentation. Thus, jets are defined at three-levels, the detector, the particle, and the parton level.

Jets are not universal observables, meaning they can be defined in multiple ways using different algorithms. Jet algorithms cluster partons, or particles based on proximity in coordinate space (for example cone algorithms) or proximity in momentum

space (for example k_T algorithms). The details of these algorithms will be discussed in the following chapters.

Jet observables have served as excellent tests of perturbative quantum chromodynamics (pQCD) predictions, as well as tools to probe new physics. For example the observation of 3-jet events, in electron-positron annihilation experiments, provided the first direct evidence for the existence of gluons. It indicated that hard gluon bremsstrahlung is the dominate source of hadrons transverse to the main jet axis [6].

A dijet event is defined by the observation of two nearly back to back jets. In events where there are two and only two jets, it is possible to use the direction and transverse momentum of the jets to determine the kinematics of the initial partons. This is especially important in proton-proton collisions where the initial parton momentum cannot be determined from the proton momentum. In contrast, the initial parton momentum can be reconstructed in lepton scattering experiments from the initial and final momentum and energy of the lepton beam. The main measurement addressed in this thesis is the probability for two partons to collide and form a dijet event.

1.3.3 Underlying Event

In proton-proton collisions the "underlying event" is everything except the outgoing jets produced from the hard scattered partons. The proton remnants, the partons not associated directly with the hard scattering, must also partake in the hadronization process leading to final state particles that are not related to the process of interest. These spectator particles may be swept up in the jet algorithm and therefore artificially contribute to the jet energy scale. It is an unavoidable background in collider observables. [7].

In events that involve proton collisions, especially with high energies, hard interactions between multiple partons may occur. Multiple parton interactions (MPIs) are when at least two hard scatterings occur in a single proton-proton collision and

the addition interactions become a component of the underlying event. In addition, initial and final-state radiation (IFR) occurs, which is when the partons emit soft radiation prior and/or after the hard collision. The initial-state radiation, but not the final-state radiation, can add to the underlying event background observed. Unlike the other background contributors the IR can be theoretically calculated. All the contributions to the underlying event are illustrated in Fig 1.4.

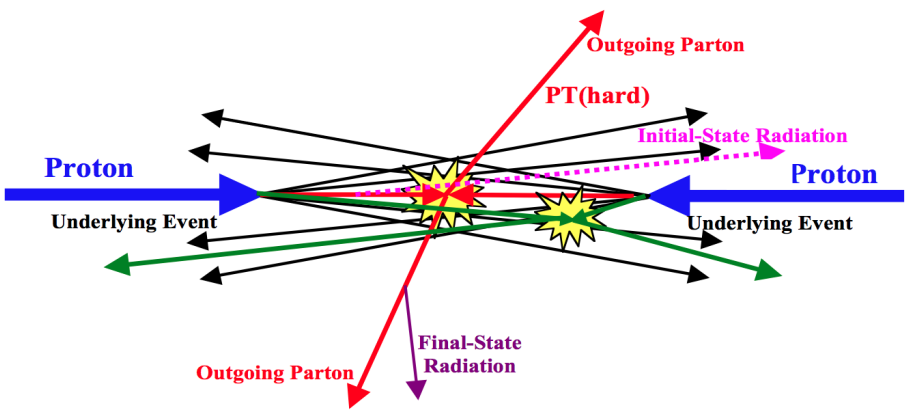

Figure 1.4: **The Underlying Event** - An illustration of the hard scattering partons (red) and the inevitable underlying event (black). The initial (pink) and final (purple)-state radiation and mutliple parton interactions (green) are also shown, which are often considered as part of the underlying event. [7]

1.4 Parton Distribution Functions

The proton is made of three valence quarks (two up quarks and one down quark) and numerous sea quarks which are held together through the exchange of gluons. The parton distribution functions (PDFs) represent the probability of finding a parton carrying a momentum fraction x of the proton at a certain energy scale Q^2. The parton distribution functions cannot be determined solely through pQCD calculations. Instead, they are extracted by confronting experimental data with theorectical curves that incorporate partonic cross section calculations and account for the Q^2 evolution of the PDFs [8]. For example, in electron-proton scattering, the inclusive cross section

is described by the following equation:

$$\sigma_{ep} = \sum_i \int e_i^2 f_i(x, Q^2) \hat{\sigma}_i(x, \alpha_s, Q^2) dx. \tag{1.4}$$

This equation relates the theoretically calculated partonic cross-section, $\hat{\sigma}_i(x, \alpha_s, Q^2)$, to the observed cross-section, σ_{ep} via the various quark PDFs $f_i(x, Q^2)$. The quark momentum distribution functions are often denoted by their flavor $f_i(x, Q^2) = u(x, Q^2)$, $d(xQ^2)$, $s(x, Q^2)$, etc. The mystery of the proton structure can only be unraveled through the use of both experimental data and theoretical calculations.

Numerous scattering experiments (pp, $p\bar{p}$, lp) are included in the global analyses used to determine the PDFs [9] [10] [11]. To date the tightest constraints on the PDFs come from e-p collisions at the HERA collider [12]. The inclusive differential cross-section for inelastic electron-proton scattering is

$$\frac{d\sigma}{dE' d\Omega} = \frac{\alpha^2}{4E^2 \sin^4 \frac{\theta}{2}} \left(W_2(\nu, q^2) \cos^2 \frac{\theta}{2} + 2W_1(\nu, q^2) \sin^2 \frac{\theta}{2} \right) \tag{1.5}$$

where W_1 and W_2 are the structure functions of the proton. As discussed in detail by several particle physics books [13], $MW_1(\nu, Q^2)$ and $\nu W_2(\nu, Q^2)$ can be reformulated in terms of $F_1(x)$ and $F_2(x)$ if Q^2 and ν are large enough to resolve point-like partons inside the proton. In this kinematic limit, known as the scaling regime, F_1 and F_2 are only dependent on the dimensionless Bjorken scaling variable $x_B = x = \frac{Q^2}{2M\nu}$, which is the fraction of proton momentum carried by the parton.

Therefore, in the scaling regime, deep inelastic electron-proton scattering should be viewed as elastic scattering of the electron on a free quark within the proton. This in turn connects F_1 and F_2 to the PDFs in the simple parton model

$$F_2(x) = 2xF_1(x) = \frac{1}{2} \sum_i e_i^2 f_i(x) \tag{1.6}$$

where the sum is over both quark and antiquark flavors. The identity, $F_2(x) = 2xF_1(x)$, is known as a Callan-Gross relation and is a direct consequence of the spin

$\frac{1}{2}$ nature of quarks.

The experimental measurements of the differential cross-sections allows for the extraction of the proton structure function $F_2(x)$. If the quarks are truly point-like then F_2 should be independent of Q^2 and the world data shown in Fig 1.5 confirms this behavior in a limited x range ($0.05 > x > 0.4$). However, at low and high x the structure function F_2 clearly exhibits scaling violations, or a Q^2 dependence. In this regime the simple parton model begins to break down because it does not include the effects of gluons and gluon radiation in hard scattering processes. Low x sea quarks are produced as quark-antiquark pairs from the exchanged and radiated gluons. Only large Q^2 photons are able to resolve the low x quarks, causing F_1^p to rise with increasing Q^2 at low x. The slope of the scaling violation is reversed at high x, because sensitivity to gluon emission is reduced at low Q^2.

Fig 1.6 shows the momentum PDFs as a function x and Q^2 as extracted from a next-to-next-to leading order (NNLO) global analysis [15]. The red and blue curves represent the up and down quark parton distribution functions and peak at large x ($x > 0.1$), which is excepted since valence quarks carry a relatively large fraction of the protons momentum. The green and yellow curves are the momentum distribution functions for the gluons and sea quarks respectively. The distributions for gluons and sea quarks, which have been scaled down by a factor of 0.10, tend rise exponentially in the low x regime especially as the Q^2 increases. This plot indicates that the gluons and sea quarks tend to carry the majority of the proton's momentum in the low x regime, which also agrees with the fact that scaling violations tend to have a large effect at low x. Integrating the PDFs over the entire x range will determine the total momentum carried by each parton flavor. For example the following equation

$$\epsilon_u = \int_0^1 dx x(u + \bar{u}) \tag{1.7}$$

expresses the total momentum carried by the u quarks and antiquarks in the proton. Deep inelastic scattering experiments have shown that the electrically neutral gluons

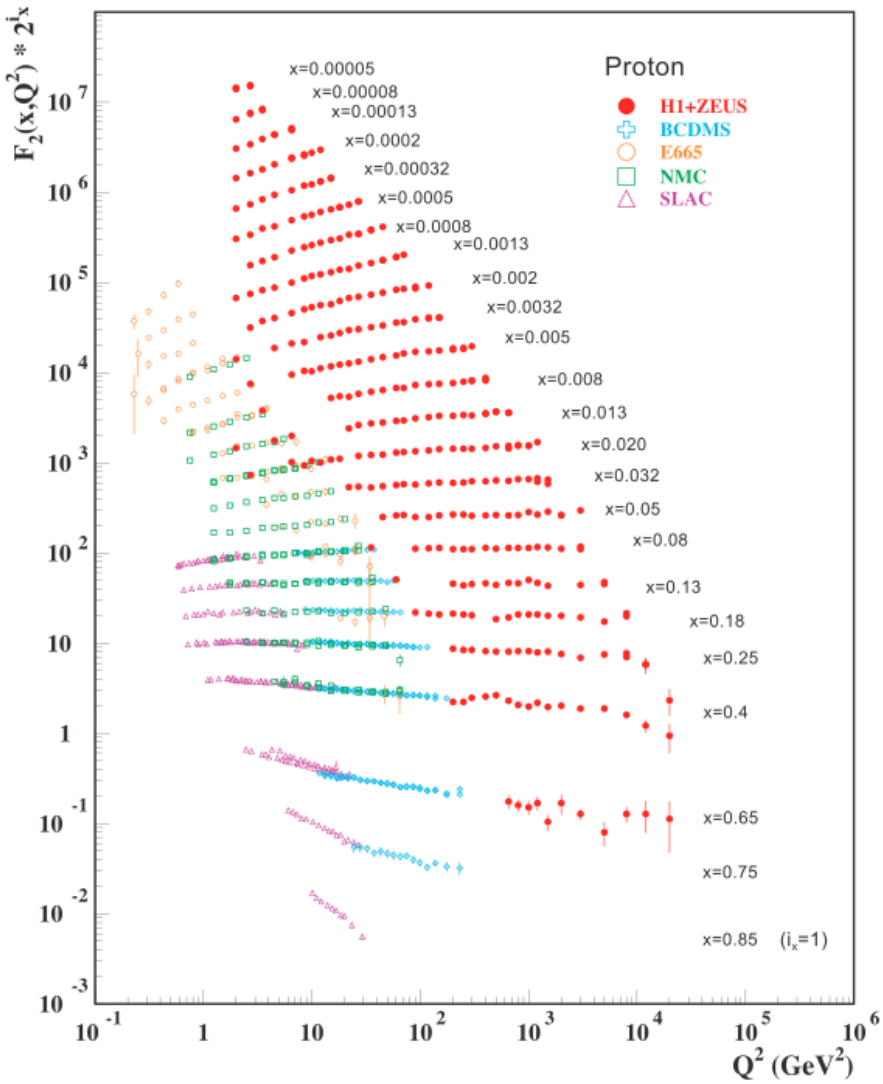

Figure 1.5: F_2^P **VS** Q^2 - A representative selection of data on the proton electromagnetic structure function F_2^p from collider (HERA) and fixed target experiments that clearly shows the pattern of scaling violation [14]

carry about 50% of the proton momentum [16].

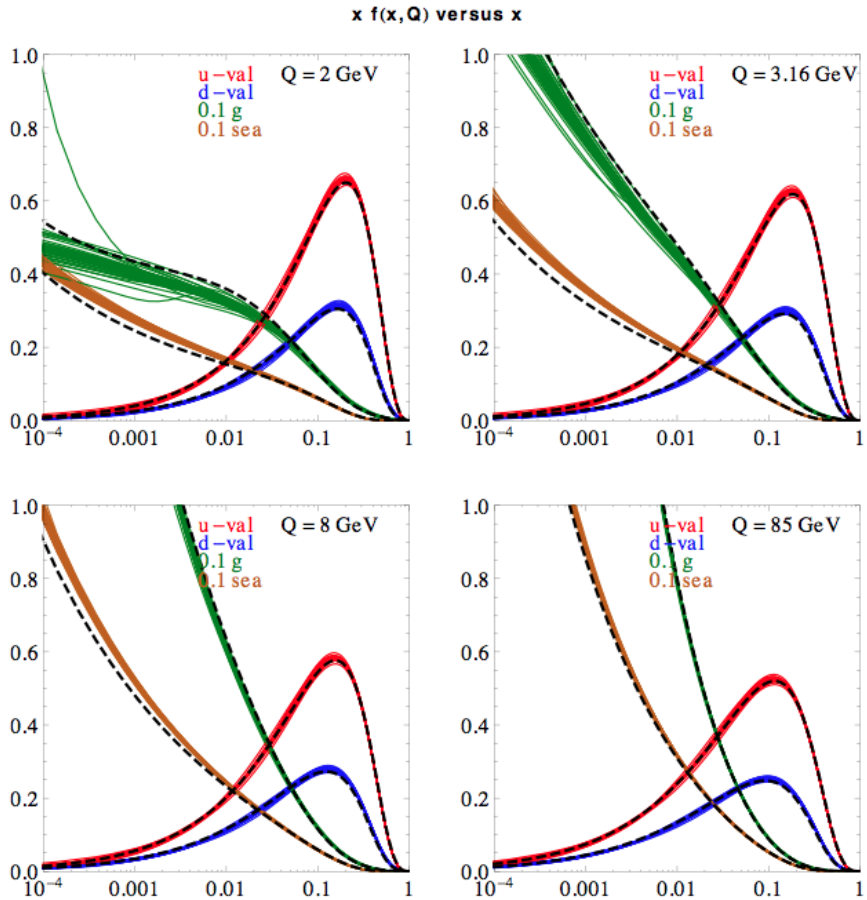

Figure 1.6: **CT10NNL0 parton distribution functions** - These figure show the PDFs from the CTNNL0 analysis. Each group shows $xu_{valence} = x(u - \bar{u})$, $xd_{valence} = x(d - \bar{d})$, $0.10xg$ and $0.10xq_{sea}$ as a function of x for a fixed value of Q. The values of Q are 2, 3.16, 8, and 85 GeV. The quark sea contribution is $q_{sea} = 2(\bar{d} + \bar{u} + \bar{s})$.The dashed curves are the central CT10 NLO fit. [15]

1.5 Polarized Parton Distribution Functions

Angular momentum, like energy and charge, must be conserved in all interactions. This means the spin and orbital motion of the quarks and gluons must sum at all times to the value of the proton spin. The helicity PDFs, $\Delta f(x, Q^2)$, represent the probability of finding a parton whose spin is aligned minus the probability of finding

a parton whose spin is anti-aligned with the spin of a longitudinally polarized proton at a specific momentum fraction x and Q^2.

$$\Delta f_i(x, Q^2) = f_i^+(x, Q^2) - f_i^-(x, Q^2) \tag{1.8}$$

where $f^+(x, Q^2)$ $[f^-(x, Q^2)]$ is the parton distribution with positive [negative] helicity.

The advent of polarized lepton beams and proton targets allowed physicists to examine the spin structure within the proton using *polarized deep inelastic scattering* (pDIS). The polarization of the lepton beam and proton can either be parallel or antiparallel to one another. If the quark spins are preferentially (anti-) aligned with the spin of the parent proton, then the interaction of the virtual photon with the quark will depend on the spin of the proton. Conservation of angular momentum only permits the spin 1 photon to be absorbed by a spin 1/2 quark with a helicity opposite to that of the photon. Therefore, a nonzero asymmetry in the scattering rate of virtual photons off protons with parallel and antiparallel helicity states would indicate that the quark spins are correlated with the parent nucleon spin. The difference in the observed differential cross-section upon reversal of the nucleon spin provides direct access to measure the polarized proton structure functions $g_{1,2}$

$$A_{LL} = \frac{d^2\sigma^{\rightrightarrows}}{d\Omega dE'} - \frac{d^2\sigma^{\rightleftarrows}}{d\Omega dE'} = \frac{4\alpha^2 E'}{Q^2 E M \nu}\left[(E + E'\cos\theta)g_1(x, Q^2) - 2xMg_2(x, Q^2)\right] \tag{1.9}$$

where $\rightarrow$ and $\Rightarrow$ indicates the spin directions of the lepton beam and nucleon. Analogous to $F_{1,2}$, which represents the unknown momentum structure of the quarks in the proton, the spin dependent structure functions $g_{1,2}$ encapsulates our ignorance about the partonic spin structure of the proton. Measurements of the longitudinal double spin asymmetry, A_{LL}, allow for the extraction of $g_1(x, Q^2)$. The relationship between this structure function and the quark spin distributions in the simple parton

model is described as follows

$$g_1(x) = \frac{1}{2}\sum_i e_i^2 \Delta f_i(x). \tag{1.10}$$

where $\Delta f_i(x)$ is the quark helicity PDF and e_i is the charge of the quark. Similar to the unpolarized case, the simple parton model does not incorporate gluons and therefore does not exhibit any Q^2 dependence. However, as in the unpolarized case, Fig 1.7 demonstrates the scaling violations of $g_1^P(x, Q^2)$[17]. The QCD scale evolution of $g_1(x, Q^2)$ provides insight to the gluon helicity function $\Delta g(x)$.

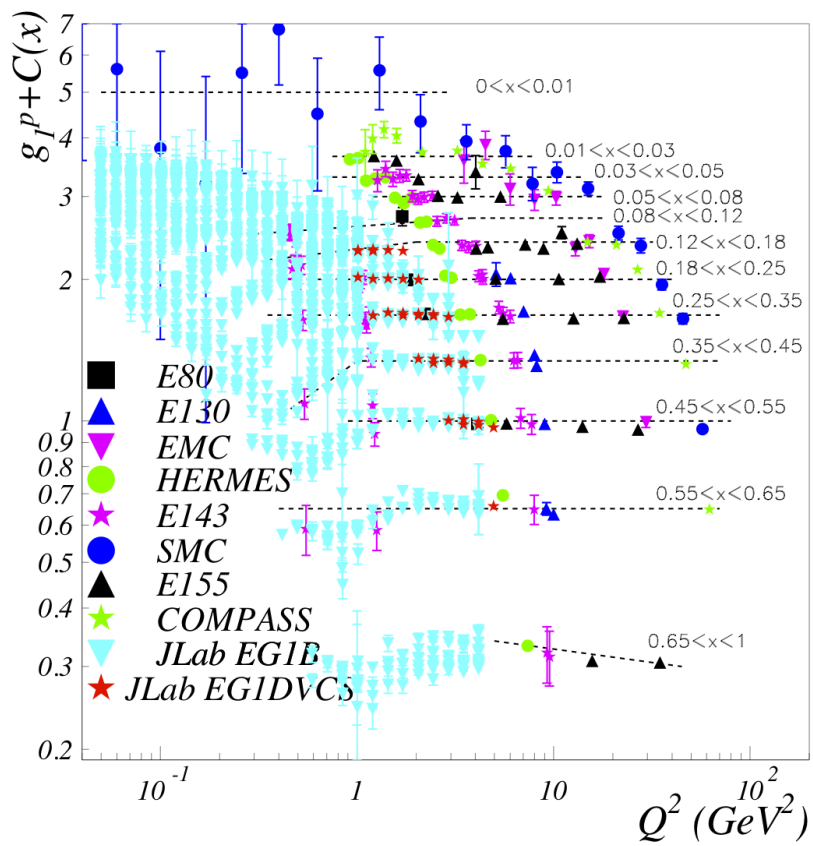

Figure 1.7: g_1^P **VS** Q^2 - The spin dependent structure function of the proton as a function of Q^2 extracted by measurements from multiple experiments. The momentum fraction x of the proton sensitivity is indicated in the plot. [17]

The polarized parton distribution functions as a function of x are shown in Fig

1.8 for all partons within the proton. The large amount of lepton-nucleon pDIS data has tightly constrained the valence quark contributions to the proton spin (top two plots). The spin of the (down) up quarks tend to (anti-)align themselves with spin direction of the proton. However, the sea quark and gluon distributions remain highly unconstrained. This is due to the limited kinematic reach in x and Q^2 of the lepton-nucleon fixed target pDIS experiments. This is highlighted by the comparisons of Fig 1.5 and Fig 1.7.

The total contribution from the quarks to the proton spin is given by integrating the quark helicity PDFs over all x:

$$S_z^q(Q^2) = \int_0^1 \sum_i \Delta f_i(x, Q^2)dx + \Delta \bar{f}_i(x, Q^2)dx \tag{1.11}$$

The European Muon Collaboration at CERN was the first to measure $S_z^q = (14 \pm 9 \pm 21)\%$ in 1988[19]. Since then the DIS data shown in Fig 1.7 have been incorporated into several global analyses [18] [20] [21]. The DSSV extraction gives $S_z^q(Q^2) = 24.2\%$ at a $Q^2 = 10$ GeV^2. This value does not vary strongly with Q^2 or with different theoretical extractions.

1.5.1 Gluon Spin

The lepton-nucleon pDIS experiments demonstrated that the overall proton spin has a relatively small contribution from the quark spin. This naturally raises the question: where is the rest of the proton spin? In the infinite momentum frame the half integer spin of the proton can be broken down into it's constituent parts:

$$J_z^N = S_z^q + L_z^q + \Delta G + L_z^g = \frac{1}{2} \tag{1.12}$$

where S_z^q, ΔG, L_z^q, and L_z^g are the contributions from the quark spin, the gluon spin, the orbital momenta of the quarks and the orbital momenta of the gluons, respectively. In this framework it is not clear how to experimentally access L_z^q and

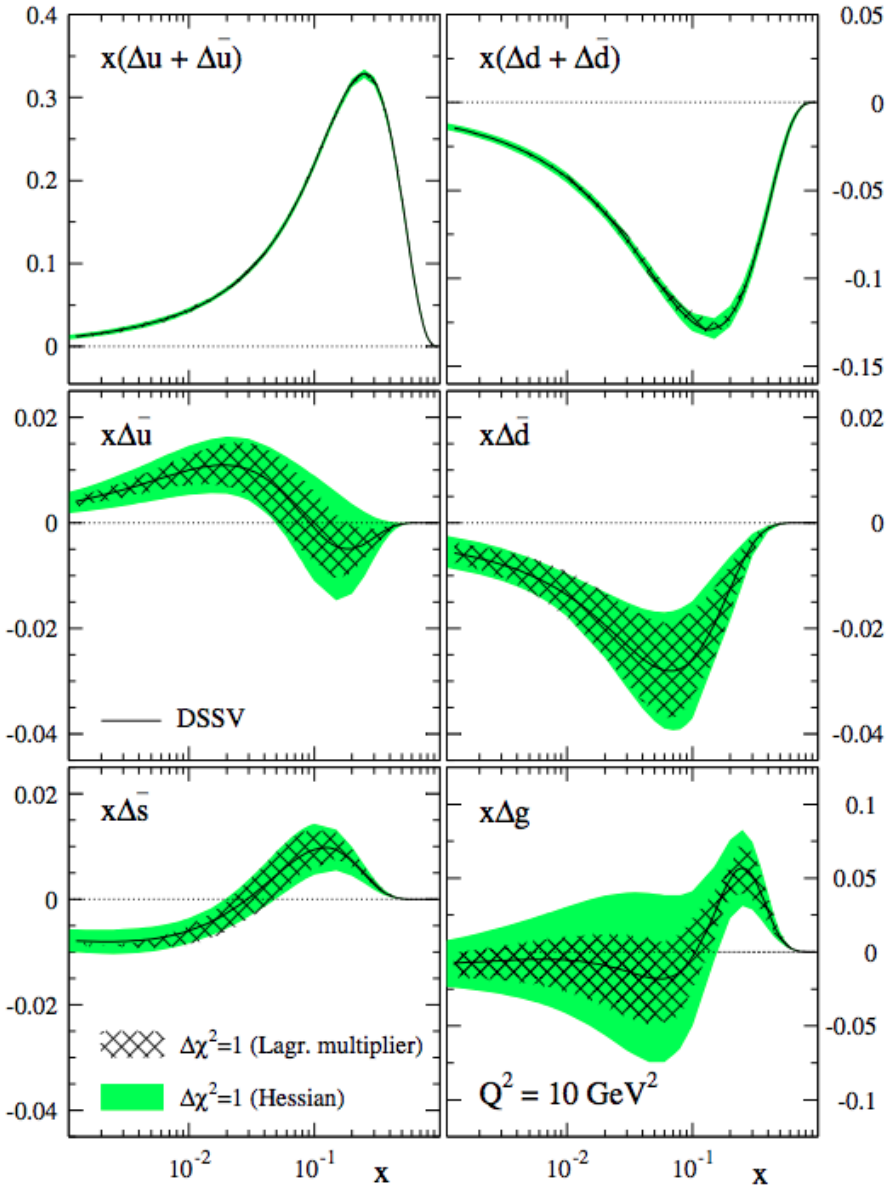

Figure 1.8: **Polarized Parton Distribution Functions** - The polarized parton distribution of the proton at $Q^2 = 10\ GeV^2$ along with their $\Delta\chi^2 = 1$ uncertainty bands computed with Lagrange multipliers [hashed band] and the improved Hessian approach [green band]. The method for determining the error band is described in Ref. [18]. The total up and down spin distributions are shown in the top two plots, which inclusive DIS probes primarily, are the most constrained. The sea quark spin distributions (the light sea and strange quark) are the following three plots, which is constrained by semi-inclusive DIS. The lower-right plot is the spin-dependent gluon distribution, which is remains highly unconstrained especially at low x.

L_z^g, leaving ΔG as the next candidate to be experimentally measured. A major disadvantage of the l-p pDIS experiments is the inability for leptons to directly couple with gluons. The virtual photon emitted from the interacting lepton can only interact with electromagnetically charged particles, namely the quarks within the proton. Therefore, at leading order the lepton is blind to the gluons within the proton. It is only through higher-order interactions that pDIS has any sensitivity to the gluon spin structure. Unfortunately, the limited kinematic range of pDIS data leaves ΔG highly unconstrained.

One of the main objectives of the RHIC-Spin program is to directly measure the gluon helicity distribution using polarized proton-proton collisions. This type of collision, mediated by the strong colored interaction, provides leading order access to the gluon. As an illustrated example, in Fig 1.9, a parton from each polarized proton (one quark and one gluon) is involved in the hard interaction. The virtual parton mediator then splits into a quark and gluon, which will then hadronize and produce a spray of particles that form jets. This type of interaction provides leading order sensitivity to the gluon spin.

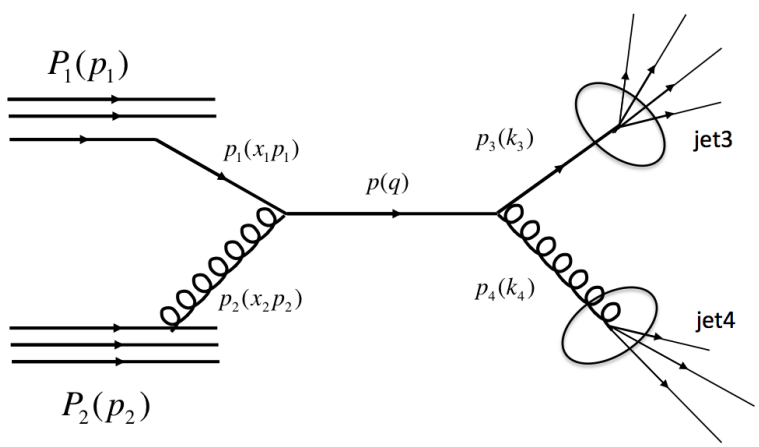

Figure 1.9: **P-P scattering** - A diagram of a proton-proton collision highlighting a leading order gluon interaction.

The gluon contribution to the spin of the proton is the first moment of the gluon

helicity distribution functions $\Delta g(x)$:

$$\Delta G = \int_0^1 \Delta g(x) dx \tag{1.13}$$

Experimentally, STAR can measure ΔG by constraining the possible values of $\Delta g(x)$ in the range of $0.02 < x < 0.2$.

1.5.2 Accessing the Gluon Spin

As in the lepton-proton pDIS measurements, the longitudinal double spin asymmetry, A_{LL} will be used to access the spin structure of the proton in proton-proton collisions. This quantity is the ratio of the difference and the sum of the jet cross section with parallel and anti-parallel initial polarization states:

$$A_{LL} = \frac{\Delta\sigma}{\sigma} = \frac{(\sigma^{++} + \sigma^{--}) - (\sigma^{+-} + \sigma^{-+})}{(\sigma^{++} + \sigma^{--}) + (\sigma^{+-} + \sigma^{-+})}. \tag{1.14}$$

In the framework of QCD the polarized and unpolarized jet cross sections can be expressed as

$$\Delta\sigma = \sum_{ij} \int \Delta f_i(x_1, Q^2) \Delta f_j(x_2, Q^2) \Delta\hat{\sigma}_{ij}(x_1, x_2, \alpha_s, Q^2) dx_1 dx_2 \tag{1.15}$$

$$\sigma = \sum_{ij} \int f_i(x_1, Q^2) f_j(x_2, Q^2) \hat{\sigma}_{ij}(x_1, x_2, \alpha_s, Q^2) dx_1 dx_2 \tag{1.16}$$

respectively. Therefore, we can express the double spin asymmetry as

$$A_{LL} = \frac{\sum_{ij} \int \Delta f_i(x_1, Q^2) \Delta f_j(x_2, Q^2) \Delta\hat{\sigma}_{ij}(x_1, x_2, \alpha_s, Q^2) dx_1 dx_2}{\sum_{ij} \int f_i(x_1, Q^2) f_j(x_2, Q^2) \hat{\sigma}_{ij}(x_1, x_2, \alpha_s, Q^2) dx_1 dx_2} \tag{1.17}$$

where the parton level cross-sections are calculable by pQCD, the unpolarized PDFs $f_i(x, Q^2)$ are well determined from unpolarized experiments, and the quark helicity PDFs are tightly constrained from previous pDIS experiments.

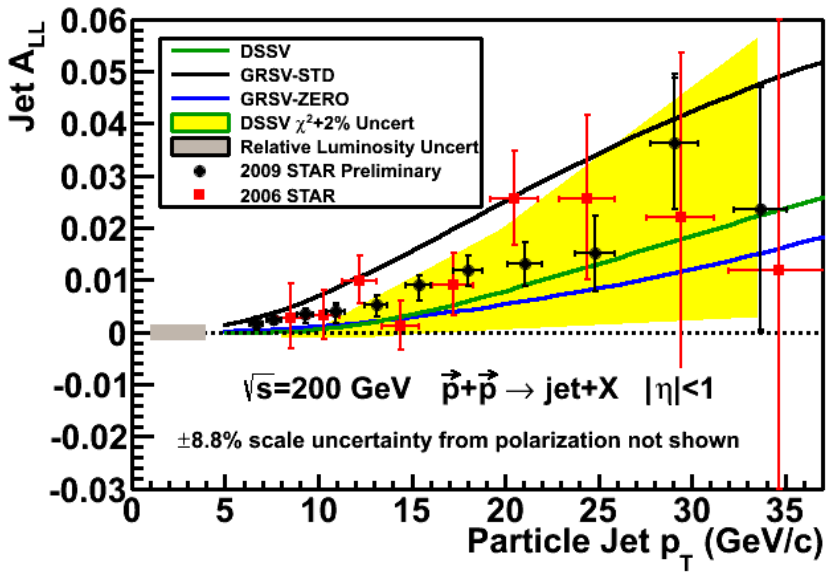

Figure 1.10: **Inclusive Jet A_{LL} Vs Q^2** - The STAR inclusive jet double spin asymmetry, A_{LL}, as a function of the particle jet transverse momentum. The 2006 and 2009 A_{LL} measurement is shown in red and black, respectively. Overlaying the experimental data are three theoretical predictions: DSSV (green), GRSV-std (black), and GRSV-zero (blue).

Proton-proton collisions are considered relatively complicated and "messy" when compared to lepton-proton interactions.The detection of a scattered lepton is relatively straightforward and allows for the calculation of the partonic kinematics, x and Q^2. In proton-proton collisions the scale of the interaction is the transverse momentum ($\hat{p_T}$) of the scattered partons in the center of mass frame. Due to the nature of the strong force the reconstructed jet p_T must serve as a proxy for the partonic $\hat{p_T}$. The connection between measured jet observables and theoretical predictions can only be made if detector and trigger effects that alter the reconstructed jet p_T and rapidity are understood and accounted for correctly. Therefore, prior to calculating a spin-dependent observable like A_{LL}, one that requires the full framework of pQCD in order to extract the helicity PDFs, it is necessary to confirm that the unpolarized cross-section agrees well with the pQCD predictions.

The STAR collaboration measured the inclusive jet and dijet cross-section at

a center of mass energy of 200 GeV and confirmed a strong agreement with pQCD calculations [22] [23]. With these measurements made and confirmed, the inclusive jet A_{LL} as a function of transverse jet momenta was calculated. This 200 GeV 2009 result is shown in Fig 1.10 and the data systematically lies above the DSSV best fit curve. This measurement provides the first indications of a non-zero $\Delta G = \int_{0.05}^{0.2} \Delta g(x) = 0.1 \pm^{0.06}_{0.07}$ [24].

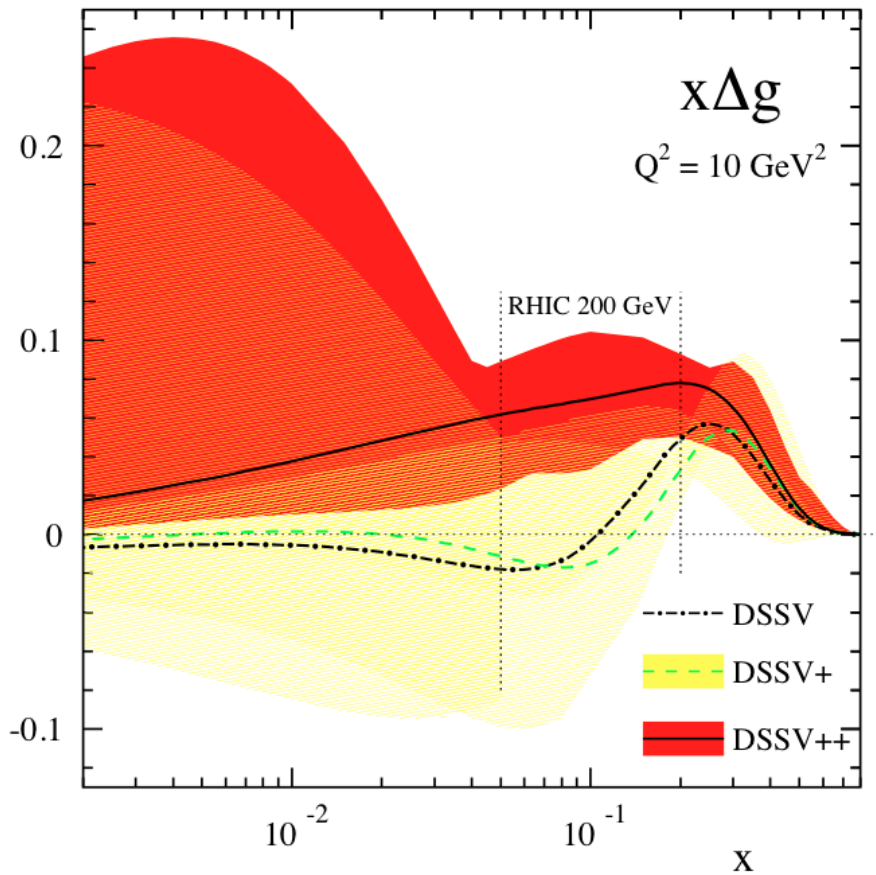

Figure 1.11: **The Gluon Helicity Distribution** - The gluon helicity distribution $\Delta g(x)$ of the proton as a function of momentum fraction of the proton x at a scale of 10 GeV^2. The red (yellow) band are uncertainties with (without) the RHIC 2009 data [24]

The focus of this thesis is the crucial step of calculating the dijet cross-section at a center of mass energy of 500 GeV from data collected in 2009 at the STAR detector. The increase of center of mass energy from 200 to 500 GeV will extend STAR's

kinematic range down to an $x \sim 0.02$. As shown in Fig 1.11 this extension is vital since the low x contribution to $\Delta g(x)$ is highly unconstrained. The dijet channel will also provide tighter constraints than the inclusive jet channel on the functional form of $\Delta g(x)$. The initial partonic x of the participating partons cannot be extracted on an event by event basis in the inclusive jet channel. Only a loose correlation between the jet kinematics and the range and mean of the x distribution can be made. However, at leading order the partonic x_1, x_2 and center of mass scattering angle $\cos(\theta^*)$ can be accessed from the dijet transverse momenta and rapidities according to the following equations:

$$x_1 = \frac{1}{\sqrt{s}} \left(p_{T3} e^{\eta_3} + p_{T4} e^{\eta_4} \right) \tag{1.18}$$

$$x_2 = \frac{1}{\sqrt{s}} \left(p_{T3} e^{-\eta_3} + p_{T4} e^{-\eta_4} \right) \tag{1.19}$$

$$\cos(\theta^*) = \tanh\left(\frac{\eta_3 + \eta_4}{2} \right) \tag{1.20}$$

This information will allow theorists to better constrain the shape of $\Delta g(x)$ and therefore significantly reduce the systematic errors associated with the determination of the first moment. The measurement of the dijet cross-section at $\sqrt{s} = 500$ GeV will provide the crucial first test of STAR's ability to reconstruct dijets, use these observables for future A_{LL} measurements and therefore take the next steps towards constraining the gluon helicity distribution at lower x.

Chapter 2 RHIC and The STAR Detector

2.1 The Relativistic Heavy Ion Collider

The Relativistic Heavy Ion Collider (RHIC) is located at the Brookhave National Laboratory in Upton, New York. RHIC is the world's first and only polarized proton-proton collider. The two 3,834 m long rings house five interaction regions. Two of these regions are equipped with spin rotators allowing for the possibility of either longitudinally or transversely polarized proton collisions at variable energies reaching up to $\sqrt{s} = 500$ GeV. This versatility make RHIC an excellent laboratory for proton spin structure experiments. In addition to polarized collisions, RHIC is capable of colliding various species of ions. This program is aimed at observing the dynamics and kinematics of the quark-gluon plasma (QGP). This high temperature, high density QCD phase, where quarks and gluons are de-confined from hadrons, gives insight into the properties of matter nearly following the Big Bang.

This section will describe the overall layout of the RHIC facility at BNL and the devices required to acquire and maintain beam polarization.

2.1.1 RHIC Layout

Two independent rings, arbitrarily denoted as the "Blue" and "Yellow" rings, accelerate heavy ions and/or protons clockwise and counter-clockwise, respectively. A diagram of the RHIC complex is shown on Fig 2.1. There are five interactions points (IPs), located at 12, 2, 6, 8, 10 o'clock positions on the RHIC ring. The STAR detector, at the 6 o'clock position, is the focus of this thesis and is described in Section 2.2. The polarimeters and the PHENIX experiment, are located at the 12 and 8 o'clock IPs.

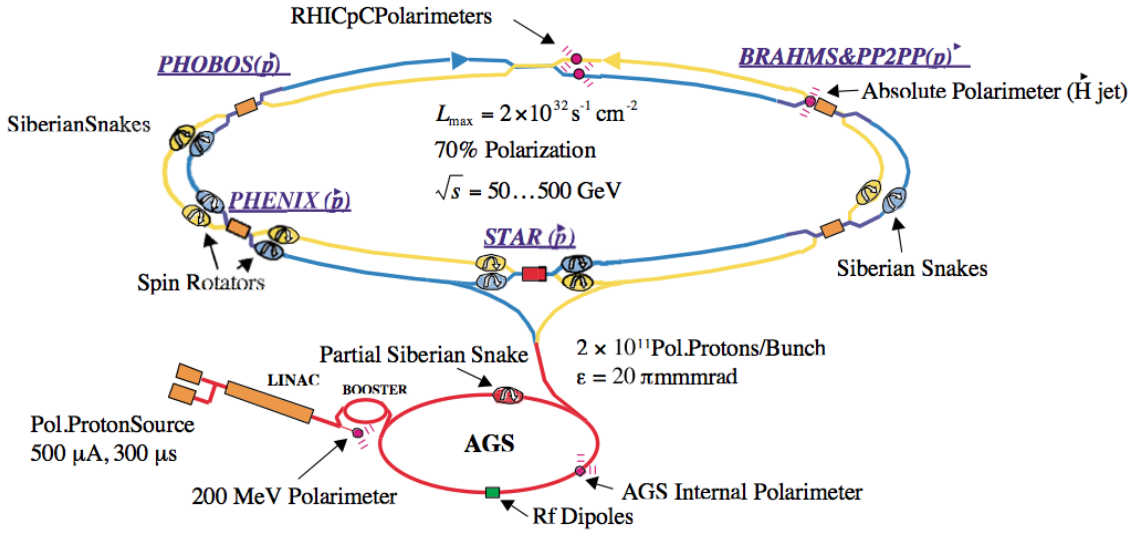

Figure 2.1: **The Relativistic Heavy Ion Collider** - The Brookhaven proton facility complex, highlighting the helicity-spin controlling and monitoring devices [25].

2.1.2 Polarized Proton Injection

The RHIC accelerator chain starts with an optically-pumped polarized H^- ion source (OPPIS), which was developed in collaboration among BNL, KEK, INR (Moscow), and TRIUMF [26]. Polarized hydrogen ions are produced in OPPIS at a 300 μs pulsed current of 0.5-1.0 mA, providing an intensity of $\sim 9 \times 10^{11}$ H^- ions in each pulse with 80-85% polarization. At an energy of 35 keV, the pulse of H^- ions leave the source to be accelerated to 200 MeV with a radio-frequency quadrupole and LINAC. This process results in $\sim$ 50% of the original OPPIS beam being accelerated to 200 MeV. The 300 μs pulse of H^-ions is then sent into the Booster as a single bunch of $\sim 4 \times 10^{11}$ polarized protons. The bunch is accelerated to 2.4 GeV in the Booster and transferred to the Alternating Gradient Synchrotron (AGS), where it is further accelerated to $\sim$ 25 GeV before injection into RHIC. Once in the RHIC rings, the beams are accelerated to and stored at the desired energies. This thesis will discuss energies of 250 GeV per beam.

2.1.3 Siberian Snakes

A vital aspect of high energy polarized proton-proton collisions is the maintenance of the beam polarization. As the proton beams are accelerated both the orbital and spin motion must be controled. There are two main types of depolarizing resonances: imperfection resonances, which are driven by magnet errors and misalignments, and intrinsic resonances, driven by the focusing fields [25]. Siberian Snakes are a system of magnetics, which generates a 180° spin rotation about a horizontal axis. The Siberian Snakes will provide a stable spin direction at all times as long as they rotate the of spin polarization of the protons at a faster rate than rotations due to other resonance driving fields. [27]

2.1.4 Measuring Beam Polarization

A critical aspect of extracting a spin-dependent observable is the monitoring of the beam polarization, which determines the percentage of the accelerating proton beams with spins pointing in the same direction. The spin of the proton beam is transverse to the direction of motion. The polarization of each beam is determined by the following equation

$$P_{Beam} = \frac{1}{A_P}\frac{N_R - N_L}{N_R + N_L} = \frac{\epsilon_N}{A_P} \tag{2.1}$$

where A_P is referred to as the analyzing power and N_R (N_L) is the number events produced to right (left) of the vertical scattering. Two methods are used to determine the beam polarization at RHIC.

One method used to measure the beam polarization is based on the asymmetry observed in proton-Carbon (pC) elastic scattering in the Coulomb-Nuclear Interference (CNI) region [28] [29]. During the measurement the experiments stop taking data to allow an ultra-thin carbon ribbon target (30 $\mu g/cm^3$) to be inserted into each of the

proton beams. Recoiled carbon nuclei are measured at $\sim 90°$ to the left and right of the target using silicon detectors. The large cross-section and large asymmetry of pC elastic scattering allows for a relatively fast measurement of the polarization. Therefore, the beam polarization can be calculated several times within a long fill, which could last for many hours. Each measurement takes less than two minutes to reach a statistical accuracy of about $\pm 2\%$. However, the analyzing power of pC interactions is not as well known at RHIC energies. Therefore, the pC polarimeters are used to determine the relative polarization from fill to fill.

The H-jet polarimeter provides RHIC with an absolute polarization, which is required to properly normalize the relative polarizations measured by the pC polarimeters. A jet of highly polarized hydrogen gas is inserted transversely to the proton beams at the 12 o'clock interaction region. Elastically scattered protons are detected by silicon strip detectors located at 90° to the left and right of the target as shown in Fig 2.2.

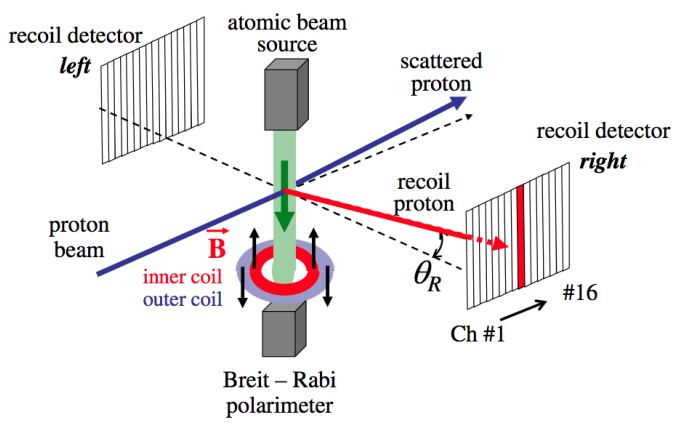

Figure 2.2: **The Hydrogen Jet Polarimeter** - Schematic of the hydrogen jet polarization experiment [30].

The analyzing power in the H-jet polarimeter for the beam and for the target is the same, both the beam and the target are polarized protons, and can be expressed

as

$$A_P^{pp} = \frac{\epsilon_N^{beam}}{P_{beam}} = \frac{\epsilon_N^{target}}{P_{target}}. \tag{2.2}$$

The absolute beam polarization, P_{beam}, can be written in terms of the target polarization and the raw asymmetries of the beam and target. The beam asymmetry, ϵ_N^{beam} is measured by averaging over the spin states of the target. Similarly, the target asymmetry, ϵ_N^{target}, can be measured by averaging over the spin states of the beam. Finally, the target polarization, P_{target} is measured by a Breit-Rabi polarimeter with an absolute accuracy of 2% and the absolute beam polarization can be expressed as

$$P_{beam} = \frac{\epsilon_N^{beam}}{\epsilon_N^{target}} P_{target}. \tag{2.3}$$

The narrow thickness of the atomic hydrogen beam, $\sim 10^{12}$ atoms/cm^2, permits a continuous operation of the polarimeter without largely effecting the RHIC beams. However, the cross section for this elastic pp scattering process is rather small. This results in the measurement needing a longer duration of time to integrate over, much longer than the elastic pC measurement. [31]. The ratio of the polarizations obtained by the pC and H-jet polarimeters results in a normalized polarization value for each beam over each fill.

2.2 The STAR Detector

The Solenoid Tracker at RHIC (STAR) is a large acceptance detector designed to reconstruct the particles from a wide variety of collisions. Fig 2.3 shows a cross-sectional view of the STAR detector. Located at the 6 o'clock position on the RHIC ring, the blue beam comes from the East end and the yellow beam comes from the West end. The STAR coordinate system has its origin at the interaction point with the positive z-axis point to the west along the beam line and the y-axis points up.

The STAR detector is actually a system of sub-detectors. The sub-systems are the Time Projection Chamber (TPC) [$|\eta| < 1.3$] [32], the Time of Flight (TOF) [$|\eta| <$

1.3] [33], the Solenoid Magnet [34], the Barrel Electromagnetic Calorimeter (BEMC) [$|\eta| < 1.0$] [35], the End-cap Electromagnetic Calorimeter (EEMC) [$1.0 < \eta < 2.0$] [36], and the Beam-Beam (BBC) [37] and Zero-Degree Counters (ZDC) [38]. The coverage in pseudo-rapidity, η, is given in parenthesis and defined as

$$\eta = -\ln\left[\tan\frac{\theta}{2}\right] \tag{2.4}$$

where θ is the angle between the particle momentum and the beam axis. It is often used in the particle physics experiment due to its invariance under Lorentz boosts.

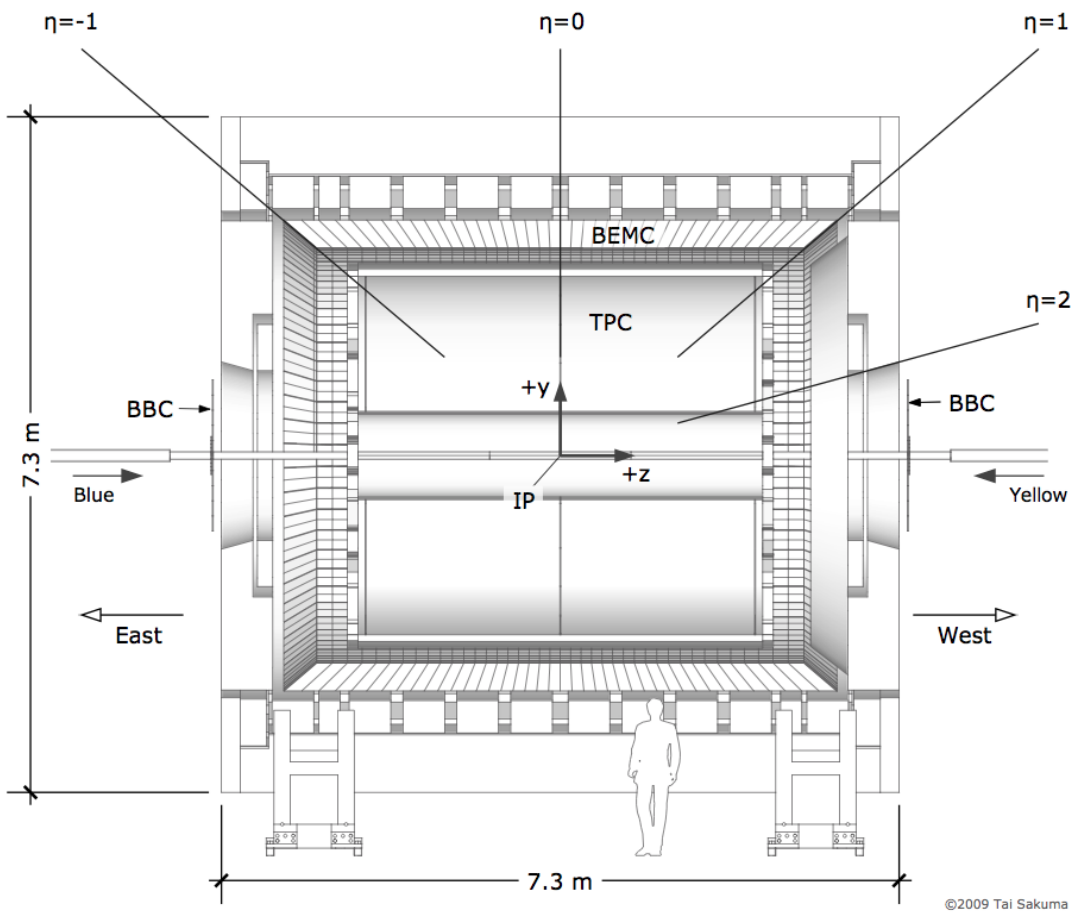

Figure 2.3: **The STAR Detector** - The figure shows the sub-systems composing the STAR detector except for the ZDC and TOF detectors.

2.2.1 Solenoidal Magnet

The magnet subsystem provides the STAR detector with a magnetic field parallel to the beam direction, which operates at a field range of 0.25 T $< |B_z| <$ 0.5 T. It consists of current carrying aluminum coils and a steel structure that acts as the mechanical support for many of the other sub-detectors. This thesis analyzes data taken with a magnetic field of $B = 0.5$ T.

There are three types of magnet coils: the main, space trim and poletip trim coils. The main and space trim coils have an inner diameter of 5.3 m and outer diameter of 6.0 m. The main coils have an axial thickness of 0.45 m and the space trim coils have an axial thickness of 0.23 m. The space trim and pole-tip coil were tuned to improve the uniformity of the magnetic field to a few percent [34]. At the maximum field of 0.5 T the current through the main coils is 4500 A, with an additional 12-13% current through the space trim coils. The total power consumed is 3.5 MW.

2.2.2 Time Projection Chamber

The TPC is a 4.2 m long cylinder with a diameter of 4 meters. A thin conductive central membrane located in the x-y plane, bisects the cylinder forming an East and West end of the TPC as shown in Fig 2.4. It is housed within a large solenoidal magnet that operates at 0.5 T, which bends the tracks of the charged particles coming from a collision. This track curvature is needed to determine the momenta and charge sign of the outgoing particles. These particles, often called the ionizing particles, have enough energy to easily ionize the P10 gas (10% methane, 90% argon) within the TPC drift volume.

A uniform electric field $\sim$ 135V/cm, pointing in $\pm z$ directions and defined by the central membrane, concentric field-cage rings and the readout end caps, allows the ionized electrons to drift toward the readout end caps. The endcaps of the TPC are held at ground potential and the central membrane cathode is held at +28 kV.

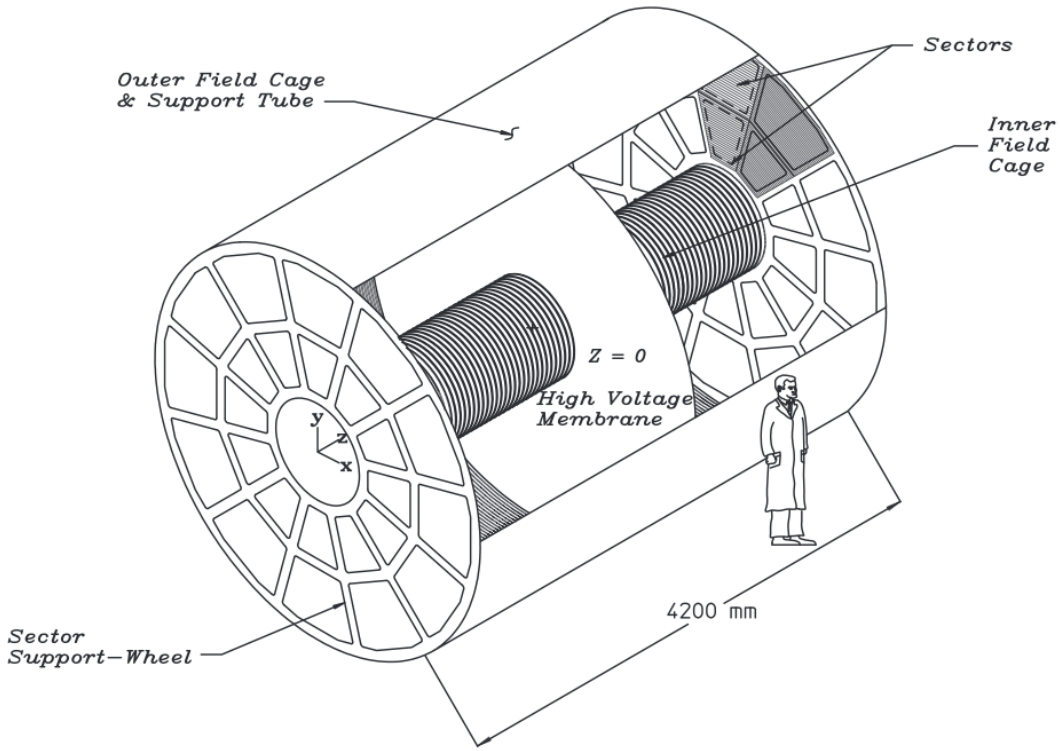

Figure 2.4: **The Time Projection Chamber** - Schematic diagram of the entire TPC. The STAR TPC surrounds the interaction region at RHIC. The collisions take place near the center of the TPC [32].

There are 12 sectors or readout modules, arranged as on a clock face, mounted on the support wheel at each end of the TPC. Each sector is then divided into an outer and inner sub-sector as shown in Fig 2.5. The outer sub-sector has a continuous pad coverage used to optimize the dE/dx resolution and improvement in tracking resolution. The inner sub-sector, a region with high track multiplicity, uses separated pad rows with smaller pad sizes needed for good hit resolution.

The Multi-Wire Proportional Chamber (MWPC), located at the readout end caps, consists of the pad plane and three wire planes as shown in Fig 2.6. The outermost wire plane on the sector is the gating grid located 6 mm from the shield grid. This grid controls entry of electrons from the TPC drift volume into the MWPC. It also blocks positive ions produced in the MWPC, keeping them from entering the drift volume

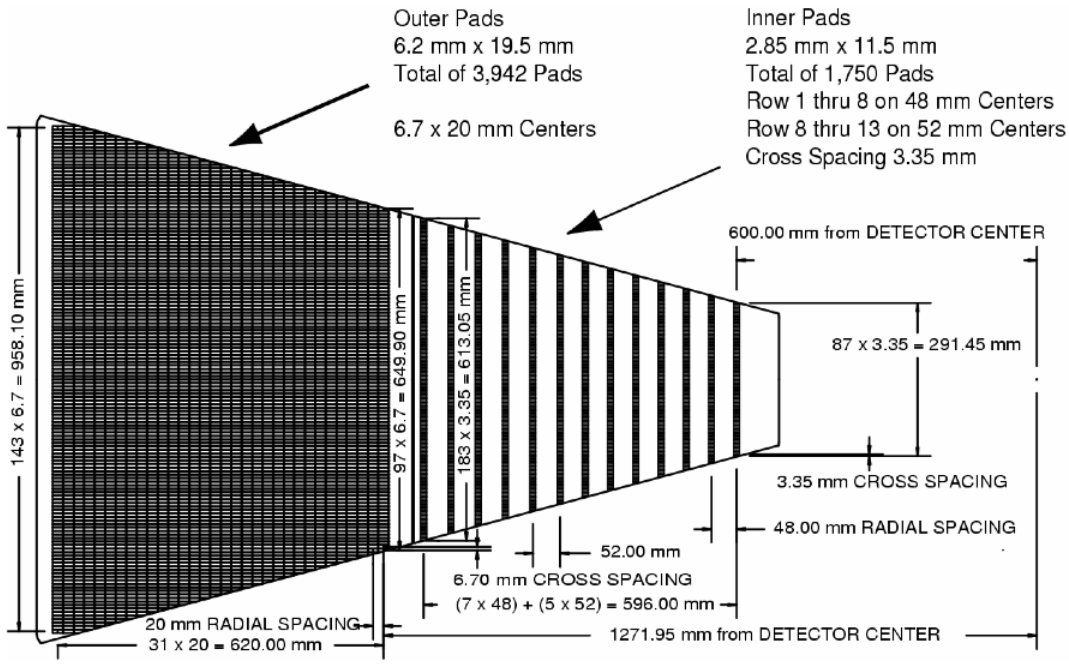

Figure 2.5: **The TPC Sector** - A diagram showing the anode pad planes distributed on one full sector. The inner sub-sector is on the right and it has small pads arranged in widely spaced rows. The outer sub sector is on the left and it is densely packed with larger pads. [32]

and distorting the drift field. The grid is "open" when all of the wires are biased to the same potential (typically 110 V). The grid is "closed" when the voltages alternate ± 75V from the nominal value [32]. Once the drifting electrons reach the MWPC at the ends of the TPC (anode grid), they avalanche in the high fields produced by the 20 μm anode wires providing the necessary amplification to induce a temporary image charge on the pad planes. It is this image charge shared over several adjacent pads that is ultimately measured by the waveform digitizer system, which feeds into a readout board.

The Time Projection Chamber (TPC), the heart of the STAR detector, records the tracks of charged particles as they travel through the detector by measuring their momenta and identifying particles by measuring their ionization energy loss (dE/dx). The TPC has a measurable momenta range from 100 $\frac{MeV}{c}$ to 50 $\frac{GeV}{c}$ and can identify

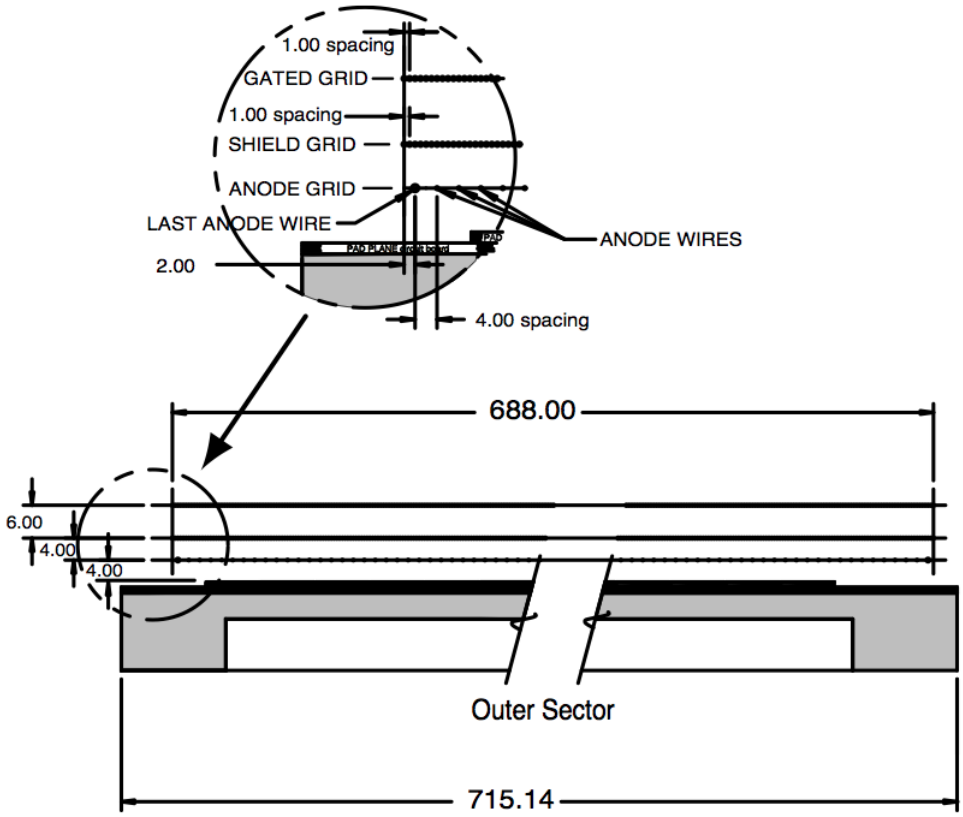

Figure 2.6: **The TPC Multi-Wire Proportional Chamber** - A cutaway view of an outer sub-sector pad plane. The cut is taken along a radial line from the center of the TPC to the outer field cage so the center of the detector is towards the right hand side of the figure. The figure shows the spacing of the anode wires relative to the pad plane, the ground shield grid and the gated grid. The bubble diagram shows additional details about the wire spacing. The inner sub-sector pad plane has the same layout except the spacing around the anode plane is 2 mm instead of the 4 mm shown here. All dimensions are in millimeters [32].

particles with a momentum range of 100 $\frac{MeV}{c}$ to 1 $\frac{GeV}{c}$. [32] This system provides an accurate (within a small fraction of a pad width) measurement of the original track radial position in space. The time taken for the electrons to drift to endcap and the drift velocity of electrons in the P10 gas provides the z position of the track within the TPC. Hence, like a three dimensional camera, we can reconstruct the tracks produced by the ionizing particles as the travel within the Time Projection Chamber.

2.2.3 Space Charge and Grid Leak in the TPC

As discussed in the previous section a uniform electric field is critical to track reconstruction. However, the TPC has several potential sources of field distortions, which must be considered and corrected for in the calibration procedures. While most of these sources are static in time, the buildup of slow-drifting positively charged ions in the gas volume generated from standard operation of the TPC varies with the quantity of charged particles traversing the TPC. Therefore, increases in the luminosity of the collider and/or the multiplicity of charged particles emitted in the collisions will increase the amount of positive charge seen in the drift chamber[39].

The variations in this "space charge" (SC) can occur on time scales of ~ 0.5 sec, the time it takes for the positive ions to drift the length of the chamber. This time is relatively long compared to the drifting ionized electrons ($\sim 40\ \mu s$) and therefore affects multiple colliding events. These positive ions distort the electric field created by the TPC hardware and displaces the position of the reconstructed TPC tracks. Fig 2.7 provides the simulated potential created by this positive charge. The principle distortion is azimuthal and has the effect of rotating the tracks in the transverse plane midway along their path through the TPC

However, this is not the only source of positive charge within the TPC drift chamber. The STAR TPC was designed with a gated grid to prevent the ions created in the high gain region around the anode wires from leaking into the TPC main

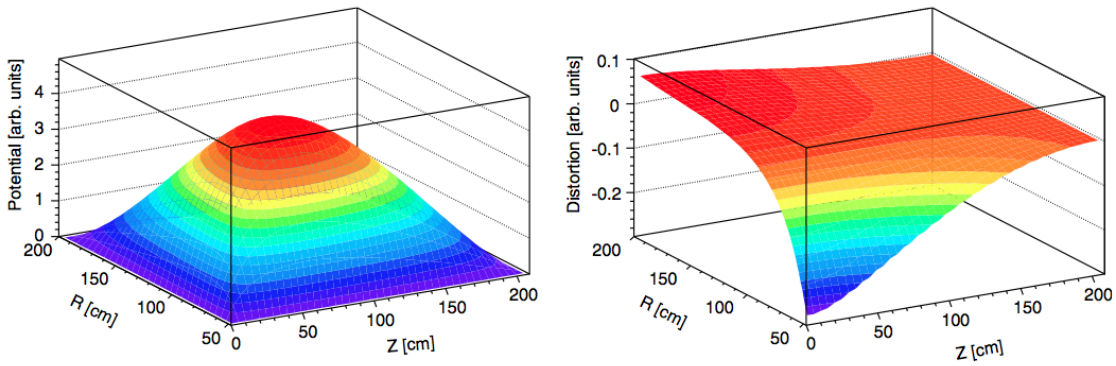

Figure 2.7: **Space Charge Potential and Distortions** - Simulated shape of the potential due to space charge in the TPC (left) and the azimuthal distortions of electron clusters (right) caused by drifting through that potential as a function of radius R and drift Z. The cathode is at Z = 0, and electron clusters drift to the endcaps at high Z [39].

volume and drifting across to the cathode. The recent increase in luminosity has caused this preventative method to become ineffective at completely stopping the positive ions. This causes a thin sheet of positive charge to leak around the edge of the grid between the inner and outer sectors ($\sim$ 119 cm from the detector center). Studying the difference between TPC hit positions and the track fit to these positions, referred to as the residuals, reveals the sources of positive ions seen in the TPC. If the TPC hits fall along the fit track then the residuals will be small, ideally zero. Large residuals point to a mismatch between the hits and the fit and most often occur at the sector boundaries where the position ion current distorts the hit positions. Fig 2.8 shows the sudden reduction in the fit residuals at the gap between the inner and outer readout wire chambers before (left) and after (right) the corrections are performed. Figure 2.5 shows the inner and outer sub-sectors of the TPC and gap between them.

The build up of positive charge inside the TPC increases with increasing luminosity. Unfortunately, high luminosities are required to achieve the RHIC spin physics goal in a reasonable time. Therefore, it is necessary to properly account for the distortion to the TPC tracks and move them back to their original position. There are

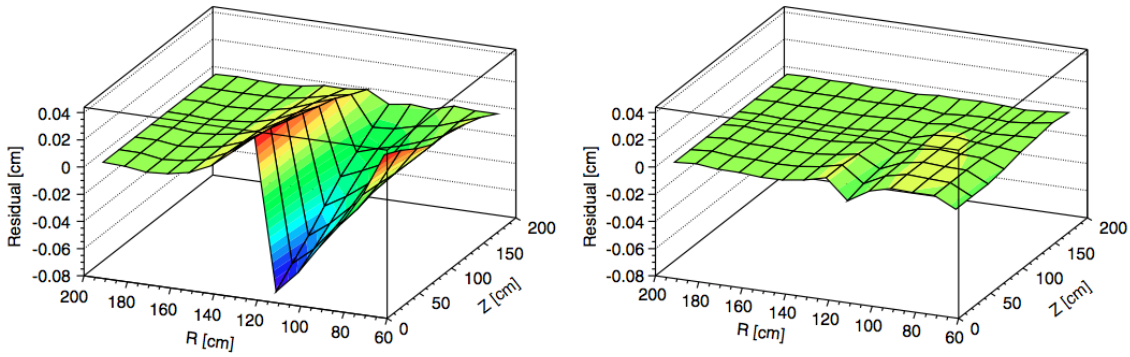

Figure 2.8: **Grid Leak Residuals** - Residuals of TPC tracks over R and Z in a selection of events acquired during high luminosity before (left) and after (right) leakage distortion corrections. The gap between inner and outer wire chambers is at R $\approx$ 122 cm.[39].

two observables used to quantify the amount of positive charge within the TPC: the signed distance of closest approach (sDCA) and the z component of the difference between the residuals between the inner and outer sectors (gapf). The sDCA for each track is the closest measured distance from the vertex position and the position of that track. Simulations have shown that for any distortion to the primary particle track its sDCA is linearly proportional to the amount of positive charge in the TPC such that

$$C^{sim}_{track} = (\rho^{sim}_{SC} + \rho^{sim}_{leak})/sDCA^{sim}_{track} \tag{2.5}$$

where $\rho^{sim}_{SC}$and ρ^{sim}_{leak} are the simulated charge densities from built up space charge and grid leak, respectively. C^{sim} is the linear correction factor that relates the space charge density and the signed DCA, which depends on the location of points on a track. Therefore, as the build up of positively charged ion increases, the sCDA of the track also increases. The observed correction used to account for the distortions is

$$(\rho^{obs}_{SC} + \rho^{obs}_{leak}) = (\rho^{sim}_{SC} + \rho^{sim}_{leak}) \cdot sDCA^{obs}_{track}/sDCA^{sim}_{track} \tag{2.6}$$

In addition, a calibration was performed that found a linear relation, $\rho_{leak} =$

$D \cdot \rho_{SC}$, between the charge densities of space charge and grid leak. The observables are expressed as

$$sDCA = A < \rho_{SC} > + B < \rho_{leak} > \tag{2.7}$$

$$gapf = D < \rho_{leak} > \tag{2.8}$$

where the constants A,B and D are determined from the modeled simulations. If we define the space charge per unit length of the TPC as $SC = \frac{<\rho_{SC}>}{L}$ and the grid leak per unit length of the TPC as $GL = \frac{<\rho_{leak}>}{<\rho_{SC}>}$ this allows us to express the above equations as

$$\frac{sDCA}{L} = A \times SC + B \times (SC \times GL) \tag{2.9}$$

$$\frac{gapf}{L} = D \times (SC \times GL). \tag{2.10}$$

The gives two equations and two unknowns, a completely solvable expression. This calibration is an iterative method starting with the calibration parameters from the previous runs. For example in the case of Run9 pp200 GeV, the initial parameters used were Run6 pp 200 GeV SC and GL calibration parameters. The calibration is repeated until all the parameters converge to stable values.

2.2.4 The Time Of Flight and the pseudo Vertex Position Detector

The time of flight system installed at the STAR experiment is used for the purpose of direct identification of hadrons in Au+Au collisions. The system consists of two detectors, one called the pVPD (pseudo-vertex position detector) and the other referred to as the TOF (time of flight). The pVPD ($4.24 \leq \eta \leq 5.1$ coverage) and TOF (with 72% of the full detector installed in 2009) measures the start and stop

time, respectively. Together these detectors provide the time interval measurements of interest.

The pVPD consists of two identical detector assemblies that are positioned very close to the beam pipe. They are positioned outside of the STAR magnets, one on each side of STAR, at a $|z|$ position around 4.5 m. The TOF sits inside the STAR magnet immediately outside the TPC [33]. A diagram of the TOF location for one tray is shown in Fig 2.9. The reconstruction of jets does not require particle identification so the TOF was not used in this analysis.

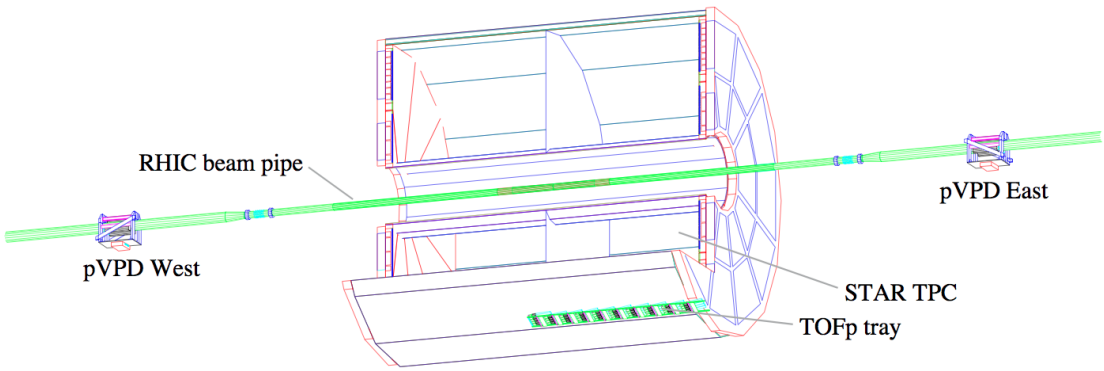

Figure 2.9: **The TOF and VPD schematic** - A scale drawing of the locations of the pVPD and the TOFp detectors in relation to the STAR TPC and the RHIC beam pipe. For clarity, the TPC is cut away, while the STAR magnet and other subsystems are not drawn [33].

2.2.5 The Barrel Electromagnetic Calorimeter

The Barrel Electromagnetic Calorimeter (BEMC) allows for the detection of electromagnetically interacting particles, such as electrons and photons, from their energy deposition in the detector [35]. It also provides STAR a fast detector that can be utilized for trigger purposes. The design for the Barrel Electromagnetic Calorimeter includes a total of 120 calorimeter modules, each covering 6° in $\Delta\phi$ and 1.0 unit in $\Delta\eta$. The modules are positioned with 60 on the West end and 60 on the East end. The modules are segmented into 40 towers, 2 in ϕ and 20 in η; making each tower

covering 0.05×0.05 in $\eta - \phi$ space. Therefore, the full Barrel Calorimeter consist of a total of 4800 towers projecting back to the center of the interaction region. The deposition of energy in the individual towers, or a sum of towers, can be used to trigger on high transverse momentum (p_T) events. This capability provides STAR access to study rare high p_T processes such as jets, leading hadrons, heavy quarks, etc.

Each tower consists of an alternating lead-scintillator stack and a shower maximum detector (SMD) situated at ∼5 radiation lengths. The 20 lead layers and 19 plastic scintillator layers within the stack are 5 mm thick and the first two layers of the plastic scintillators are 6mm thick. Figure 2.10 shows one of 4800 calorimeter towers. The first two thicker layers are known as the pre-shower detector. The SMD and pre-shower detectors can provide electron, hadron and π^0 reconstruction, but they are not needed for jet reconstruction.

2.2.6 The EndCap Calorimeter

A single EndCap Calorimeter (EEMC) was installed on the West pole-tip of the STAR detector and provides full azimuthal coverage within an pseudorapidity range of $1.0 < \eta < 2.0$. Traditional Pb/plastic scintillator calorimeter towers are used, which is consistent with the STAR BEMC. In total there are 720 projective towers in the Endcap and just like the BEMC they can be used for triggering purposes. Figure 2.11 provides a schematic of the detector. The analysis of this thesis focuses on the mid-rapidity region and only uses the EEMC for triggering purposes.

2.2.7 Zero Degree Calorimeter

Each of the RHIC experiments constructed a pair of Zero Degree Calorimeter (ZDC) detectors to provide the accelerator operators a common tool for monitoring interactions at each region. These are placed at nearly identical positions, $\sim$ 18 m on either

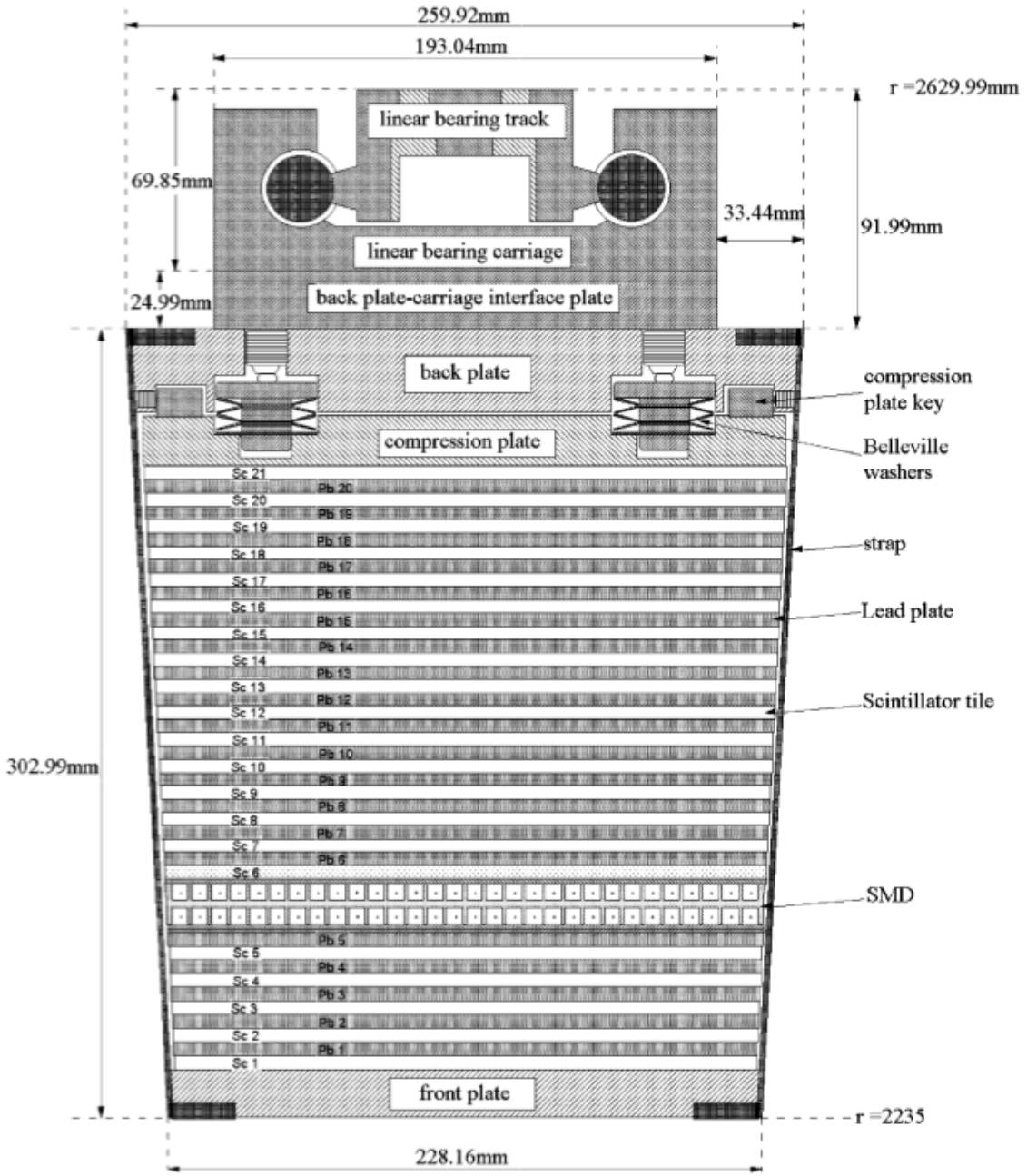

Figure 2.10: **A BEMC Tower** - Schematic of a side view of a STAR EMC module showing the compressed components. [35]

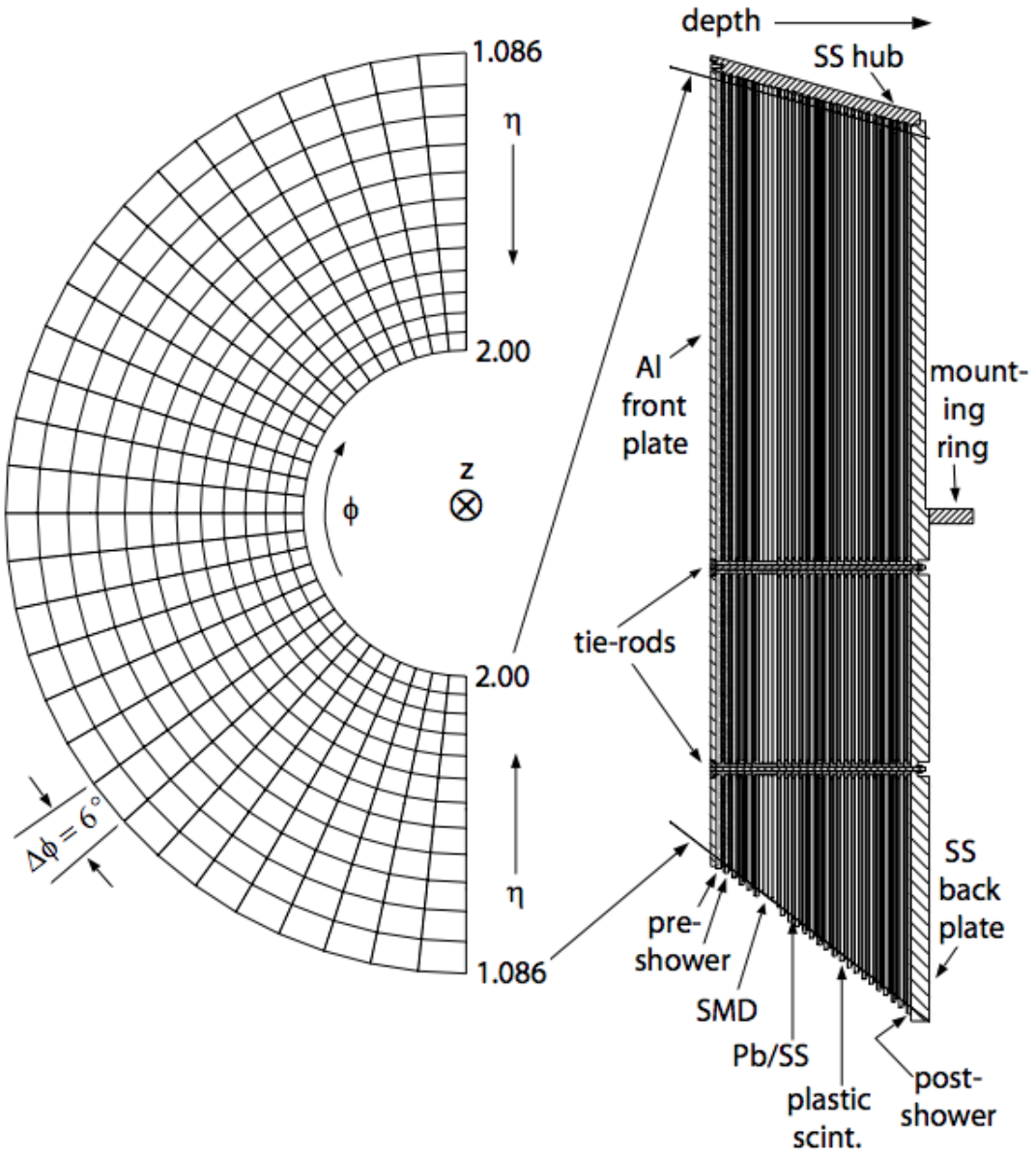

Figure 2.11: **The Endcap Calorimeter** - A cross-sectional view of the Endcap calorimeter. [36]

side of the interaction region, with an acceptance of 4 mrad from the beamline. Each ZDC consists of three modules constructed from a series of tungsten plates alternating with layers of wavelength shifting fibers that route Cherenkov light to a PMT. The design of the modules is shown in Fig 2.12. They detect neutrons emitted from the beam collision. The ZDCs are used for beam monitoring, triggering, and locating interaction vertices. Comparison of the time an interaction occurs in the ZDCE and in the ZDCW gives a measure of the interaction location. Many of our triggers cut on the location of the interaction vertex. [40]

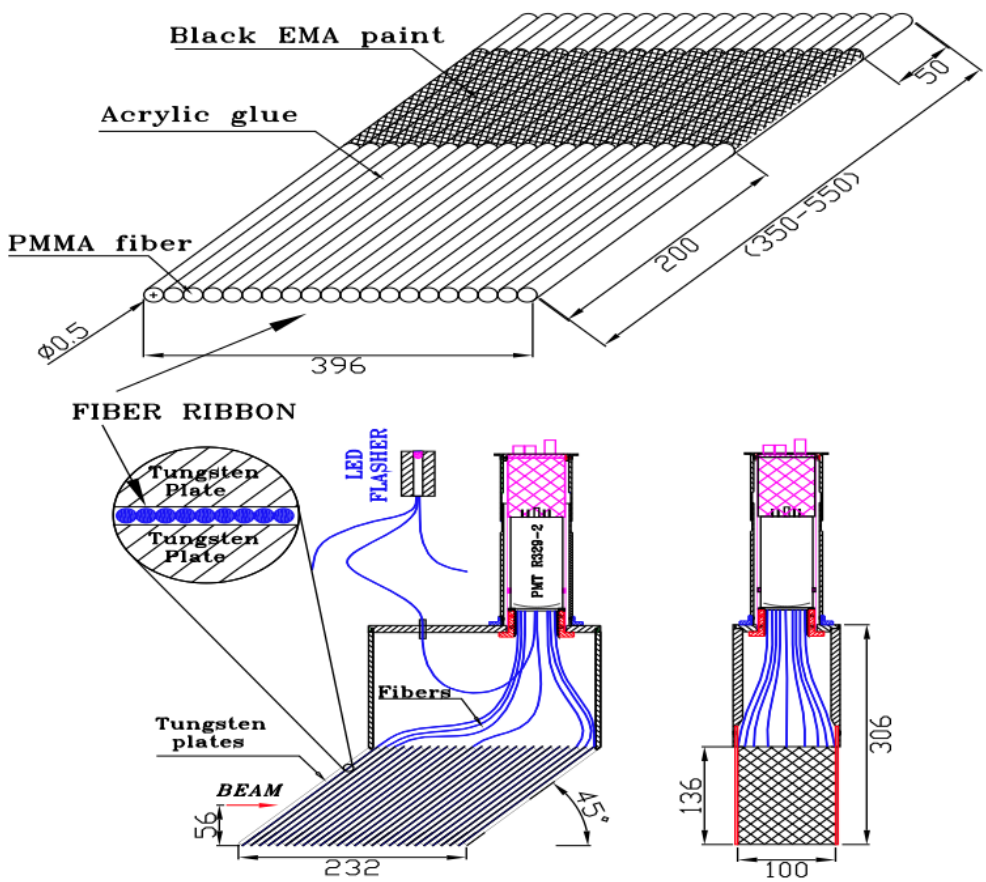

Figure 2.12: **ZDC Module** - Mechanical design of the tungsten models. The dimensions shown are in millimeters. [38]

2.2.8 Beam-Beam Counter

The Beam-Beam Counters (BBC) at STAR are used for three purposes: (i) a measure of luminosity, (ii) triggering, and (iii) local polarimetry. The BBC consists of scintillator annuli mounted around the beam pipe beyond the East and West pole-tips of the STAR magnet at 374 cm from the interaction point [37]. Figure 2.13 displays the hexagonal tiles that offer full azimuthal coverage in the pseudorapidity range of $2.2 < |\eta| < 5.0$. There are 36 tiles in total with 18 small tiles (1-18) close to the beamline and 18 surrounding large tiles (19 - 36). A signal from any of the 18 inner tiles on the East side and any of the 18 inner tiles on the West side within a short timing window results in a BBC coincidence. This BBC coincidence provides a baseline minimum bias (MB) trigger for the STAR detector. The number of BBC coincident events is a measure for the luminosity. The BBC acceptance amounts to $\sim 53\%$ of the total proton-proton cross-section of $\sigma_{tot}^{pp} = 51$ mb at a center of mass energy of 200 GeV. [37].

The BBC is also used as a local polarimeter at the STAR detector. The particle yields of transversely polarized proton beam collision have a ϕ dependence. Therefore, the size of the left-right asymmetry indicates the extent of the transverse component of the beam polarization. At RHIC both beams are polarized, which means one needs to sum over the yields for both spin states for one beam to measure the single spin asymmetry of the other beam. One beam is considered to be polarized and the other unpolarized and vise versa. The conditions for a right scattered event is indicated in Fig 2.13.

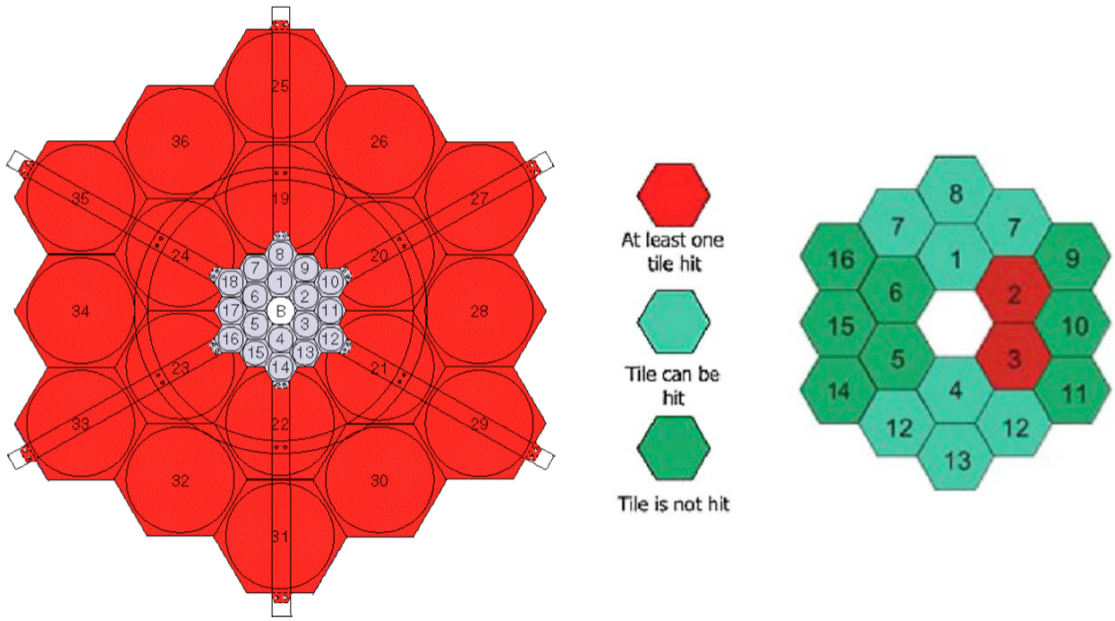

Figure 2.13: **Front View of the BBC** - The left figure shows the entire schematic of one of the BBC detectors. The right figure displays a zoomed in picture of the inner 18 scintillators and indicates the conditions for a right scattered event. The red tiles must have a least one hit, the dark green tiles must not have a hit, and there is no constraint on the light green tiles.

2.3 Triggers

It is not feasible to record every event that occurs within the STAR detector. There are many reasons why it's not possible; the main ones being:

1. many events are not of physics interests
2. bandwidth limitations (the rate at which data is taken)
3. disk space limitations (space to store date)
4. CPU limitations (processors require to reconstruct all the data).

Therefore, only the events that satisfy certain trigger conditions are recorded. When those conditions are met, the event has fired a trigger in the STAR detector and is recorded.

The triggers used in this thesis are the BHT3 (Barrel High Tower 3), JP1(Jet Patch 1), and JP2 (Jet Patch 2) triggers. A barrel high tower trigger requires a minimum transverse energy E_T deposited in a single BEMC tower. A jet patch trigger requires a minimum energy deposited in a patch of calorimeter towers, 400 towers in total, that are approximately the size of a jet cone. The barrel is divided into 18 jet patches, 6 each on the East end, 6 on the West end, and 6 overlapping jet patches with their centers at $\eta = 0$. The details of the trigger conditions are summarized at Table 2.1.

			Threshold	
	ID	$\Delta\eta \times \Delta\phi$	DSM ADC	E_T
BHT3	230531	0.05×0.05	31	$\sim$ 6.1 GeV
JP1	230410	1.0×1.0	40	$\sim$ 8.3 GeV
JP2	230411	1.0×1.0	60	$\sim$ 13.0 GeV

Table 2.1: Trigger Conditions

The jets in a triggered data sample often have very different characteristics (neutral energy fraction, average p_T, vertex distribution) from those reconstructed in a minimum bias sample. In order to understand and quantify the biases imposed on the data sample from the trigger the jet sample is separated into jets that could have caused the trigger and those that could not. If a jet points to a jet patch with energy exceeding the trigger threshold then this jet is called a trigger jet. This requires the separation of jet axis and the middle of a jet patch to be within $\Delta R = \sqrt{(\eta_{jet} - \eta_{JP})^2 + (\phi_{jet} - \phi_{JP})^2} \leq 0.4$. In the dijet analysis, at least one jet of the dijet pair is required to be a triggered jet.

2.4 Luminosity

The vernier scan technique was used to measure the total cross-section of BHT3 triggered events for the first RHIC proton run with a beam energy of 250GeV[41].

In this technique the position of one of the two beams is deliberately altered, in the x-direction and then in the y-direction, while taking data. The luminosity is defined to be the overlap integral of the transverse particle density of the colliding beams. For bunched beams the z-integral over the length of the bunch size is performed, which determines the intensity of each bunch measured using a scan by the Wall Current Monitors (WCM) [42]. Assuming a gaussian distribution in the x and y component the luminosity can be expressed as

$$L = \sum_i f_{rev} \int_{-\infty}^{\infty} dx \int_{-\infty}^{\infty} dy N_{1i} g(\sigma_{1x}, x) g(\sigma_{1y}, y) N_{2i} g(\sigma_{2x}, x) g(\sigma_{2y}, y) \tag{2.11}$$

where $N_{1(2)i}$ is the number of ions in the ith bunch in beam 1(2) and $g(\sigma_{1(2)x}, x)$ and $g(\sigma_{1(2)y}, y)$ are the gaussian distributions in the x-direction and y-direction with a width of $\sigma_{1(2)x}$ and $\sigma_{1(2)y}$ respectively. The revolution frequency of the beams is f_{rev}. For head-on collisions the luminosity is

$$L_0 = \frac{N_1 N_2 f_{rev}}{2\pi\sqrt{(\sigma_{1x}^2 + \sigma_{2x}^2)(\sigma_{1y}^2 + \sigma_{2y}^2)}}. \tag{2.12}$$

which is the integration of the Eq. 2.11. For beams that do not collide head on an offset is applied which alters the luminosity equation above as follows

$$L(\Delta x, \Delta y) = L_0 e^{\frac{-\Delta x^2}{2(\sigma_{1x}^2 + \sigma_{2x}^2)}} e^{\frac{-\Delta y^2}{2(\sigma_{1y}^2 + \sigma_{2y}^2)}} \tag{2.13}$$

which can then be related to the collision rate for a given process by the following:

$$R(\Delta x, \Delta y) = \sigma_{event} \cdot L(\Delta x, \Delta y). \tag{2.14}$$

The cross section can be the be extracted by

$$\sigma_{event} = \frac{R(\Delta x, \Delta y)}{L(\Delta x, \Delta y)}. \tag{2.15}$$

where in the vernier scans δx and δy are known and the widths $\sigma_{x(y)}$ are determined from gaussian fits of the overlap region. Two usable vernier scans were performed

during the 2009 $\sqrt{s} = 500$ GeV data, which operated using only the fast STAR subdetectors. Taking data with only the fast detectors, such as the BEMC, minimized the dead-time effects. The STAR BHT3 trigger was the main absolute luminosity monitor in the 2009 proton-proton collisions at $\sqrt{s} = 500$ GeV. However, in order to reduce background rates an addition coincidence condition was required. The BHT3+coincidence trigger locates the trigger patch with the highest ADC in the event, then adds the ADCs from all trigger patches 10 or more patches away in azimuth and the summed away-side ADC must be greater than or equal to 98 [43]. Each vernier scan was analyzed separately and the results were averaged to obtain an effective cross section of $\sigma^{2009}_{BHT3+coin} = 434 \pm 7$ (stat) nb $\pm 13\%$ (syst) [44].

A major contribution to the systematic uncertainty are the possible non-gaussian components in the beam profile. This non-gaussian behavior is measured by comparing the full fit of the entire data to partial fits of sections of the data, which was determined to give a 10% uncertainty. The next largest uncertainty of the effective cross-section is a 5% uncertainty due to the possible drift of trigger patch gains over the course of the run. This was estimated by altering the ADC values by ± 1. Details on the vernier scan technique and all the systematics, beyond the brief description presented here, can be found at the following Refs [41] [43].

The integrated luminosity for this analysis was calculated from the number of BHT3 triggers in the events used for the dijet cross section measurement and the cross section determined from the vernier scan. The number of recorded BHT3 dijet events for this analysis is

$$N^{recorded}_{BHT3} = 3787534. \tag{2.16}$$

However, we want to measure the dijet cross-section for the JP2 trigger, which has a different dead time than the BHT3 trigger. Therefore, the ratio of the BBCMB_Cat2 and BBCMB_Cat3 trigger rates, which have the same dead-times as the JP2 and

BHT3 triggers respectively, is calculated. The trigger deadtime discrepancies are corrected by the following ratio:

$$R_{BBCMB} = \frac{N^{recorded}_{BBCMB_Cat2}}{N^{recorded}_{BBCMB_Cat3}} = \frac{854931}{827881} \sim 1.033 \tag{2.17}$$

In addition, it is important to note that the cross-section used for the vernier scan was used with BHT3+coincidence trigger, which is a similar trigger for the W-analysis. This coincidence is not a requirement in the dijet analysis. Therefore, using the exact number of runs for the W analysis, the luminosity for the BHT3 trigger (without the coincidence requirement) is

$$\left(\int Ldt\right)_{W-analysis} = \frac{N^{W-analysis}_{BTH3}}{\sigma^{2009}_{BHT3+coin}} = \frac{3739733}{434} = 8.616pb^{-1} \tag{2.18}$$

and the total luminosity for W-analysis using the L2W trigger is 8.0948 pb^{-1}. Correcting our luminosity by the fraction

$$R_{W-analysis} = \frac{\int Ldt^{BHT3}_{W-analysis}}{\int Ldt^{L2W}_{W-analysis}} = 0.9394. \tag{2.19}$$

resolves the issues of the coincidence requirement in the vernier scan.

Therefore, the total integrated luminosity for this analysis for the JP2 trigger is

$$\int Ldt = \frac{N^{recorded}_{BHT3} * R_{BBCMB} * R_{W-analysis}}{\sigma^{2009}_{BHT3+coin}} = 8.47pb^{-1} \tag{2.20}$$

Chapter 3 Jet Algorithms

3.1 Jet Definition

In the STAR experiment, two highly energetic partons collide, elastically scatter off one another and then undergo fragmentation and hadronization. The spray of particles produced during hadronization then reach the detectors where they leave tracks of their path and deposit energy. This process leads to the reconstruction of jets at three different levels: detector-level jets, particle-level jets and parton-level jets.

Detector level jets consist of the collection of energy deposited in BEMC towers and charged tracks reconstructed in the TPC. The collimated bunches of stable hadrons and other particles moving in nearly the same direction are referred to as particle-level jets. The collection of partons prior to non-perturbative effects, such as hadronization, are known as parton jets.

Jet-finding algorithms attempt to correlate clusters of particles detected in an experiment with the properties of the original quark and gluon participants. Comparisons between measured jet observables and pQCD predictions are only meaningful if the jet algorithm is well defined and consistent at all levels. In the later sections two jet reconstruction algorithms are discussed and analyzed.

3.2 Jet Algorithms

Many types of jet algorithms have been developed and implemented in high energy experiments[5] [45] [46]. Every jet algorithm begins with a list of partons, particles, or detector responses. A jet-finding algorithm then clusters these objects into jets in such a way that the jet's kinematic properties correlate to the properties of the

partons produced in the hard scattering process. Nearly 30 years of jet studies has made clear there is no unique or preferred algorithm for defining a jet. Instead, the jet algorithm must be choose to fit the experimental conditions and physics goals.

3.2.1 An Ideal Algorithm

Prior to the discussion of some specific jet-finding algorithms, we will first examine the ideal theoretical and experimental criteria for jet reconstruction.

Ideal Requirements:

- infrared safe
- collinear safe
- invariance under longitudinal boosts
- order independence: same jets reconstructed at the parton, hadron and detector level.
- independence of the detailed detector geometry and granularity
- minimal sensitivity to non-perturbative processes and multiple scatterings at high luminosity
- minimization of resolution smearing/angle bias
- maximal reconstruction efficiency (find all jets) vs minimal CPU time
- replicate cross sections while avoiding theoretical problems.

The conditions described above are fairly self-explanatory except for the first two requirements, which are very important in jet reconstruction. There is always some emission of soft particles (i.e a quark radiates a soft gluon) both through perturbative and non-perturbative effects. This is referred to as infrared radiation and can alter

the number and energy of reconstructed jets. As an example, illustrated in Fig 3.1, two partons which originally formed two separate jets might be combined into a single jet due to a radiated gluon emitted between them.

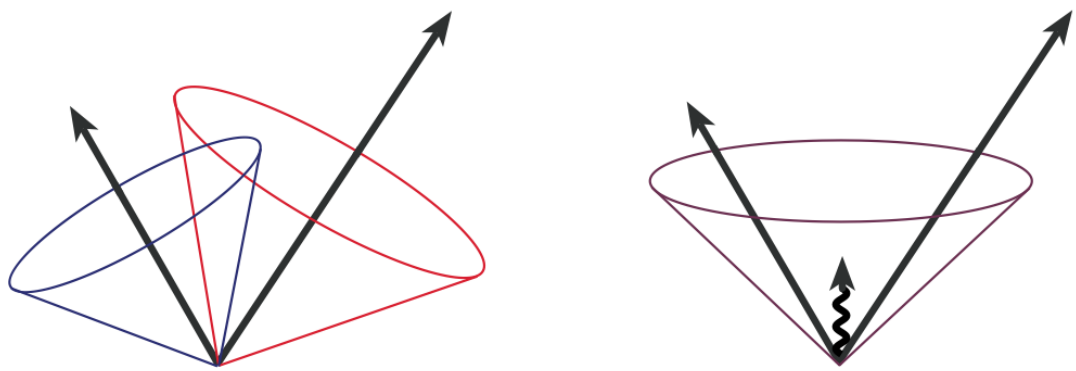

Figure 3.1: **Infrared sensitivity** - An example of how soft radiation between two jets found using a jet algorithm (left) can cause them to merge into one jet (right) [46]

A hard parton can separate or spilt into two or more partons moving close to the same direction, due to fragmentation. This parton underwent a process known as collinear splitting. Jet algorithms that use "seeds", a particle above a particular threshold, in reconstructing jets have problematic issues with collinear splitting. For example, if a parton that was originally used as a seed for a jet splits into two collinear partons and neither of these partons has sufficient energy themselves to be seeds, then the jet will not be reconstructed. This results in the loss of a jet and is diagramed in Fig 3.2. In addition, the ordering of particles in the jet algorithm, such as energy ordering, can effect the jet kinematics due to collinear splitting. The hardest parton is split into two collinear partons causing another parton at a different location to be the hardest parton. This ultimately alters the kinematic properties of reconstructed jets described by Fig 3.3. It would be problematic experimentally and theoretically

if the class of jets reconstructed with a specific algorithm was sensitive to infrared radiation and collinear splitting, which will certainly occur during the scattering, fragmentation and hadronization process.

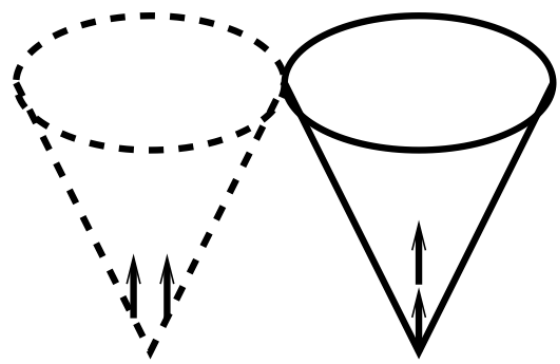

Figure 3.2: **Collinear sensitivity** - The left figure does not produce a seed because energies are spilt among the detectors while the right figure does produce a seed[46].

A jet-algorithm needs to satisfy the majority of the requirements listed in this section. Historically, at the STAR experiment, the mid-point cone algorithm was primarily used. However, the collaboration has strongly considered moving to the anti-k_T jet algorithm. A description and comparison of the midpoint cone and anti-k_T algorithms are discussed in the following sections.

3.2.2 Mid-Point Cone Jet Algorithm

This section focuses on the mid-point cone algorithm[46]. Cone algorithms use the spatial distribution of particles to form clusters that lead to jets and have been widely used in hadron colliders. The algorithm begins by creating a list of seed particles, which pass a certain p_T threshold. In addition, to reduce collinear sensitivity all the midpoints between the seed particles are also included in the seed list. Then using a seed i to set the initial direction, the algorithm sums the momenta of all particles j

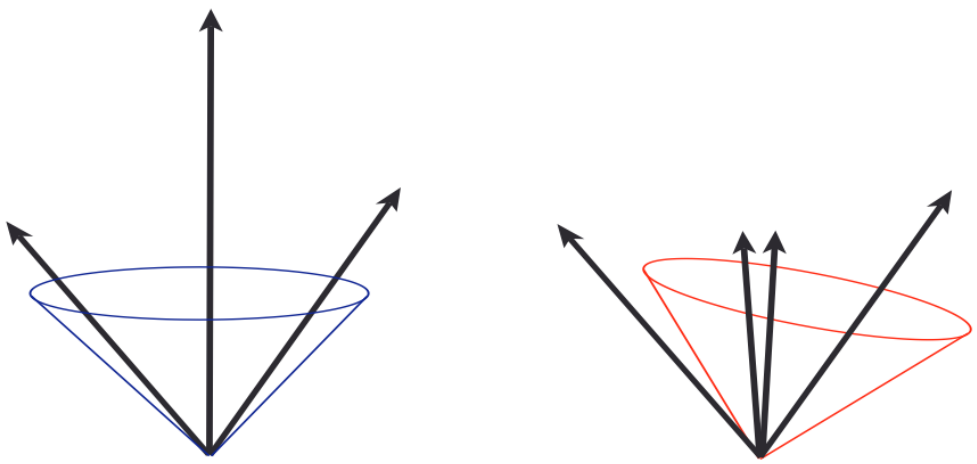

Figure 3.3: **Collinear sensitivity** - An illustrations showing how the ordering in an algorithm can effect the jet kinematics making the algorithm collinear unsafe. The central (hardest) parton splits into two almost collinear partons. On the left, where the single central parton has the largest transverse energy, a single jet containing all three partons will be found. On the right, the splitting of the central parton leaves the right-most parton with the largest E_T. This seed is looked at first and a jet may be found containing only the right-most and two central partons. The left-most parton is a jet by itself. [46].

within a circle of radius R around i in azimuthal angle ϕ and pseudorapidity η. In other word, taking all j such that

$$\Delta R_{ij}^2 = (\eta_i - \eta_j)^2 + (\phi_i - \phi_j)^2 < R^2 \tag{3.1}$$

The radius used in this thesis is $R = 0.6$ (see Section 5.4). The transverse energy, E_T, weighted centroid of the jet is then calculated using all particles within the cone and is compared with the geometric centroid. If the two centroids match then the jet is put into a list of protojets. If the centroids do not match, the E_T weighted centroid is made into a new seed the process is iterated until the centroids match.

Once we have a list of all the protojets, they are then sorted in descending order by the jet momentum. The protojets kinematics were determined using the E-scheme

recombination which is described as follows [46]:

$$p^{jet} = \left(E^{jet}, \mathbf{p}^{jet}\right) = \sum_{i \subset jet} \left(E^i, p_x^i, p_y^i, p_z^i\right) \tag{3.2}$$

$$\eta^{jet} = \frac{1}{2} \ln \frac{|\mathbf{p}| + p_z}{|\mathbf{p}| - p_z} \tag{3.3}$$

$$\phi^{jet} = \tan^{-1} \frac{p_y^{jet}}{p_x^{jet}}. \tag{3.4}$$

Unfortunately, nothing prevents the stable cone protojets from overlapping. A single particle may belong to two or more cones, which should not be allowed to happen. Therefore, prior to obtaining the final list of jets, the algorithm implements a split-merge step. It identifies the hardest overlapping pair of proto-jets and merges (splits) them if they share more (less) than a fraction f of the hardest cone. The split-merge fraction used for this analysis is 50%, which tries to ensure that no final jets share the same particle. Table 3.1 lists the user parameters for the midpoint algorithm .

Cone Radius = 0.6
Spilt/Merge Fraction = 0.5
Seed Threshold > 200 MeV

Table 3.1: Mid-Point Cone Parameters

The mid-point cone algorithm is infrared and collinear safe to NLO. It is not safe at all orders beyond NLO calculations, which is a major theoretical disadvantage . Since the algorithm implements an initial set of seeds, its fails to identify all the stable cones, leading to infrared and/or collinear sensitivity. However, in practice seeds are often needed to save computation time. The STAR experiment has 4800 barrel towers and would it would be very computational expensive to consider each tower as a possible seed.

3.2.3 Anti-k$_T$ Jet Algorithm

In contrast to the mid-point cone algorithm, which uses a clustering process in $\eta - \phi$ space, the anti-k_T algorithm uses the relative momentum between particles to form clusters. The definition of the inclusive anti-k$_t$ jet algorithm is coded is as follows:

1. For each pair of particles i, j work out the distance

$$d_{ij} = \min\left(\frac{1}{k_{ti}^2}, \frac{1}{k_{tj}^2}\right)\frac{\Delta R_{ij}^2}{R^2} \tag{3.5}$$

   with $\Delta R^2 = (y_i - y_j)^2 + (\phi_i - \phi_j)^2$, where k$_{ti}$, y$_i$, and ϕ_i are the transverse momentum, rapidity and azimuth of particle i, repectively. Also, for each particle i work out the beam distance $d_{iB} = 1/k_{ti}^2$.

2. Find the minimum d$_{min}$ of all the d$_{ij}$, d$_{iB}$. If d$_{min}$ is a d$_{ij}$ merge particles i and j into a single particle, summing their four-momenta (this is the E-scheme recombination); if it is a d$_{iB}$ then declare particle i to be a final jet and remove it from the list. [47]

3. Repeat from step 1 until no particles are left.

While the concise description above of the anti-k$_T$ algorithm is accurate, the prescription remains difficult to intuitively interpret. An excellent example described by Cacciari, Salam and Soyez [45] illuminate the methodology of the anti-k$_T$ algorithm:

> The functionality of the anti-k$_T$ algorithm can be understood by considering an event with a few well-separated hard particles with transverse momenta k$_{T1}$, k$_{T2}$, ... and many soft particles. The $d_{1i} = \min(1/k_{t1}^2, 1/k_{ti}^2)\Delta R^2/R^2$ between a hard particle 1 and a soft particle i is exclusively determined by the transverse momentum of the hard particle and the ΔR_{1i} separation. The d_{ij} between similarly separated soft particles will instead be much larger. Therefore soft particles will tend to cluster with hard particles long before

they cluster among themselves. If a hard particle has no hard neighbors within a distance 2R, then it will simply accumulate all the soft particles within a circle of radius R, resulting in a perfectly conical jet. [45]

If another hard particle 2 is present such that $R < \Delta R_{12} < 2R$, then two hard jets are formed. It is not possible for both to be perfectly conical. If $k_{t1} \gg k_{t2}$ then jet 1 will be conical and jet 2 will be partly conical, sinceIt will miss the part overlapping with jet 1. Instead if $k_{t1} = k_{t2}$ neither jet will be conical and the overlapping part will simply be divided by a straight line equally between the two. For a general situation, $k_{t1} \sim k_{t2}$, both cones will be clipped. Similarly, one can work out what happens with $\Delta R_{12} < R$. Here particles 1 and 2 will cluster to form a single jet.

Hard particles can alter the shape of a jet, but not soft radiation. This ensures the algorithm is infrared and collinear safe at all orders in pQCD, which is a significant theoretical benefit. The anti-k_T algorithm also tends to produce conical jets, similar to the mid-point cone algorithm. This is demonstrated by Fig 3.4, which implements the jet-finding over a simple Monte Carlo sample.

$R = 0.6$

Table 3.2: Anti-k$_T$ user parameters

3.2.4 Comparison of Anti-k$_T$ and Mid-Point Cone Jet Algorithms

It is vital to study an algorithm's characteristics and select the one most appropriate for the proton-proton collisions at STAR. This section compares two prominent algorithms, the anti-k_T and mid-point, by running each jet finder over the 2009 data sample. Although the algorithms are expected to behave similarly, there are substantive differences which are highlighted in this section .

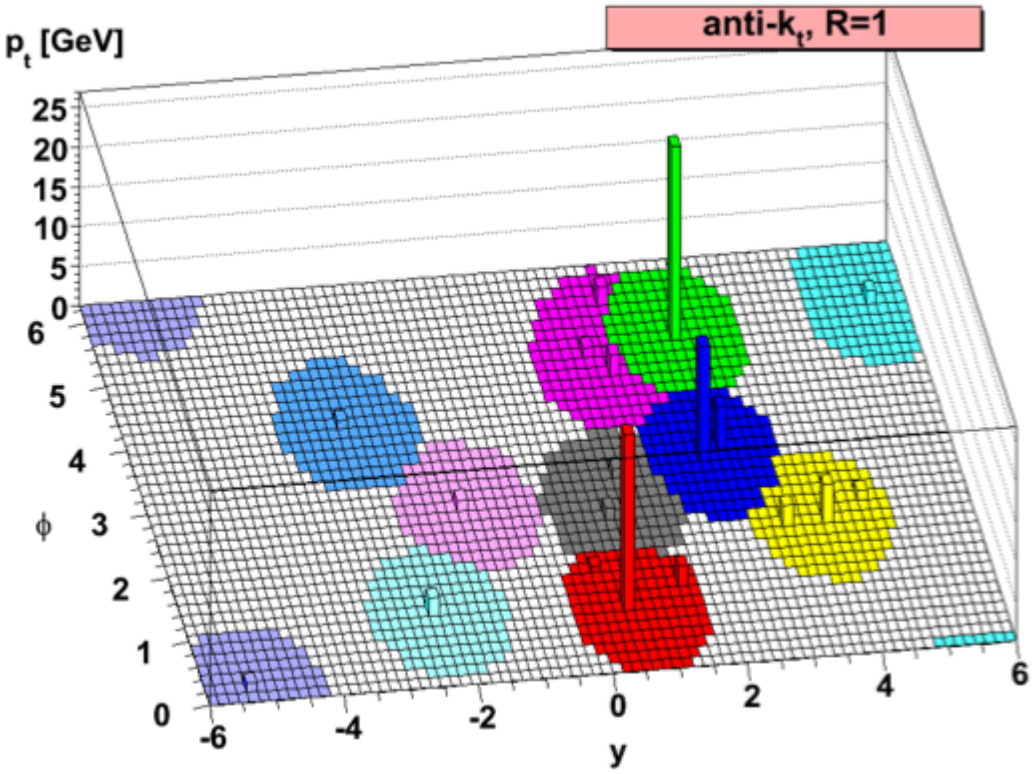

Figure 3.4: **Applied anti-kT Algorithm** - Illustration of the regularity of the jets obtained with the anti-k$_T$ algorithm.[48]

The total number of jets produced by the anti-k$_T$ algorithm and the mid-point cone algorithm are respectively 10.57M and 10.78M jets. As shown in Fig 3.5, the cone algorithm has more events with 3 jets or more. The reason for the increase in the number of cone jets is indicated in Fig 3.6. This figure displays the jet p_T spectrum for both algorithms with the anti-k$_T$ algorithm in black and the mid-point cone algorithm in red. It is clear that the midpoint cone jet p_T spectrum is shifted a bit to the right of the anti-k_T jet p_T spectrum. The mid-point cone algorithm, therefore, must on average sweep up just a bit more energy into the jet than the anti-k_T algorithm, which causes the shift to the right. The cone algorithm then has more jets passing the jet $p_T > 5$ GeV reconstruction threshold causing the overall increase in the number of jets. Specifically, the midpoint cone algorithm obtains ($\sim 2-3\%$)

more high p_T (above ~18GeV) jets than the anti-k_T algorithm and up to $\sim 6\%$ more jets in the very low p_T regime (less than 9 GeV).

Naturally, from the jet p_T spectrum, the number of tracks and towers within a jet is expected to be larger for the mid-point cone algorithm than the anti-k_T algorithm. This is clearly verified by Fig 3.7 and Fig 3.8. The mid-point cone algorithm overall has a much higher multiplicity for both tracks and towers than the anti-k_T algorithm.

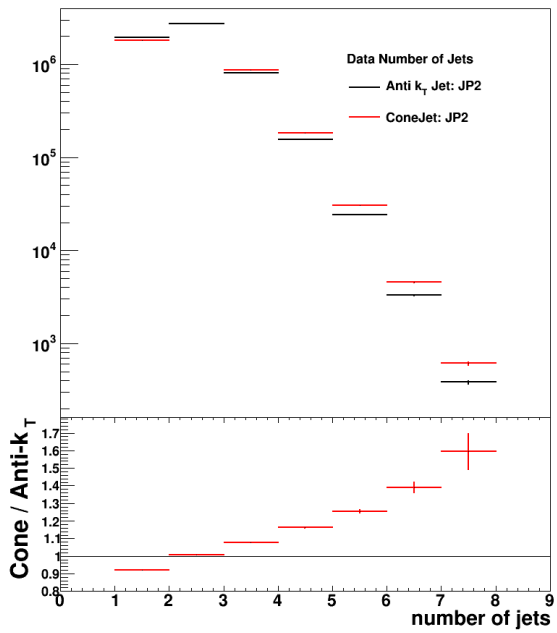

Figure 3.5: **Algorithm Comparison: Number of jets** - Jet number comparison of the Anti-k_T (black) and Cone (red) Algorithms

However, what are the characteristics of these extra tracks and towers within mid-point cone jets? Examining the track p_T and the tower energy spectrums, Fig 3.9 and Fig 3.10 respectively, we observe the midpoint cone algorithm reconstructs jets with more low p_T tracks and low energy towers than the anti-k_T algorithm. In fact, the cone algorithm has $\sim 10\%$ more tracks with a transverse momentum of 0.6 GeV and $\sim 3\%$ more towers at energies of 0.6 GeV.

An interesting finding from this comparison, as seen in Fig 3.11, is the neutral energy fraction (R_T) distributions. Even though the cone algorithm has more low

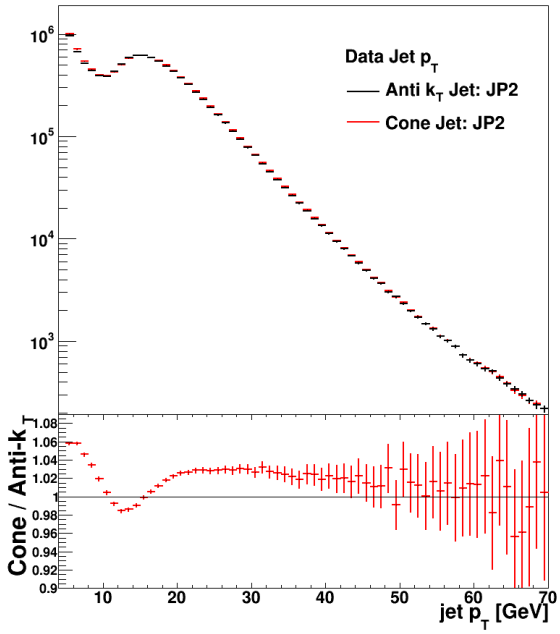

Figure 3.6: **Algorithm Comparison: Jet** p_T - Jet p_T distributions of the anti-k$_T$ (black) and cone (red) algorithms (top plot) and the ratio (bottom plot). The dip at $\sim$ 11 GeV is a result of the JP2 trigger threshold.

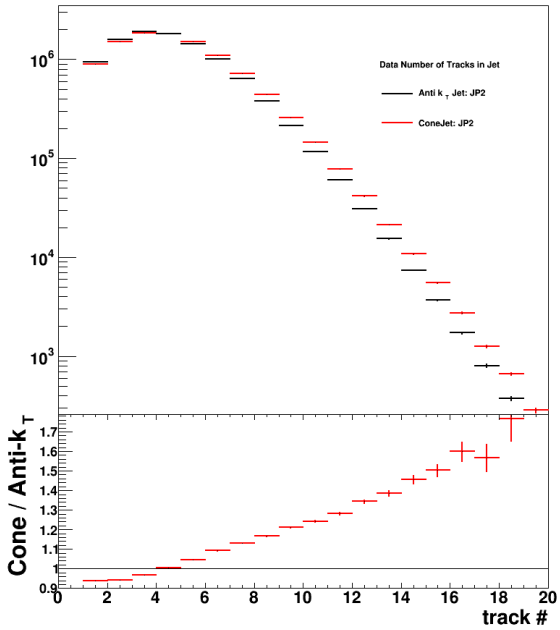

Figure 3.7: **Algorithm Comparison: Number of tracks** - Track number comparison of the Anti-k$_T$ (black) and Cone (red) Algorithms

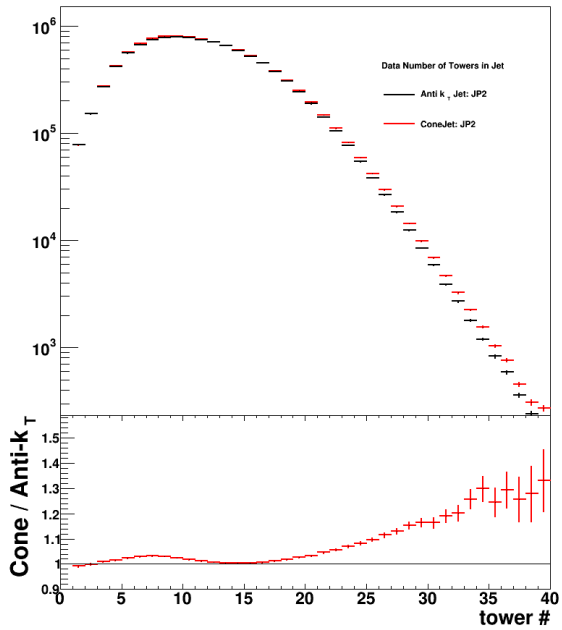

Figure 3.8: **Algorithm Comparison: Number of towers** - Tower number comparison of the Anti-k$_T$ (black) and Cone (red) Algorithms

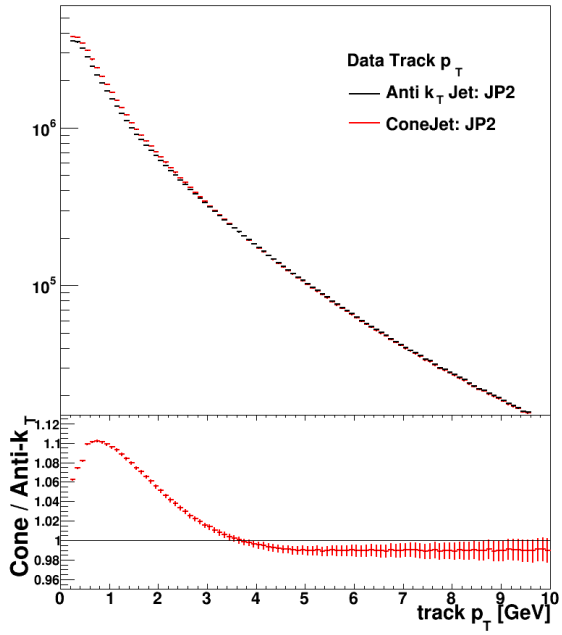

Figure 3.9: **Algorithm Comparison: Track** p_T - Track p$_T$ comparison of the Anti-k$_T$ (black) and Cone (red) Algorithms

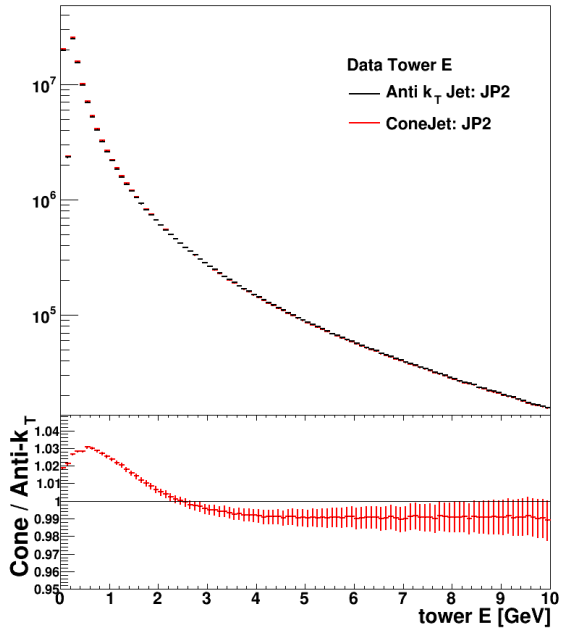

Figure 3.10: **Algorithm Comparison: Tower Energy** - Tower E comparison of the Anti-k$_T$ (black) and Cone (red) Algorithms

energy towers than the anti-k$_T$ algorithm, the enhancement from the low pT tracks is larger than the additional towers. This results in overall net lowering of the neutral energy fraction for the midpoint cone algorithm. The anti-k$_T$ algorithm produces more jets with a large R$_T$ value ($\sim$1) than the mid-point cone algorithm. Another way to look at this distribution, in order for a low p_T anti-k_T jet to satisfy the trigger, the jet must have a fairly large amount neutral energy.

Another fascinating aspect from this comparison are the jet, track, and tower η distributions, which are shown in Figures 3.12 - 3.14 respectively. Overall, the cone algorithm is larger due to the increase in jet, track, tower multiplicities. However, the cone algorithm shows an additional enhancement in the jet η region of ± 0.5 while the track and tower eta distributions are further enlarged at $\eta = \pm 1.0$. As we have established the cone algorithm sweeps up more low p_T tracks and low E towers than the anti-k$_T$ algorithm. These particles are expected to be found at larger η, which explains the track and tower η distributions. These tracks and towers, on the other

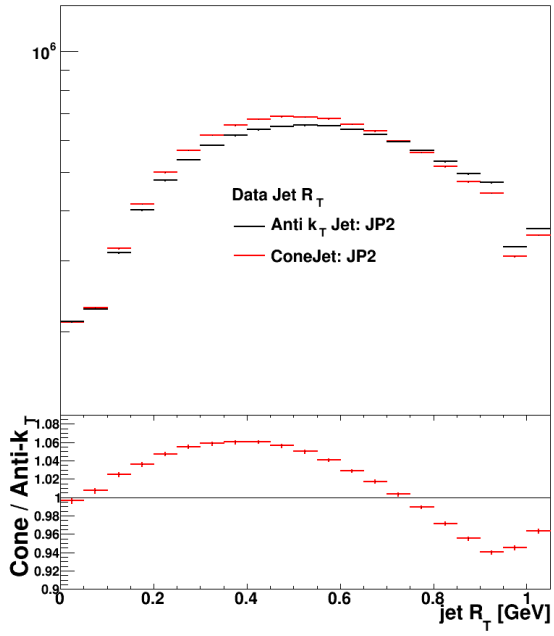

Figure 3.11: **Algorithm Comparison: Jet neutral energy** - Jet R_T comparison of the Anti-k_T (black) and Cone (red) Algorithms

hand, do not greatly alter the η position of the actual jet. Instead the jet location will be largely influenced by the leading particle within the jet.

Figures 3.15 - 3.17 displays the ϕ distribution for the jets, tracks and towers for both algorithms. Again there is an overall increase for the cone algorithm. From these plots, we can observe the jet patch structure in the BEMC and it appears that the cone algorithm has a slight enhancement in the center of the jet patches.

The midpoint cone algorithm tends to collect more tracks and towers at the low momentum and energy regions, which suggests that the mid-point cone algorithm is more susceptible to underlying event and hadronization effects. However, verification of this statement needs to be further explored by examining the two algorithms in the embedded Monte Carlo (MC) sample. The embedding sample consists of real data taken with a random trigger and overlaying MC simulation into it. This procedure effectively mixes the STAR backgrounds and pile-up effects into the PYTHIA [49] model of the hard interactions. The embedding sample is described in detail in

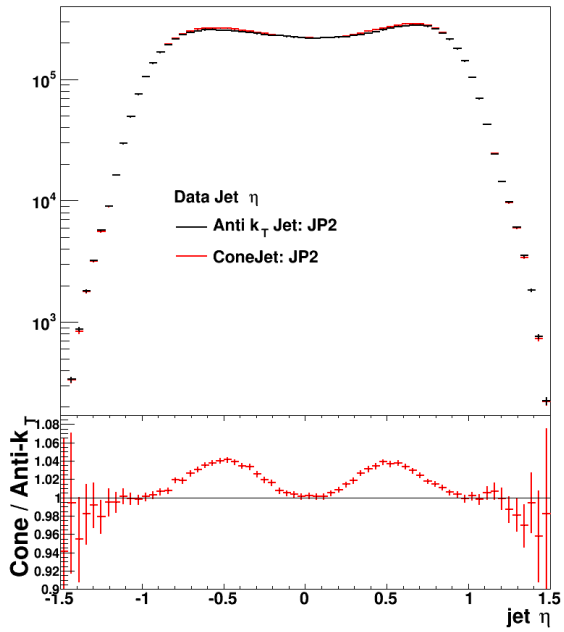

Figure 3.12: **Algorithm Comparison: Jet** η - Jet η comparison of the Anti-k$_T$ (black) and Cone (red) Algorithms

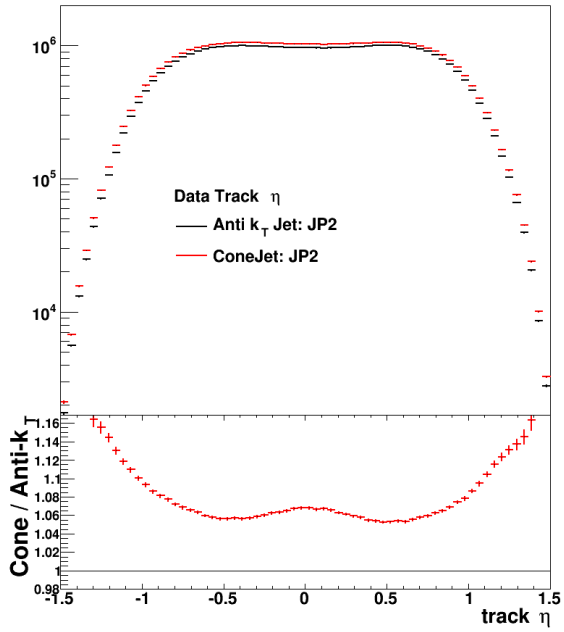

Figure 3.13: **Algorithm Comparison: Track** η - Track η comparison of the Anti-k$_T$ (black) and Cone (red) Algorithms

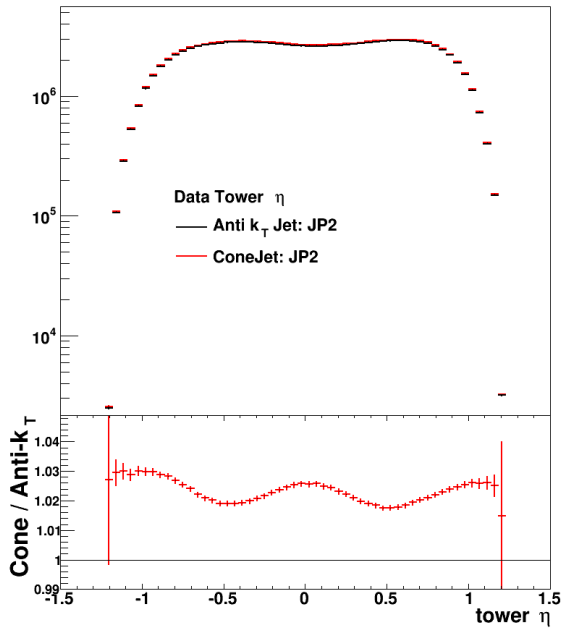

Figure 3.14: **Algorithm Comparison: Tower η** - Tower η comparison of the Anti-k$_T$ (black) and Cone (red) Algorithms

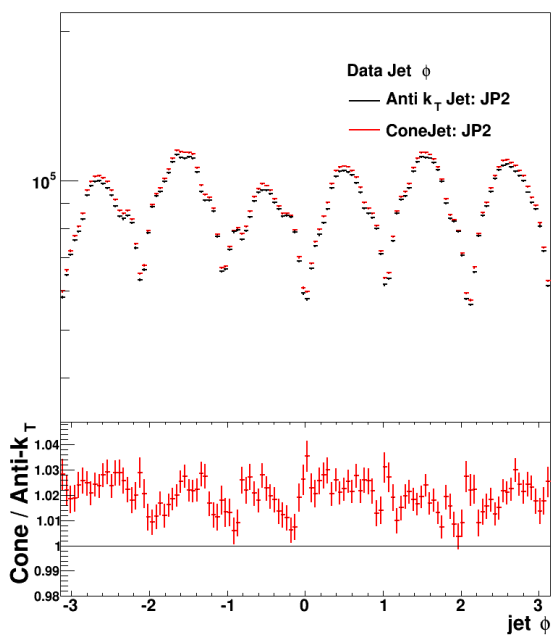

Figure 3.15: **Algorithm Comparison: Jet ϕ** - Jet ϕ comparison of the Anti-k$_T$ (black) and Cone (red) Algorithms

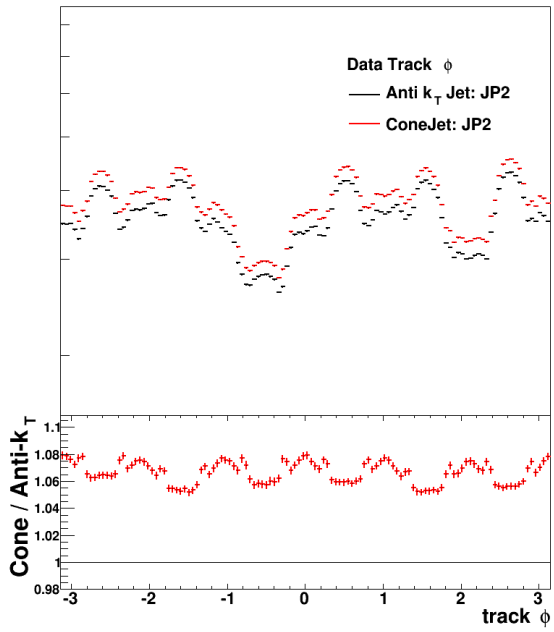

Figure 3.16: **Algorithm Comparison: Track** ϕ - Track ϕ comparison of the Anti-k$_T$ (black) and Cone (red) Algorithms

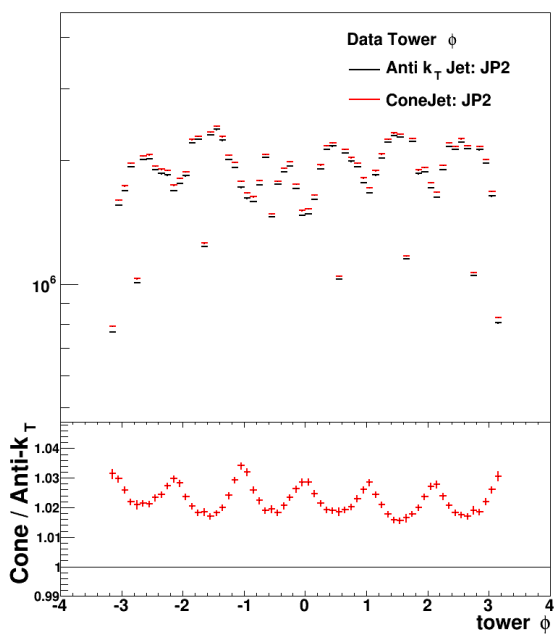

Figure 3.17: **Algorithm Comparison: Tower** ϕ - Tower ϕ comparison of the Anti-k$_T$ (black) and Cone (red) Algorithms

Section 4.4. In addition, it allows for the examination of the two algorithms at the parton-level which doesn't have hadronization and underlying event effects and at the particle-level which does model these non-perturbative QCD contributions.

In order to ensure that the particle-level jet originates from the parton-level jet a matching criteria is implemented. It requires that the jet axes at the parton and particle level be separated by $\Delta R = \sqrt{(\phi_{parton} - \phi_{particle})^2 + (\eta_{parton} - \eta_{particle})^2} < 0.4$ and is illustrated in Fig 3.18. Fig 3.19 examines the ΔR between the matched parton-level and particle-level jets as a function of parton-level and particle-level jet p_T. This demonstrates that the ΔR distribution for the anti-k_T algorithms falls at faster rate as jet p_T increases than the mid-point cone algorithm. This verifies that the pointing vector of jets produced from anti-k_T algorithm are less affected when going from the parton level to the particle-level. In other words, the spatial positioning of anti-k_T jets are affected to a lesser degree by the hadronization (HAD) and underlying event (UE) contributions than the mid-point cone algorithm.

The particle distribution within jets also provides insight to the effect hadronization and underlying event has on the jet structure. This distribution is often referred to as the "fluffy-ness" of the jet. If the majority of the particles lie close to the jet-axis then the jet is highly collimated and not fluffy. Jets containing particles over a broad distribution, specifically particles that lie close to the cone edge, are susceptible to non pQCD effects. The low p_T jets have a much larger ΔR distribution due to the fact they have lower multiplicities and are considered fluffy. Any loss or gain of a particle or parton due to the underlying event and hadronization effects will then have a greater influence on the pointing direction of the jet.

To determine the dispersion of particles within a jet, fractional portions of a jet are studied. Fig 3.20 illustrates a fraction of a jet at a particular radius. This radius varies from small ($r = 0.05$) to large ($r = 1.0$) values in this analysis. Therefore, as the fractional-jet radius, r, approaches the original jet-radius, R, the fraction (frac)

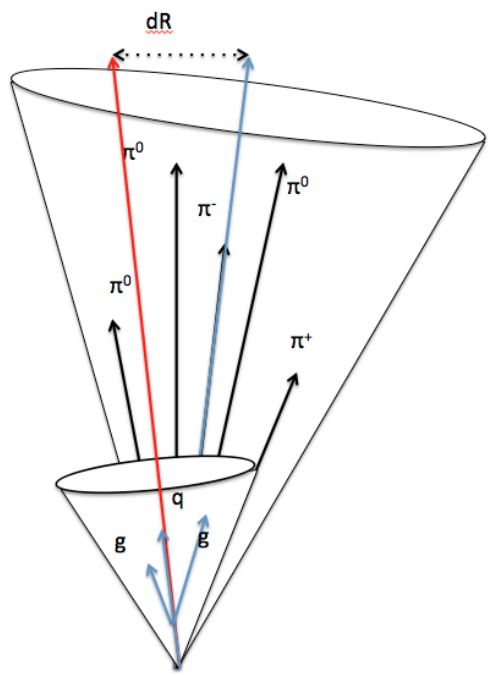

Figure 3.18: **Particle and Parton Level Jet Matching** - An illustration of the matching criteria between parton-level and particle-level jets. Both use a radius of 0.6.

should approach 1. The definition of this fraction is defined as:

$$F = \frac{\left(\sum_i p_{T_i}\right)_{r \leq R}}{\left(\sum_i p_{T_i}\right)_{r=R}} \tag{3.6}$$

where the denominator is just the original jet p_T. This fraction as a function of the radius, r, is plotted in Fig 3.21 for various jet p_T regions.

Jets in the (5 GeV $\leq p_T \leq$ 10 GeV) region (top left plot in Fig 3.21) tend to have a larger dispersion of particles within the jet than higher p_T jets. As expected, jets become more collimated and less fluffy as they increase in p_T. It is clear from this figure that the anti-k$_T$ algorithm reaches $F = 1$ earlier than the mid-point cone algorithm. This means the anti-k$_T$ algorithm produces less fluffy jets and is less susceptible to the hadronization contributions.

There are many benefits of using the anti-k$_T$ jet algorithm for jet reconstruction

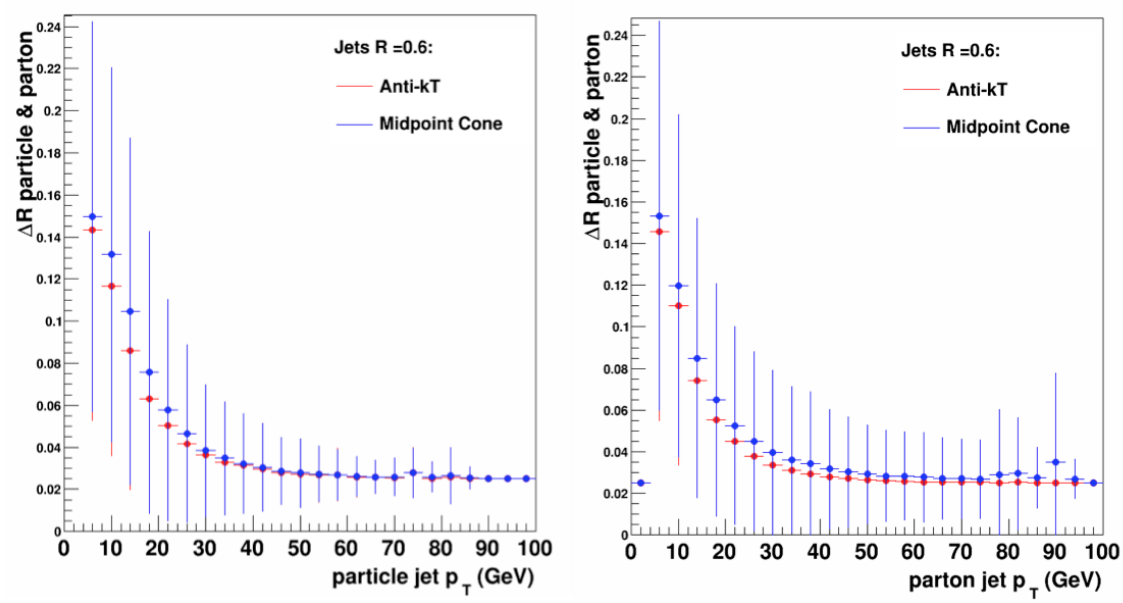

Figure 3.19: **ΔR vs. jet** p_T - The Monte Carlo distribution of ΔR as function of particle jet pT (left) and parton jet pT (right). Note: There is a change in the color scheme. The red points now represents the anti-k_T algorithm and the blue point represents the mid-point cone algorithm. Both algorithms use a radius of 0.6. The errors shown are not the statistical errors, but are the RMS of the distribution.

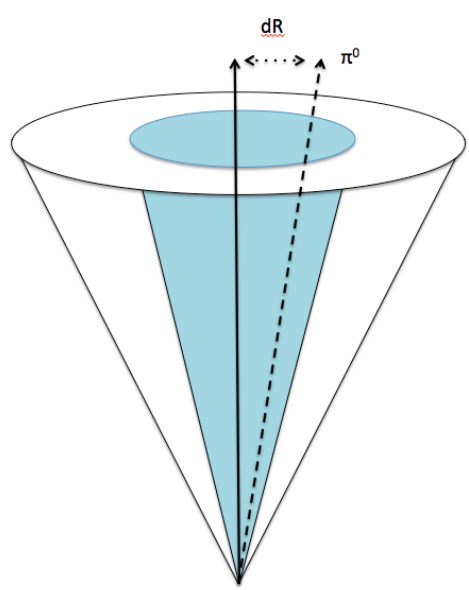

Figure 3.20: **Fractional Jets** - A diagram looking at a fraction of the momenta of particles within a specified radius. The blue region is the collection of particles within that radius.

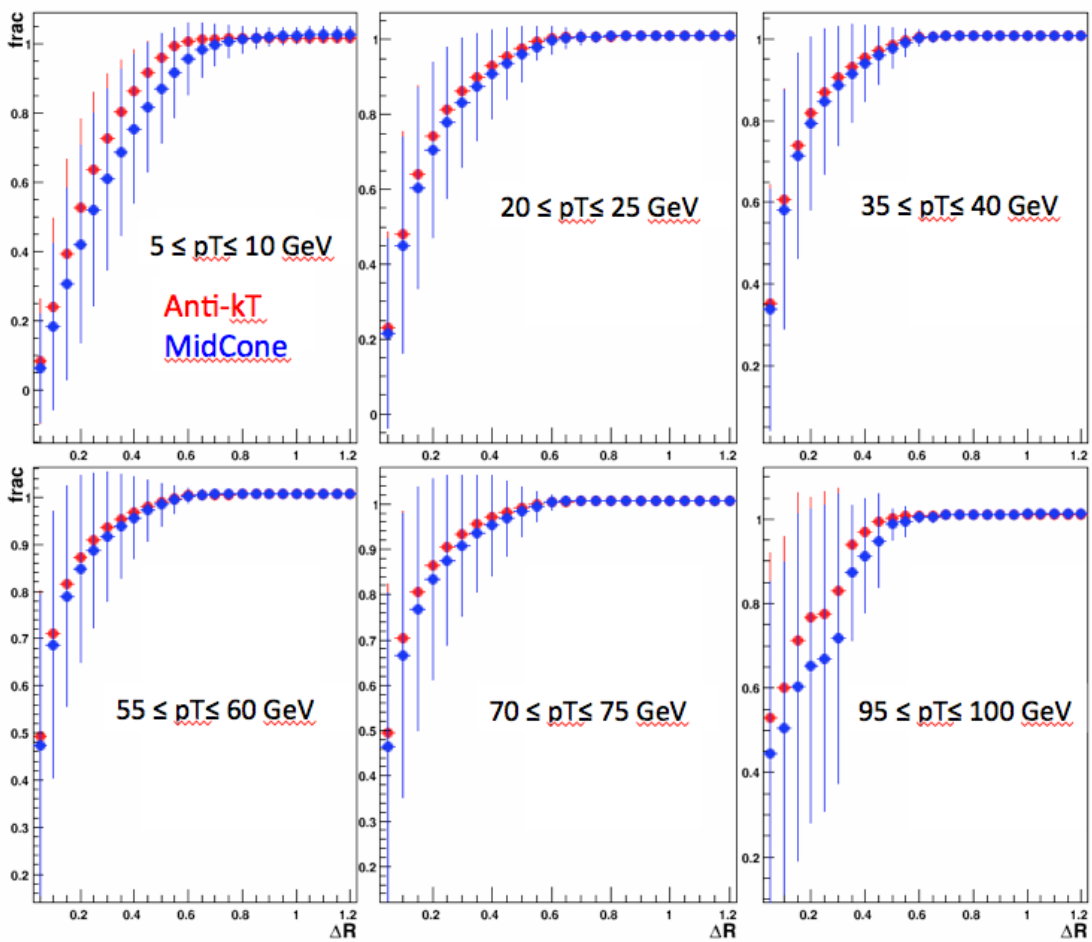

Figure 3.21: **Fractional jet Vs. ΔR** - The MC distribution of the fractional jet (described in text) as function of ΔR for the anti-k$_T$ (red) and mid-point cone (blue) algorithms. The top left plot examines the distribution at low jet particle jet p_T. The particle jet p_T increases in plots to the right and below.

at STAR. It has stronger theoretical support and is less susceptible to pile-up, the underlying event, and hadronization effects. This reduces the size and error associated with the required corrections of these effects. Similar conclusions were reached in the Run 9 200 GeV inclusive jet analysis [50]. Therefore, the dijet cross section analysis will use the anti-k$_T$ algorithm with a radius of 0.6 for jet reconstruction.

Chapter 4 Dijets

4.1 Event Selection

In 2009 RHIC operated, for the first time, at its highest reachable center of mass energy for proton-proton collisions at 500 GeV. The run began on January 16, 2009 and ended April 17, 2009 during which STAR acquired 694 physics runs. A typical run at STAR lasts on the order of $\sim 1-2$ hours during the 500 GeV data-taking. However, many runs were significantly shorter due to detector, trigger, and accelerator issues. In order to be confident with the collected data, a thorough quality analysis was performed, which significantly reduced the number of usable runs.

4.1.1 Event-by-Event Quality Anaylsis

The first method used to assure the quality of a run was an event-by-event quality analysis. In this process the average values of important detector quantities were examined for each trigger. The triggers are defined in Section 2.3. If one of these quantities for a run largely deviated from the majority of the other runs, it became a suspicious run and was further investigated. An examination of the shift log, trigger plots, and the online detector response plots of the suspected run was then performed. This indentified many potential problems during data acquisition. As an example, Fig 4.1 is a plot of the average track p_T in an event verses the run index. Runs corresponding to the run index 218 - 226 diverge considerably from the majority of the other runs, alerting us to a trigger problem during the data taking. These runs were then excluded from the analysis.

Once the obvious outlier investigation was completed, we plotted the distributions of the observable quantities and applied a Gaussian fit (shown in Fig 4.2). Any run with deviations greater than $|3\sigma|$ from the gaussian peak became suspect and further

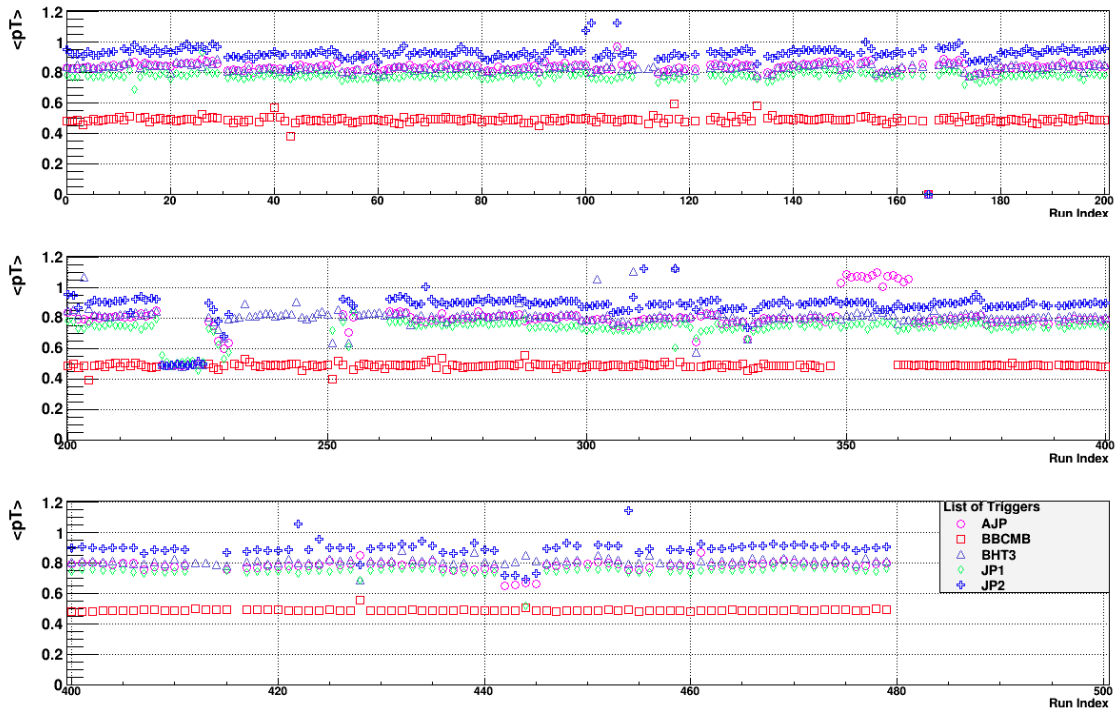

Figure 4.1: **Average track p_T vs Run Index** - The average p_T for all events in each run number before applying any selection criteria

examined. Then using the same analysis tools mentioned earlier, a decision was made to include or exclude the run.

This entire process was repeated for each trigger for many different observables such as track p_T, tower E_T, track and tower multiplicity, track and tower η, track and tower ϕ, etc. Fig. 4.3 demonstrates the final results of this quality analysis after the removal of problematic runs. The average track p_T remains fairly consistent for each run. This ensures that the detectors are responding as expected and all observables are consistent throughout a run.

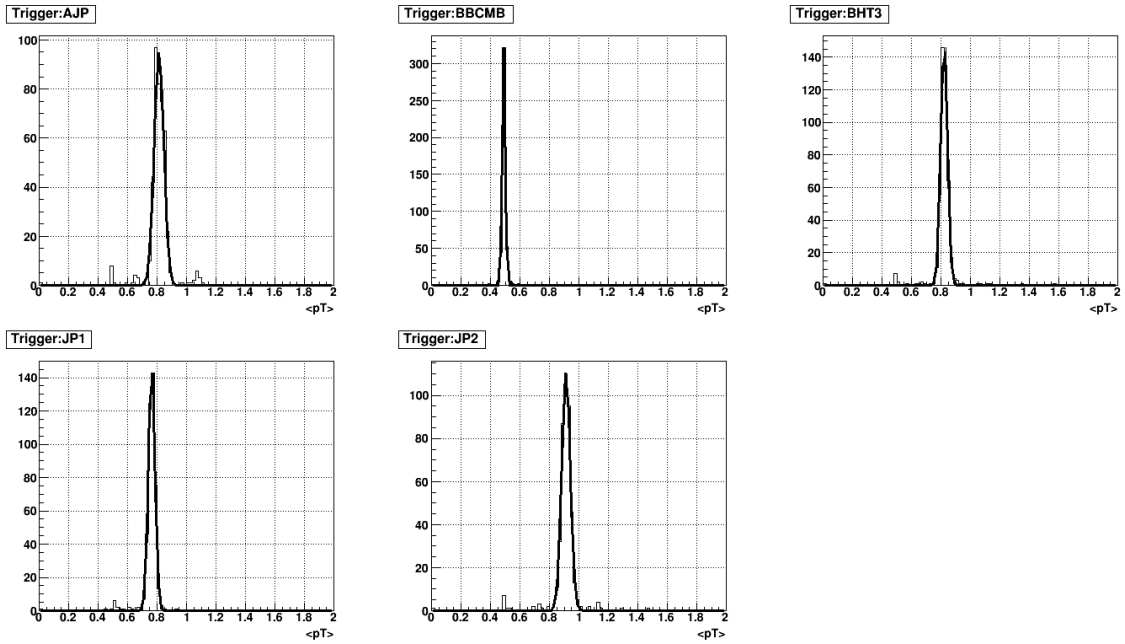

Figure 4.2: **Gaussian** $< p_T >$ - Distributions of the average track p_T of all runs. This is done for each 2009 trigger.

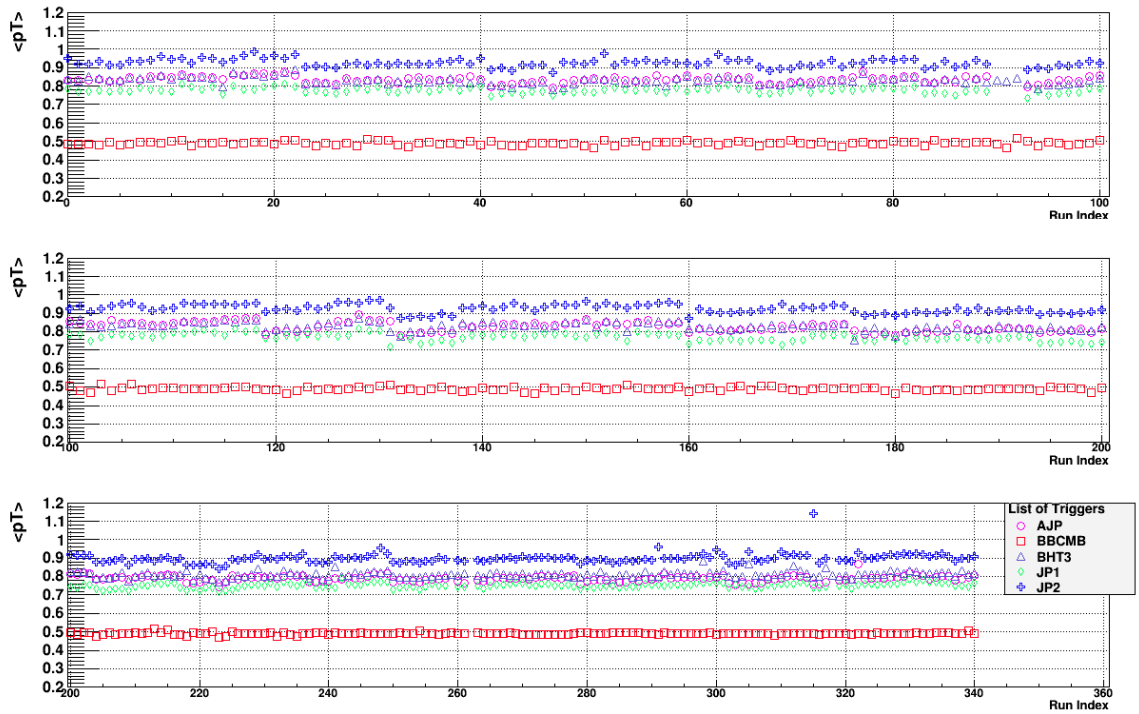

Figure 4.3: **Average track $\mathbf{p}_T$ vs Run Index** - The average p_T for all events in each run number after applying the selection criteria

4.2 Jet Quality Analysis

In the 2009 pp 500 GeV data analysis, two jet algorithms were examined: the mid-point cone jet algorithm and the anti-k_T jet algorithm. Regardless of the algorithm used, however, a list of particles is required and one needs to safeguard that only legitimate particles produced from the collision are used. Therefore, the conditions in Table 4.1 are required for all tracks and towers to be included in a jet-finding algorithm.

In order to ensure the particles are of interest (originating from the hard collision), it is required that the number of hits on the TPC's padrows are greater than 12 hits. Also the ratio of the number of hits and the number of possible hits is above fifty-one percent. The total number of possible hits for a track is, depending on the rapidity of the track, the number of padrows the track could have possibly crossed. For a mid rapidity tracks the total number of possible hits is 44, which is just the total number of padrows in the inner and outer TPC sectors. In addition, a distance of closest approach (DCA) cut, described in Table 4.1, and a $\chi^2 < 4$ cut are applied to remove the pile-up background tracks. The DCA is a distance between the primary vertex and the closest hit on the track. The DCA_{xy} is the x and y component of the DCA vector. In each event, the towers used are the ones with ADC values greater than three times the root mean square of the pedestal noise distributions from the pedestal mean. In order to prevent double counting of the charged particles, once in the TPC and once in the BEMC, if the track points to a BEMC tower, 100% of the track's energy is subtracted from the tower energy. If the track's energy is greater than the tower's energy , leading to a negative result, then the tower energy is set to zero.

Once we determined the run list from the event-by-event quality analysis, we proceeded to perform a quality analysis at the jet level. This jet quality analysis

Track Analysis Parameters:		
# Track Hits > 12		
# Track Hits / # Possible Hits > 0.51		
Track $p_T \geq 200$ MeV		
$-2.5 \leq$ Track $\eta \leq 2.5$		
Last Point on Track > 125 cm		
$\lvert DCA \rvert \leq 3.0$ cm		
	≤ 2.0 cm	if $p_T^{track} < 0.5$ GeV
DCA_{xy}	$\leq 3.0 - 2.0Ep_T^{track}$ cm	if $0.5 \leq p_T^{track} < 1.0$ GeV
	≤ 1.0 cm	if $1.0 \leq p_T^{track}$ GeV
Tower Analysis Parameters:		
Tower Status = 1		
ADC - Pedestal > 4.0 & ADC-pedestal > 3 E RMS		
Tower $E_T \geq 200$ MeV		
Tower Energy Correction for Tracks:		
100% Subtraction Scheme		

Table 4.1: Track and Tower Selection in Jet Reconstruction at the detector-level

used the standard midpoint cone algorithm with a cone radius of 0.7. The analysis examined the average jet, track and tower quantities for various triggers. Fig 4.4 - Fig 4.6 show some of the results of the jet-level quality analysis.

At this point in the quality selection process not many new outlier runs were observed. The majority of the runs removed are due to zero jets being found in the run, which you can see for a few runs in the indicated plots. After the full selection process, the event and jet quality analysis, 326 runs are used for the dijet cross-section analysis.

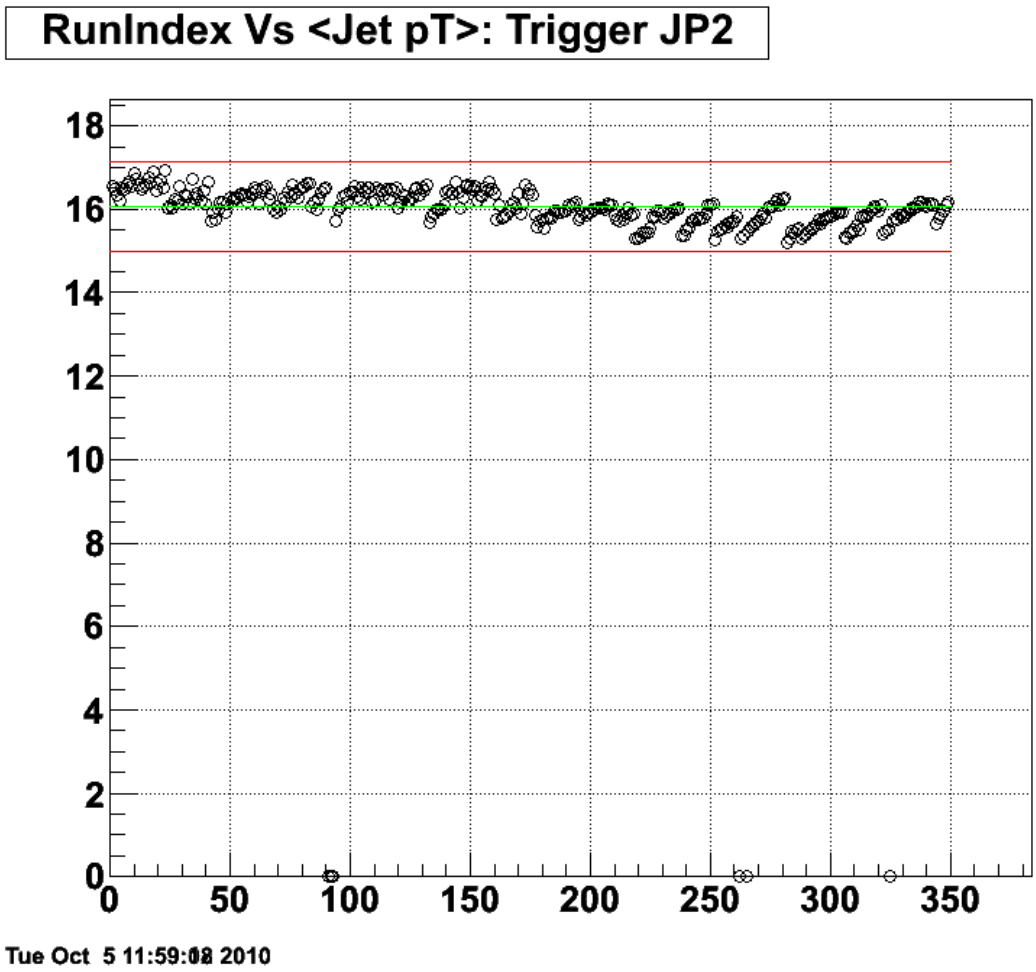

Figure 4.4: **Average Jet p_T vs Run Index** - The average jet p_T for all events in each run index. The green line is the average of all runs and the red lines are $|3\sigma|$ away from the mean.

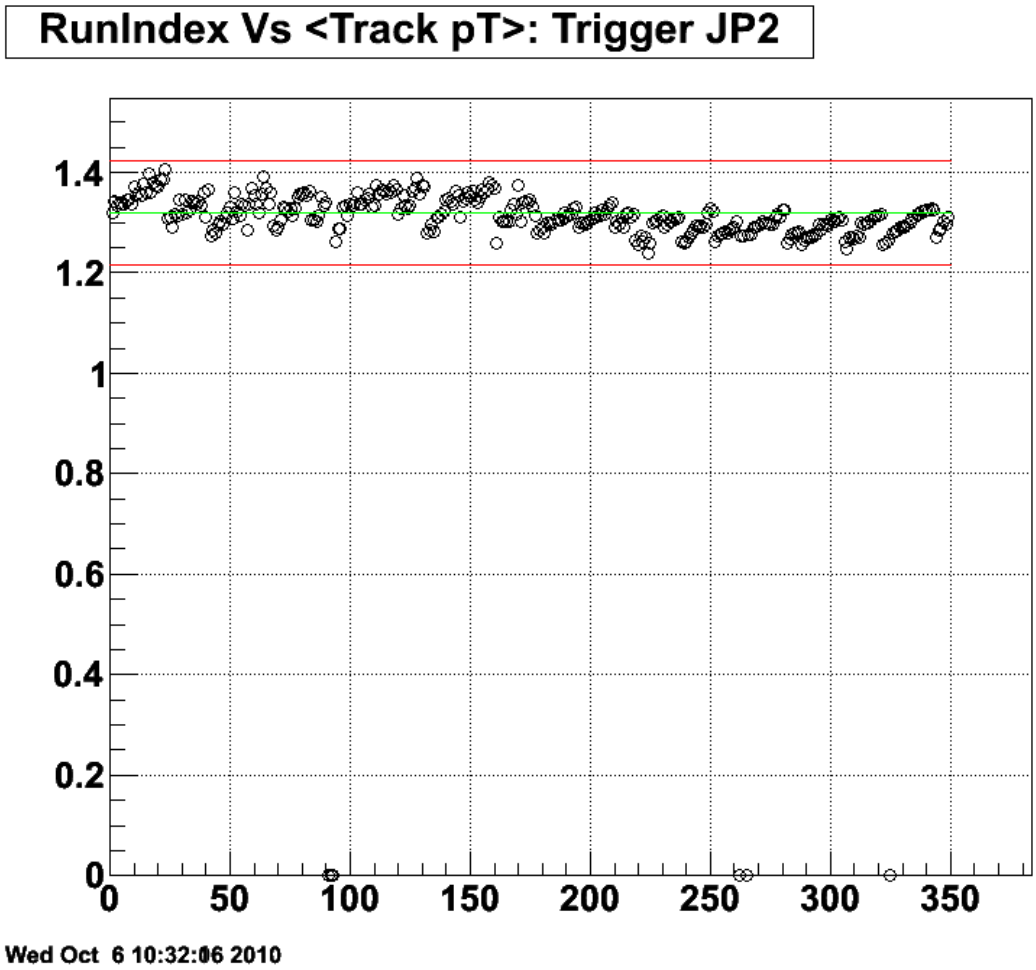

Figure 4.5: **Average Track p_T within Jet vs Run Index** - Average p_T of tracks associated with a jet verses run index. The green line is the average of all runs and the red lines are $|3\sigma|$ away from the mean.

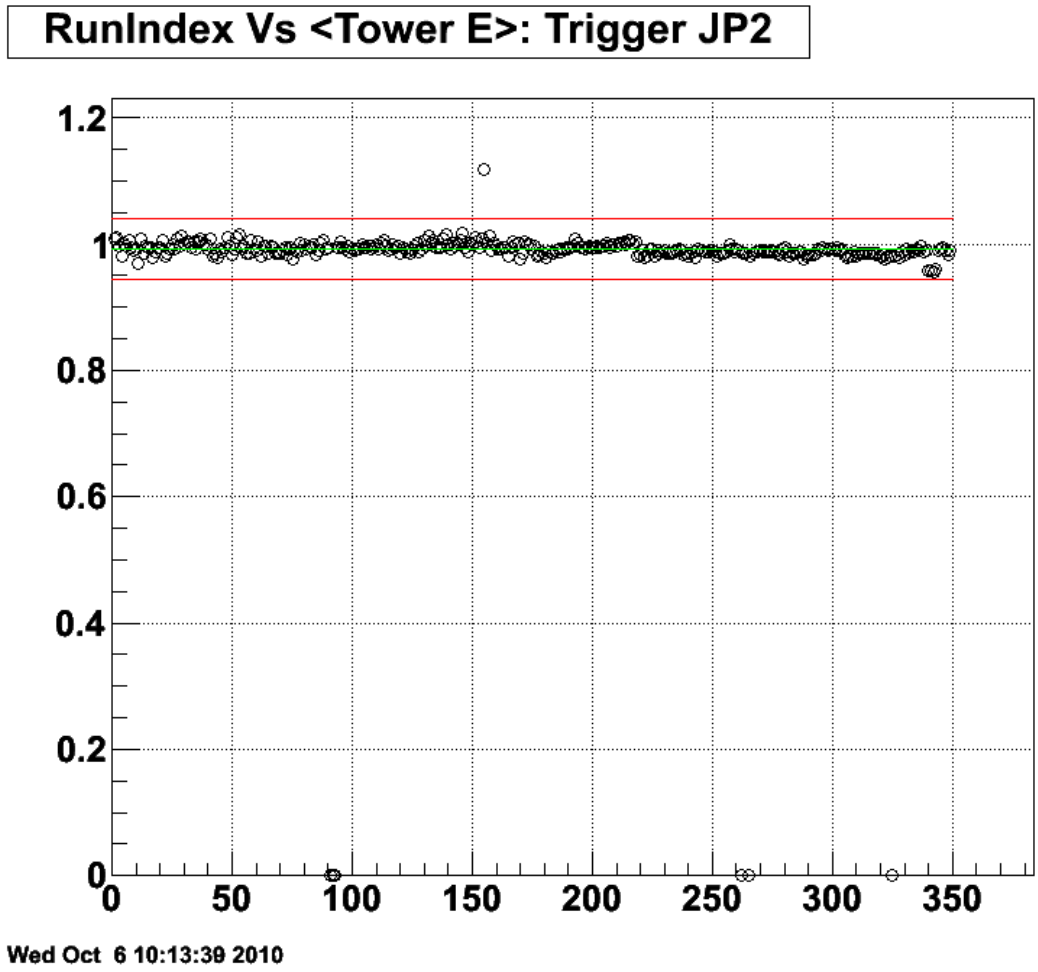

Figure 4.6: **Average Tower Energy within Jet vs Run Index** - Average energy of towers associated with a jet E_T verses run index. The green line is the average of all runs and the red lines are $|3\sigma|$ away from the mean.

4.3 Dijet Definition

Once all the reconstructed jets were obtained for every event which passed the quality analysis, selection of the less frequent dijet events can proceed. Dijets are defined as the two leading-p_T jets of an event. However, there is some ambiguity behind this definition, which must be avoided. The uncertainty in the definition lies with selection criteria and its order of operation. Consider an event with three jets A, B, and C in descending order of jet p_T before any selection is applied. Assume that jet B doesn't meet one of the jet selection requirement, for example the rapidity cut. If the selection criteria is applied before the dijet definition, jets A and C will form a dijet event. However, if the dijet event is defined first, jets A and B are the dijet candidate and since jet B is rejected, no dijet event exists. Therefore, an explicit dijet definition requires a specific order of operations of the selection criteria. The following sections is the order of operations for this dijet analysis.

4.3.1 Two Leading p_T Jets

The first criteria in defining a dijet is requiring the event have two or more jets. There is obviously no possible way to have a dijet if there is only one jet in the event.

$$\text{Number of Jets} \geq 2.0 \tag{4.1}$$

Immediately following this requirement only events that fired one of the selected triggers (see Section 2.3) are examined. This is only required for dijets in the data and at the detector-level in the embedding sample. A trigger requirement doesn't make sense for the particle and parton-level since the detector does not exist at these levels.

The list of jets are then sorted from the highest p_T jet to the lowest p_T jet. Then the two jets with the highest p_T, jet$_1$ and jet$_2$, are selected out. Since the numbers 1 and 2 are typically reserved for the two incoming partons, the numbers 3 and 4 are

used for the outgoing jets. The jet with the larger rapidity is defined as jet 3 and the jet with the smaller rapidity is defined as jet 4.

if($y_1 \geq y_2$)	$\text{jet}_3 = \text{jet}_1$ $\text{jet}_4 = \text{jet}_2$
if($y_1 < y_2$)	$\text{jet}_3 = \text{jet}_2$ $\text{jet}_4 = \text{jet}_1$

Table 4.2: Definition of jet_3 and jet_4 based upon the rapidity, y, of the two leading p_T jets.

4.3.2 p_T Thresholds

An asymmetric p_T cut is then applied. The leading jet with the highest jet p_T must be larger than 13 GeV and the lower p_T jet should be larger than 10 GeV.

$$\text{high jet } p_T > 13.0 \text{ GeV} \tag{4.2}$$

$$\text{low jet } p_T > 10.0 \text{ GeV} \tag{4.3}$$

This requirement was raised for the 2009 500 GeV data compared to the 2009 200 GeV data, which typically used 10 and 7 GeV thresholds. The increase was implemented due to the increase in the trigger thresholds in the 500 GeV data. The main reason behind implementing an asymmetric p_T cut is NLO pQCD calculations will under predict the cross section if the cut were symmetric. There are three contributions to every NLO cross section calculations, a $LO(p_{T3}, p_{T4})$, a $NLO_{virtual}(p_{T3}, p_{T4})$, and a $NLO_{real}(p_{T3}, p_{T4})$. The $NLO_{real}(p_{T3}, p_{T4})$ is calculated using only events where the $p_{T3} < p_{T4}$ and so the jet p_T asymmetric cut is applied to ensure contributions from this positive real component.

4.3.3 BEMC Acceptance and Jet Rapidity y

The reconstructed jets need to lie fully within the acceptance of the detector. Since jets are observables that cover a significant area in $\eta - \phi$ space, we must avoid jets

that are reconstructed at the edge of the BEMC acceptance. The detector η is given with respect to the center of the detector ($x = y = z = 0$). The detector η of a jet is the position of the BEMC that the four-momenta of the jet crosses and we require the following criteria

$$-0.7 < \text{detector } \eta < 0.7 \tag{4.4}$$

to ensure the majority of the jet area lies fully within the detector and reduces the corrections from the detector to particle level. The ultimate goal is to correct back to the particle level and so in order specify a definite jet rapidity, y, range the following jet y cut is applied.

$$-0.8 \leq \text{jet } y \leq 0.8 \tag{4.5}$$

This applies a clean cut at a specific rapidity, which is defined with respect to the jet vertex position. The relation between the detector η and the jet rapidity is demonstrated in Fig 4.7, where the detector η cut has been applied but not the jet y cut.

4.3.4 Neutral Energy Ratio and Background

There are scenarios where the highly energetic proton beams interact with other materials, such as the beam-pipe, the magnet, etc. These collisions result in what is referred to as the beam-background. Of course, the particles produced from these collisions are not of interest, but are seen in the detectors. Fortunately, the charge tracks do not point back to the vertex and are excluded from the event. However, it is not possible to distinguish tower responses that come from the vertex and those that arrive from beam backgrounds. Therefore, a large deposit of neutral energy from the beam background may be detected by the calorimeters, leading to false triggers, creating false jets, and contributing neutral energy to the existing jets . In order to limit our contamination from the beam background, a neutral energy fraction (R_T)

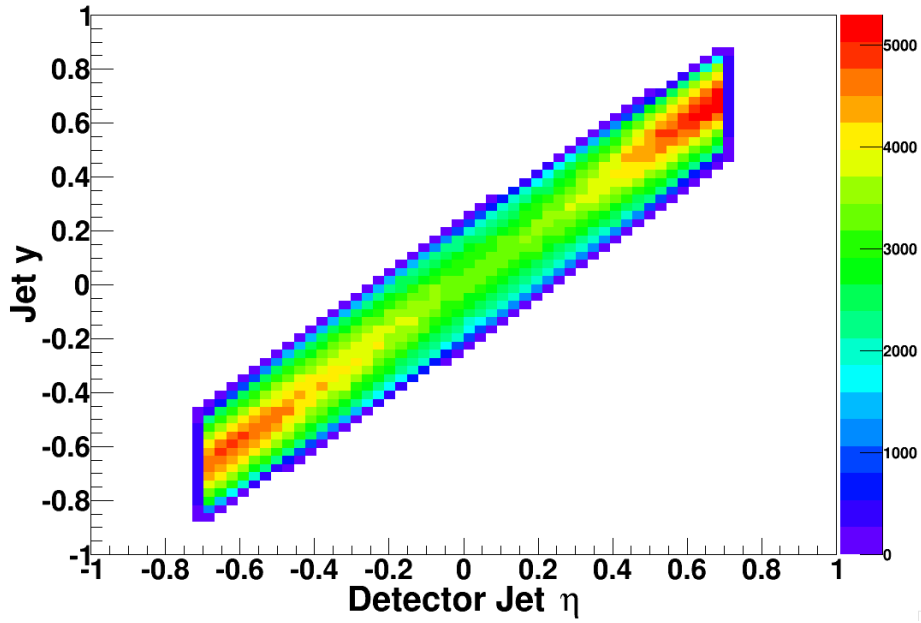

Figure 4.7: **Detector η Vs Jet y** - The correlation between the detector η and the jet y. The detector η cut has been applied but not the jet y cut. The majority of the distribution lies within the jet y range of -0.8 to +0.8.

cut on the produced jets is required:

$$R_T = \frac{E_T^{neutral}}{E_T^{jet}} < 0.95. \tag{4.6}$$

The neutral energy fraction is the ratio of neutral transverse energy of the jet to the transverse energy of the jet. This ensures that we never have any jets with only neutral energy and that the jets contain a significant amount of charged tracks within the jets. The tendency is for low p_T jets to have higher R_T values due to the trigger bias .

4.3.5 Vertex Requirement

A vertex requirement of

$$|\text{vertex z}| \leq 50 \text{ cm} \tag{4.7}$$

is applied to ensure collisions occur close to the center of the detector. A vertex reconstructed at the edges of the detector are likely from background collisions. In

addition the outgoing particles from such a collision will tend to fall outside the acceptance of the STAR detectors.

4.3.6 Back-to-Back Jets

The two outgoing jets of the dijet are required to be "back-to-back" jets by satisfying the following cut:

$$|\Delta\phi| \geq 2.0. \tag{4.8}$$

This cut ensures that the two leading jets of interest originate from the initial outgoing hard partons in the hard collision.

4.3.7 Triggered Jets

Is it impossible to store the output of every collision, there is simply not enough computer disk space, and many events are not sensitive to the desired observable. Therefore, events that passed a particular trigger are selected for analysis. A triggered jet is the jet that caused the trigger to occur. In the dijet measurement, at least one jet of the dijet pair is required to be a triggered jet. This condition is established by matching the $\eta - \phi$ of the jet to the $\eta - \phi$ of the fired jet patch (JP). The following matching requirement is tested for each jet in the dijet pair:

$$|\phi_{jet} - \phi_{JP}| \leq 0.6 \tag{4.9}$$

$$|\eta_{jet} - \eta_{JP}| \leq 0.6. \tag{4.10}$$

If neither jet of the dijet pair meets this condition then the event is removed.

4.3.8 Phase-Space

The comparison of data and theory predictions are only valid if they both have the same phase space. This section summarizes the selection criteria in the previous

sections, which establishes the phase space used. The phase space for the dijet measurement is indicated in Table 4.3.

high jet $p_T > 13.0$ GeV
low jet $p_T > 10.0$ GeV
-0.8 $\leq y \leq$ 0.8
$\lvert\Delta\phi\rvert \leq 2.0$

Table 4.3: Phase space of the dijet measurement

4.3.9 Invariant Mass

The invariant mass of a dijet event can now be calculated and is defined as

$$M = \sqrt{m_3^2 + m_4^2 + 2\sqrt{m_3^2 + p_{T3}^2}\sqrt{m_4^2 + p_{T4}^2}\cosh(\eta_3 - \eta_4) - 2p_{T3}p_{T4}\cos(\phi_3 - \phi_4)} \tag{4.11}$$

and if the jet mass is ignored then the expression becomes

$$M = \sqrt{2p_{T3}p_{T4}(\cosh(\eta_3 - \eta_4) - \cos(\phi_3 - \phi_4))}. \tag{4.12}$$

4.4 Monte Carlo Embedded Simulation

The Monte Carlo (MC) simulated events are generated to unfold the dijet cross section from the detector-level to the particle level. In addition, it is used to estimate the effect of hadronization and the underlying event on the jet energy scale. This section describes the filtered MC embedding event production request and its development. In addition it discusses the jet reconstruction in this simulation.

4.4.1 Filters and their performance

There are two filters implemented in this setup:

1. a dijet filter executed at the particle level

2. a trigger filter invoked before the computationally expensive track reconstruction

Ideally a filter will only throw away events that would not have passed the full detector level trigger or dijet reconstruction. In reality the filters applied at the particle level and at the detector level may bias the reconstructed sample. A successful filter reduces the computation time, provides a sample enhanced with the desired events, and limits the biases to an acceptable level.

The characteristics of the trigger and dijet filters were optimized through a series of embedding simulation tests. In these test the events that failed the filter were not removed, but flagged as failed events. Then the events were evaluated for successful dijet and trigger reconstruction at the detector level.

4.4.2 Filter Descriptions

StMCFilter (StDijetFilter)

The first filter applied to the sample is referred to as the dijet filter. The selection of a dijet event on the particle level is defined as:

- Cone radius R = 0.7
- Particle is a seed if it has at least 0.5 GeV
- Using Mid-Point Cone algorithm
- Split/Merge is used and jets are merged if overlap is greater than 50%
- Particle $|\eta| < 3.5$
- Jet $|\eta| < 1.3$
- Dijet $p_T\ low > 10\ GeV$
- Dijet $p_T\ high > 13\ GeV$

- $|\Delta\phi| > 2$
- Min(jet p_T) $> 4\ GeV$
- $\Delta\eta < 2.6$

This filter is an inclusive filter. This means that if 100 events are requested then it will throw as many events as needed to produce 100 events that pass the listed dijet filter requirements.

StFilterMaker (StTriggerFilterMaker)

The events are then passed to the trigger filter, which accepts events that would have fired the JP1, AJP or BHT3 triggers. This filter is performed on the GEANT (the detector simulator) level [51], but before computationally expensive tracking is performed.

4.5 Environment

This section briefly describes how the embedding sample was created. Many of the the computational details are quite technical and are listed in Appendix 7.1. In short, the code embeds the simulated response from the MC into a randomly triggered data sample. The zerobias trigger randomly samples events throughout the run, which is then use to properly estimate the backgrounds observed the STAR detector. Many of these backgrounds are not capable of being simulated. Therefore, an embedded MC sample will mimic the data to a higher degree than with just only the MC simulation.

4.6 Bias Tests

It is important to note that during the bias tests, none of the filters were actually implemented. Instead, the outcome of each event was recorded (i.e. whether the event passed or failed one of the filters) and was used to determine the bias of each

filter. If the filter bias was $<< 10^{-3}$, which is the precision on the relative cross section values, then it is safe to implement the filter at that particular partonic p_T bin without biasing the results. The first bias test, Table 4.4, used an asymmetric p_T threshold of 7 and 10 GeV, which is the same criteria in the pp 200 GeV analysis. It was later indicated that the asymmetric p_T thresholds should be increased to 10 and 13 GeV for the pp500 data. This is due to the increased trigger thresholds in pp 500 GeV data.

The first column in Table 4.4 refers to the partonic p_T range of the thrown events. The second column, "StMCFilter acceptance", is the ratio of the number of events that pass the particle level dijet filter and the total number of events thrown. The "Total Filter acceptance" is the ratio of events that passed both filters and the total number of events thrown. The "Filter bias" column is calculated by dividing the number of events that failed the dijet filter and yet still passed the trigger filter by the total number of events thrown. The "Total Expected Events" column is simply the values in the "Events for 1 pb^{-1}" column multiplied by the Total filter acceptance column.

Since the first bias tests were done at a low threshold values, the test was repeated with the desired threshold values of 10 and 13 GeV as shown in Table 4.5. In order to save time the bias tests were rerun over the partonic p_T bins with the highest bias. The test showed that increasing the thresholds tends to reduce the bias. This bias study determined which filters will be applied to each partonic p_T bin. Partonic p_T bins 4-11 GeV have both filters applied (Full), partonic p_T bins 11-25 GeV only has the trigger filter applied (Trigger), and partonic p_T bins 25-Infinity GeV receives no filter (None).

In order to conduct the timing tests needed for the embedding request, the filters were then turned on. The results of the timing tests are shown in Table 4.6 and Table 4.7. The "Events Thrown" column indicates the number of events needed to

p_T Bin (GeV)	StMCFilter Acceptance	Total Filter Acceptance	Filter Bias	Events for 1 pb^{-1}	Total Expected Events
3-4	6.96e-03	2.00e-05	0.00	5.27e+09	1.05e+05
4-5	1.69e-02	1.40e-04	0.00	1.48e+09	2.07e+05
5-7	4.70e-02	4.44e-04	0.00	7.49e+08	3.32e+05
7-9	1.26e-01	4.14e-03	2.00e-05	1.55e+08	6.42e+05
9-11	3.10e-01	2.08e-02	9.76e-05	4.44e+07	9.42e+05
11-15	3.68e-01	5.99e-02	3.06e-04	2.21e+07	1.32e+06
15-25	4.96e-01	1.40e-01	1.34e-03	5.72e+06	7.99e+05
25-35	6.53e-01	4.84e-01	2.28e-03	3.42e+05	1.66e+05
35-45	7.54e-01	6.57e-01	1.27e-03	4.32e+04	2.84e+04
45-Infin	9.08e-01	8.11e-01	9.23e-04	1.04e+04	8.43e+03

Table 4.4: Results of a Simulation Only Filter Bias Test with an asymmetric pT cut at the pythia level of 7 and 10 GeV. These values are below our nominal asymmetric pT cut need for 500 GeV.

p_T Bin (GeV)	StMCFilter Acceptance	Total Filter Acceptance	Filter Bias	Events for 1 pb^{-1}	Total Expected Events
25-35	5.95e-01	4.62e-01	2.15e-03	3.42e+05	1.58e+05

Table 4.5: Results of an Embedded Filter Bias Test with an asymmetric pT cut of 10 and 13 GeV

have 11,701 dijet filter accepted events. The "CPU Time" is the amount of time a single CPU needs to process the instructions of a computer program. The "Real Time" is the time taken from the start of the filter test code until the end as measured by an ordinary clock. The elapsed real time is always same or more than the CPU time. If a computer program used only one CPU for processing then the real time and CPU time would be the same.

The final embedding request was for a total of 5.42 M events of which 2.0 M will pass the dijet pythia filter and 1.04 M will pass both the pythia and trigger filters. The total time is 1.09×10^8 seconds (3.5 CPU years) and will leave a footprint of 451 GB. However, after re-examination of the low and high pT bins adjustment to the requested number of events in Table 4.8 were made. Calculations of the cross-sections for the highest p_T bins, demonstrated an over estimate in the number of

p_T Bin (GeV)	Events Thrown (s)	Average Time per Event	Trigger Accepted	Fzd File Size (GB)	MuDst + Pythia File Size (GB)
3-4	1.32e+07	45.50	67	8.30	0.179
4-5	4.24e+06	22.80	112	8.26	0.198
5-7	1.52e+06	18.25	291	8.18	0.281
7-9	4.21e+05	10.83	709	8.04	0.470
9-11	1.34e+05	8.92	1311	7.81	0.715
11-15	1.17e+04	8.63	1157	7.49	0.638
15-25	1.17e+04	10.35	3551	7.64	1.53
25-35	1.17e+04	11.07	7757	7.72	4.01
35-45	1.17e+04	14.13	9773	7.84	4.08
45-Infin	1.17e+04	14.15	10712	7.85	4.06

Table 4.6: Embedded Simulation Timing Test for Each pT bin with 11,701 events thrown and passing the dijet filter

p_T Bin (GeV)	Filter Set-Up	CPU Time	Real Time	Time (s)
3-4	Full	1.64e+06	1.64e+06	6.08e+08
4-5	Full	1.54e+06	2.44e+06	9.67e+07
5-7	Full	1.85e+06	1.98e+06	2.77e+07
7-9	Full	1.71e+06	1.85e+06	4.57e+06
9-11	Full	1.66e+06	1.99e+06	1.19e+06
11-15	Trigger Only	1.76e+06	2.11e+06	1.01e+05
15-25	Trigger Only	1.98e+06	2.30e+06	1.20e+05
25-35	None	2.33e+06	2.60e+06	1.29e+05
35-45	None	2.37e+06	5.73e+06	1.65e+05
45-Infin	None	2.20e+06	2.37e+06	1.65e+05

Table 4.7: Timing Table Continued

p_T Bin (GeV)	Events Thrown	Pythia Accepted	Trigger Accepted	Time (s)	MuDst+Pythia File size (GB)
3-4	1.00M	8.86e+02	5.07	4.55e+07	0.01
4-5	1.00M	2.76e+03	26.4	2.28e+07	0.05
5-7	500K	3.85e+03	95.7	9.13e+06	0.10
7-9	500K	1.39e+04	841	5.42e+06	0.56
9-11	500K	4.37e+04	4.89e+03	4.46e+06	2.67
11-15	450K	4.50e+05	4.46e+04	3.88e+06	24.6
15-25	400K	4.00e+05	1.21e+05	4.14e+06	52.4
25-35	400K	4.00e+05	2.66e+05	4.43e+06	137
35-45	200K	2.00e+05	1.67e+05	2.83e+06	67.7
45-55	200K	2.00e+05	1.84e+05	2.83e+06	69.6
55-65	150K	1.50e+05	1.38e+05	2.12e+06	52.2
65-75	60K	6.00e+04	5.51e+04	8.49e+05	20.9
75-Infin	60K	6.00e+04	5.51e+04	8.49e+05	20.9

Table 4.8: Second Draft of a Final Embedded and Filtered Simulation Request

events needed for these bins. In addition, very few events passed the trigger at the lowest p_T bin of 3-4 GeV. It was decided to save the large amount of computing time necessary for the 3-4 bin and not request any events. The modified request as can be seen in Table 4.9. The updated embedding request is for a total of 4.42 M events of which 2.0 M will pass the dijet pythia filter and 1.04 M will pass both the pythia and trigger filter. The total time is 6.18×10^7 seconds (1.96 CPU years) and will leave a footprint of 404 GB. This is the first doubly filtered embedding request at STAR and will be used for the pp500 dijet cross-section measurement.

p_T Bin (GeV)	Events for 12pb^{-1}	Events Requested	Pythia Accepted	Trigger Accepted	Time (s)	MuDst+Pythia size (GB)
4-5	1.78e+10	1.00M	2.76e+03	26.4	2.28e+07	0.05
5-7	8.99e+09	500K	3.85e+03	95.7	9.13e+06	0.10
7-9	1.86e+09	500K	1.39e+04	841	5.42e+06	0.56
9-11	5.33e+08	500K	4.37e+04	4.89e+03	4.46e+06	2.67
11-15	2.65e+08	450K	4.50e+05	4.46e+04	3.88e+06	24.6
15-25	6.86e+07	400K	4.00e+05	1.21e+05	4.14e+06	52.4
25-35	4.11e+06	400K	4.00e+05	2.66e+05	4.43e+06	137
35-45	5.19e+05	400K	4.00e+05	3.34e+05	5.65e+06	139
45-55	9.51e+04	100K	1.00e+05	9.19e+04	1.41e+06	34.8
55-65	2.17e+04	25K	2.50e+04	2.30e+04	3.54e+05	8.71
65-75	5.67e+03	6K	6.00e+03	5.51e+03	8.49e+04	2.09
75-Infin	1.30e+03	3K	6.00e+03	2.76e+03	4.24e+04	1.04

Table 4.9: Final Embedded and Filtered Simulation Request

4.7 Dijet Yields

This section discusses the raw number of dijets observed in the data as a function of the invariant mass, which is shown in Table 4.10. The size of the invariant mass bins indicated in this table were determined based upon an $\sim 9\%$ resolution except for the first bin which has a 13% resolution. Ideally, narrow bins are preferred for accuracy, but require much more statistics. The binning resolution used in the dijet cross-section measurement was determined based upon the jet transverse momentum resolution. The jet resolution is defined by the following equation:

$$\text{jet resolution} = \frac{p_{T3} - p_{T4}}{p_{T3} + p_{T4}} \tag{4.13}$$

where $p_{T3(4)}$ is the jet transverse momentum of one of the jets in the dijet pair and both jets are required to have fired a JP trigger. The jet resolution as a function of jet p_T is displayed on Fig 4.8. This distribution was then projected onto y-axis over specific ranges in jet p_T to obtained the plot shown in Fig 4.9. The jet resolution for each jet p_T was then fit with a gaussian distribution and the variance of each fit was

$\sim 14\%$. Using this value as the jet resolution, then the invariant mass resolution is just this value divided by $\sqrt{2}$ leading to the resolution of $\sim 9\%$ quoted above.

M_{ij} [GeV]	Yields	σ_Y
23-30	111039	333.225
30-36	209247	457.435
36-43	193603	440.003
43-52	133397	365.236
52-62	62993	250.98
62-74	28373	168.44
74-89	11580	107.6
89-106	3812	61.74
106-127	1290	35.9
127-152	366	19.1

Table 4.10: The raw dijet yields and the associated error, σ_Y, for each invariant mass bin for the JP2 trigger.

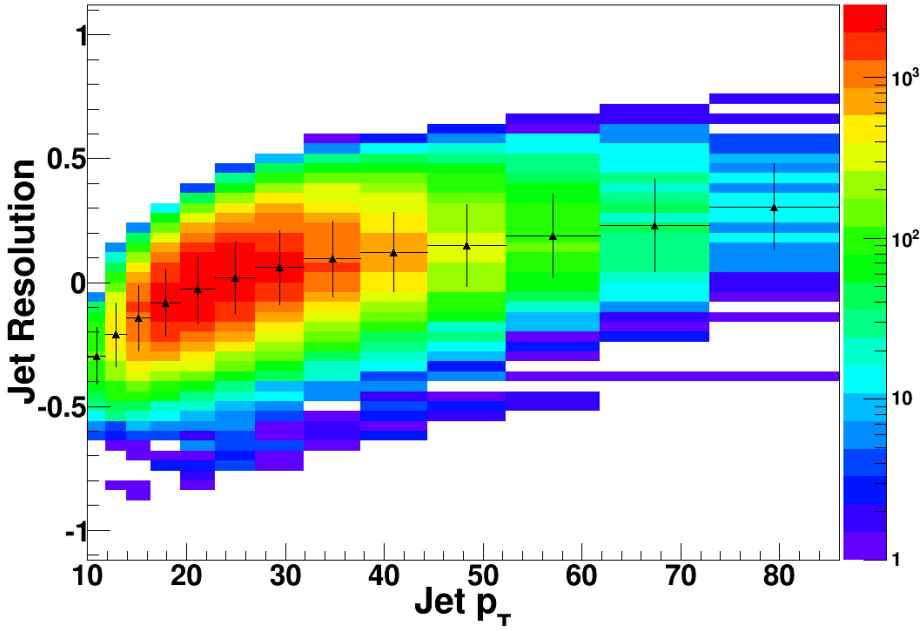

Figure 4.8: **Jet Resolution Vs Jet** p_T - The jet resolution as a function of jet p_T. The black dots are average over each p_T bin and the errors are the RMS of the distribution.

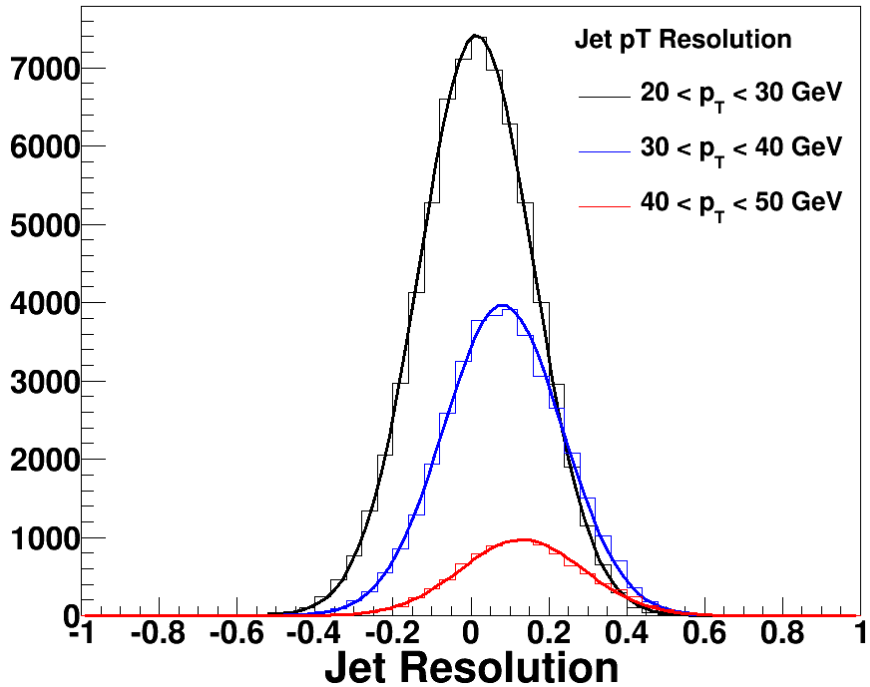

Figure 4.9: **Jet Resolution** - A plot of the jet resolution for different jet p_T regions each fit with a gaussian distribution. Black: $20 \leq$ jet $p_T \leq 30$ GeV Blue:$30 \leq$ jet $p_T \leq 40$ GeV Red: $40 \leq$ jet $p_T \leq 50$ GeV

In order to compare the created embedding sample to the data, each partonic p_T bin is normalized according to their relative cross-sections. The relative cross section and the normalization values are listed in Table 4.11 for each partonic p_T bin. The relative cross section values were determined by throwing 1×10^6 events for each partonic p_T bin using PYTHIA [49]. A large number of events were used in order to be confident in the cross-section obtained for each bin. These were not the number of events thrown for the embedding sample and no actual event reconstruction was performed. The relative normalization values, which allow for the combination of all the partonic p_T bins, were determined from the following equation:

$$W_i = \frac{N_i * \sigma_{12}}{N_{12} * \sigma_i}. \tag{4.14}$$

where σ_i are the relative cross sections, the number of event thrown is N_i, i represents

the p_T bin and in our case goes from 1 to 12. Once all the p_T bins in the embedding sample are properly combined and normalized by the number of events, comparisons between the data and the embedding sample can be made.

p_T bin	cross-section [σ]	Events Thrown [N]	Normalization [W]
4-5	1.48e+00	2.96e+08	1.34e-02
5-7	7.40e-01	5.95e+07	5.32e-03
7-9	1.55e-01	1.64e+07	7.08e-03
9-11	4.50e-02	5.38e+06	8.00e-3
11-15	2.21e-02	4.24e+05	1.28e-03
15-25	5.71e-03	3.77e+05	4.42e-03
25-35	3.43e-04	3.58e+05	7.01e-02
35-45	4.32e-05	3.73e+05	5.77e-01
45-55	7.92e-06	9.39e+04	7.94e-01
55-65	1.81e-06	2.35e+04	8.72e-01
65-75	4.74e-07	5.74e+03	8.12e-01
75-∞	1.95e-07	2.92e+03	1

Table 4.11: The estimated theoretical cross-section and the number events of thrown for the each partonic p_T bin

4.8 Data/Simulation Comparisons

In order to calculate a cross-section and compare to theoretical calculations, the raw dijet yields must be corrected for trigger and detector effects. These corrections are performed by comparing the detector response in the simulations with the generated or thrown response. Therefore, the integrity of the embedding sample must be checked by comparing the data and simulation at the detector level.

4.8.1 Vertex Re-weighting

The first distribution examined between the data and the embedding was the vertex distribution. This comparison, shown in Fig 4.10, clearly shows a large discrepancy. The embedding sample has a broader distributions than the data.

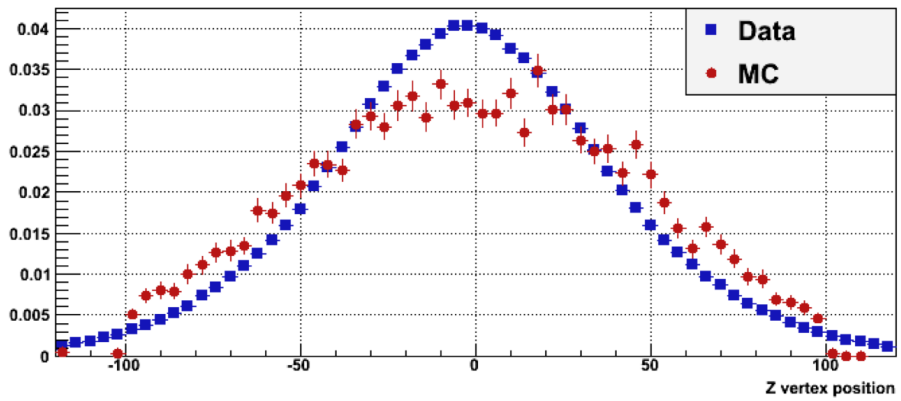

Figure 4.10: **Vertex Z position** - Data MC comparison of the vertex z-position

The z vertex distribution in the embedding sample is re-weighted to aligned it with the distribution observed in the data. The re-weighting is done by fitting the difference ratio, (Data-MC)/MC, shown in Fig 4.11. The fit function used, giving

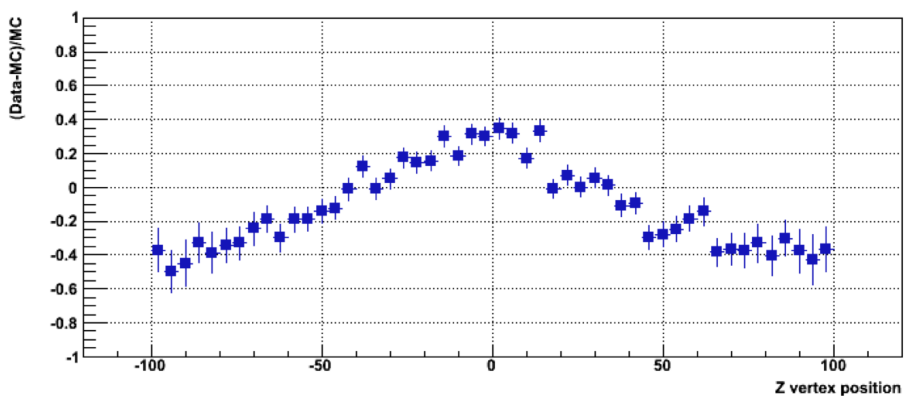

Figure 4.11: **Vertex Z position** - Data MC ratio of the vertex z-position

the $\chi^2/ndf \sim 1$, is combination of an exponential and polynomial function described as follows

$$\mathrm{VerZ}_{rw} = p_0 \exp^{-\frac{1}{2}(\frac{\mathrm{verZ}_{-p_1}}{p_2})^2} + p_3 + p_4 * verZ + p_5 * verZ^2 \tag{4.15}$$

where the value of the fit parameters $p_0 - p_5$ are indicated in Table 4.12.

Once the distributions in the embedding sample are scaled by the re-weighted vertex, the z vertex distribution between the data and MC becomes properly aligned

p_0	0.6641
p_1	-4.523
p_2	-32.34
p_3	0.6027
p_4	-1.577e-05
p_5	-3.316e-07

Table 4.12: Table of fit parameters for the vertex z distribution

as shown in Fig 4.12. All the comparisons shown in later sections have the vertex re-weighting already applied.

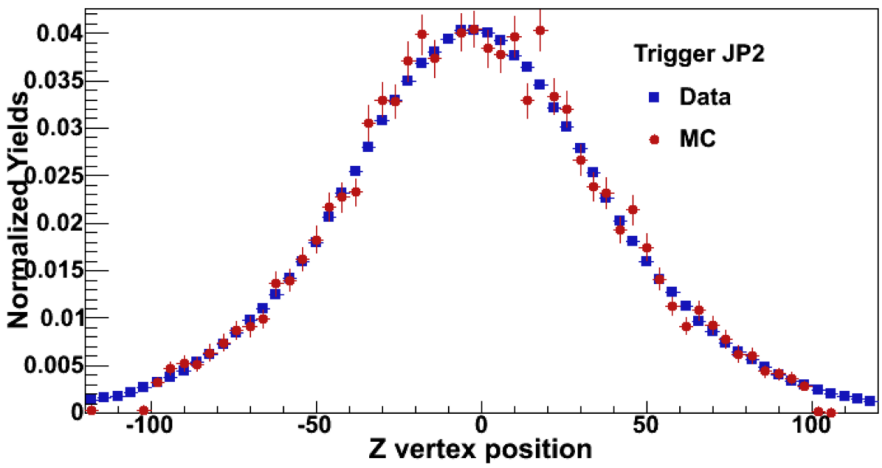

Figure 4.12: **Re-Scaled Vertex Z Position** - Data-embedding comparison of vertex z position after re-weighting.

4.8.2 Jet Comparisons

This sections compares the individual jet quantities that will compose the dijets. This comparison is demonstrated in Fig 4.13 - 4.15. The agreement between the data and MC in the jet $y - \phi$ space is excellent. There does exist some discrepancy between the data and MC in the jet p_T spectrum. At large jet p_T the embedding tends to under-estimate the pT spectrum of the data. However, due to the limited statistics at high jet p_T, the discrepancy observed is not of high concern.

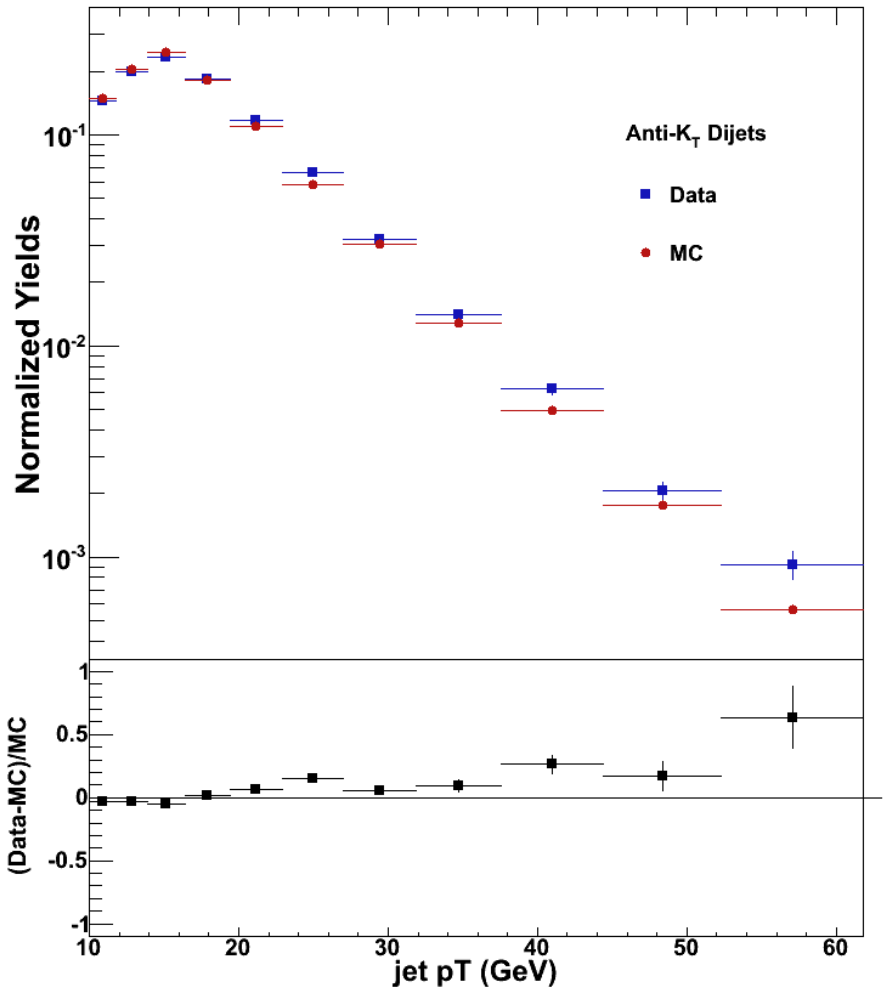

Figure 4.13: **Jet** p_T - Data-embedding comparison transverse jet momentum using the JP2 trigger

4.8.3 DiJet Comparisons

This section extends the data-MC comparisons to the dijet observables. Similar to the discrepancy in the jet p_T spectrum, the invariant mass spectrum exhibits the same behavior shown in Fig 4.16. The embedding underestimates the data in the large invariant mass regions. The agreement is excellent when examining the $\cos(\theta^*)$ distribution (Fig 4.17). The neutral energy ratio R_T for the same side and away side jet of the dijet is shown in Fig 4.18 and Fig 4.19 respectively. Both jets in the data appear to carry more neutral energy than those simulated in the embedding.

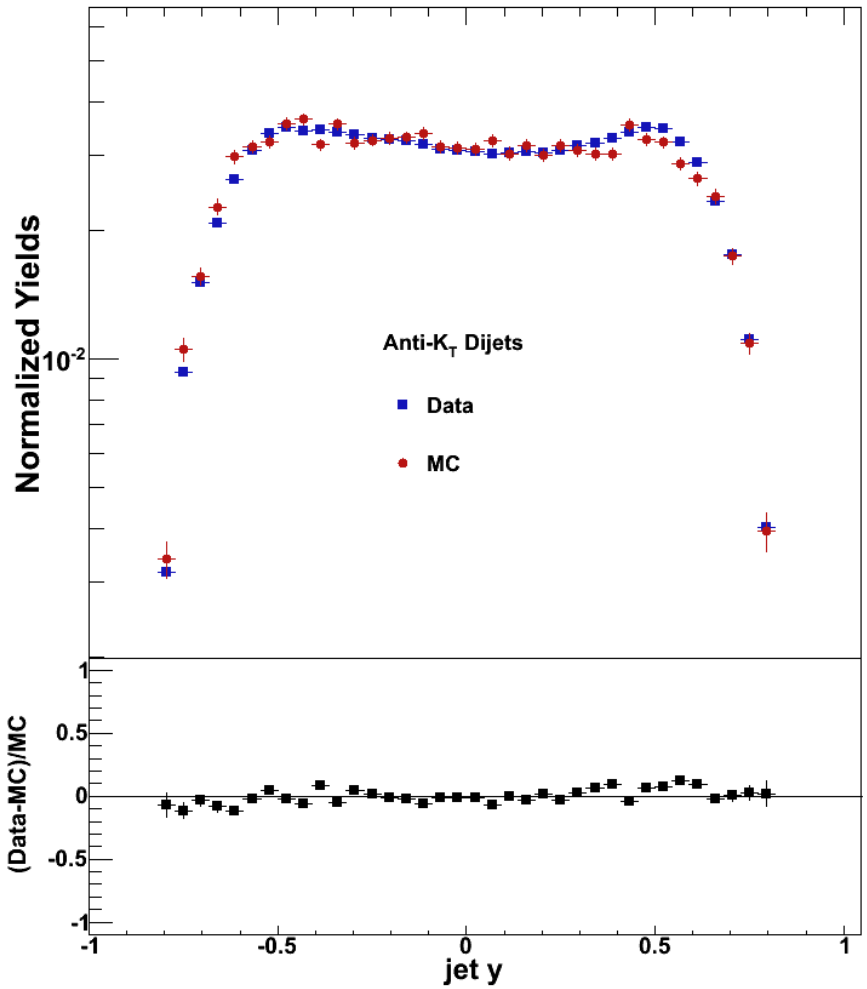

Figure 4.14: **Jet** y - Data-embedding comparison of jet rapidity using the JP2 trigger

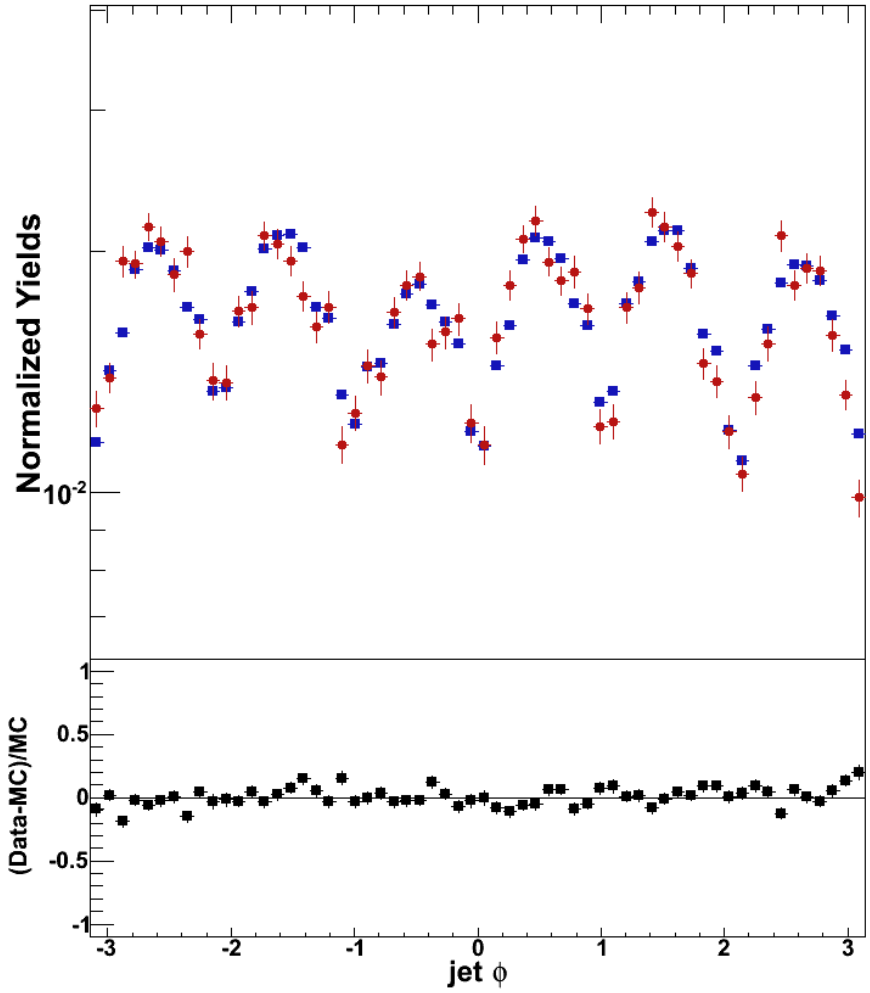

Figure 4.15: **Jet** ϕ - Data-embedding comparison of jet ϕ using the JP2 trigger

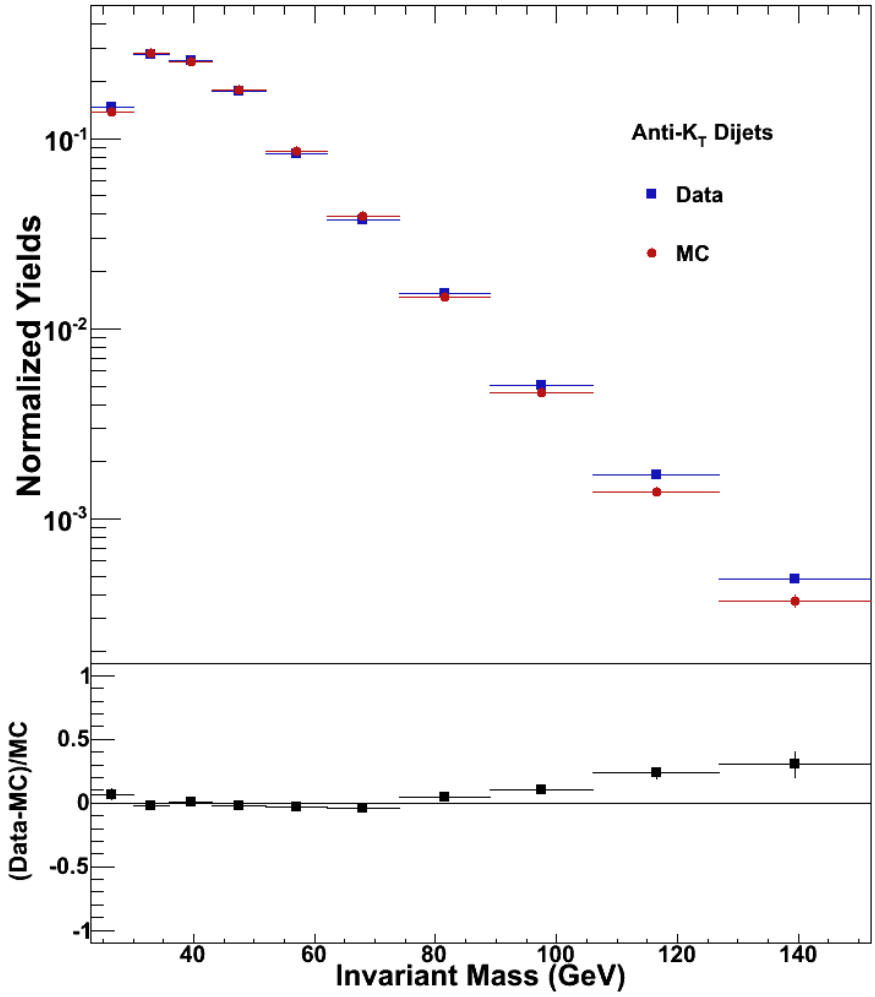

Figure 4.16: **Invariant Mass** - Data-embedding comparison of the Invariant Mass spectrum using the JP2 trigger

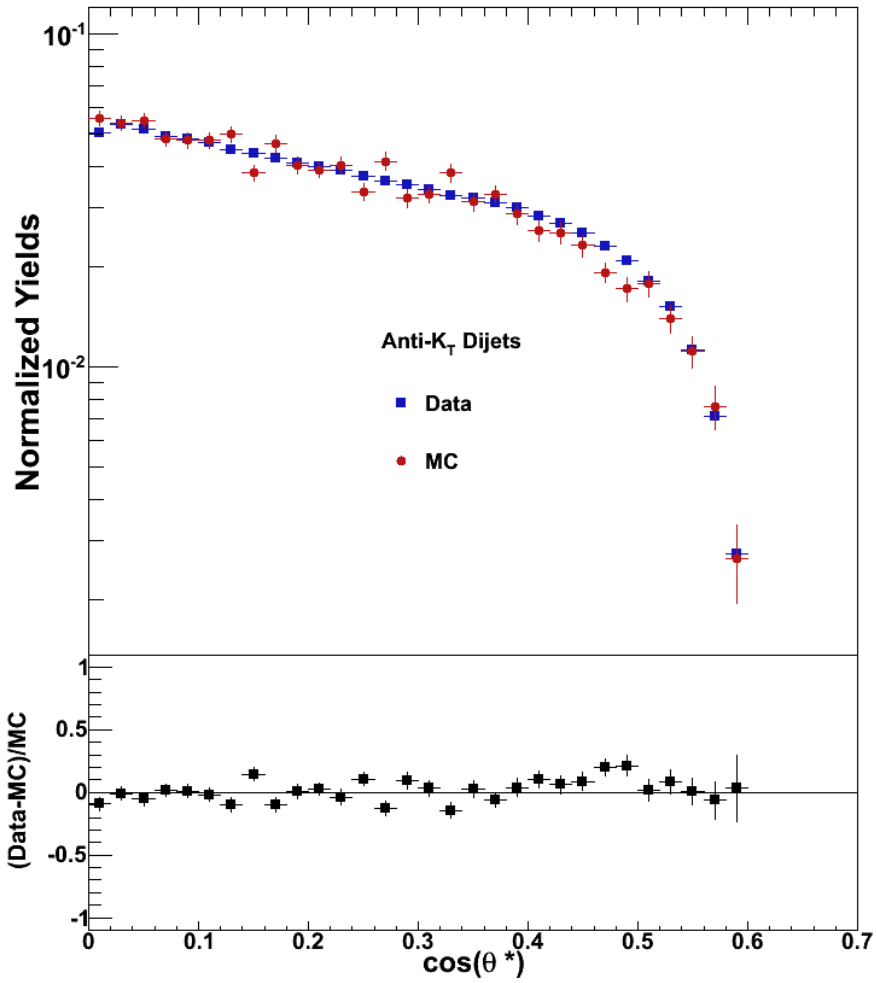

Figure 4.17: $cos(\theta^*)$ - Data-embedding comparison of $cos(\theta^*)$ using the JP2 trigger

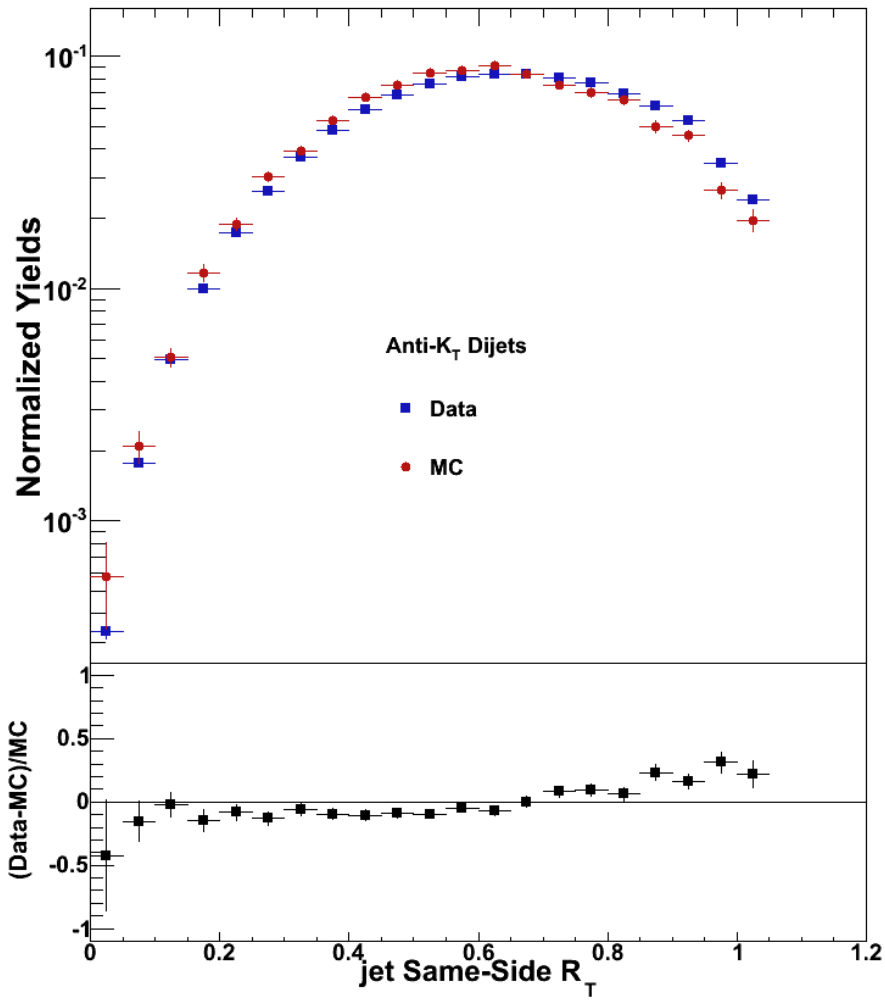

Figure 4.18: **Same-side jet neutral energy ratio** - Comparison of data to simulation for the same-side jet neutral energy ratio using the JP2 trigger

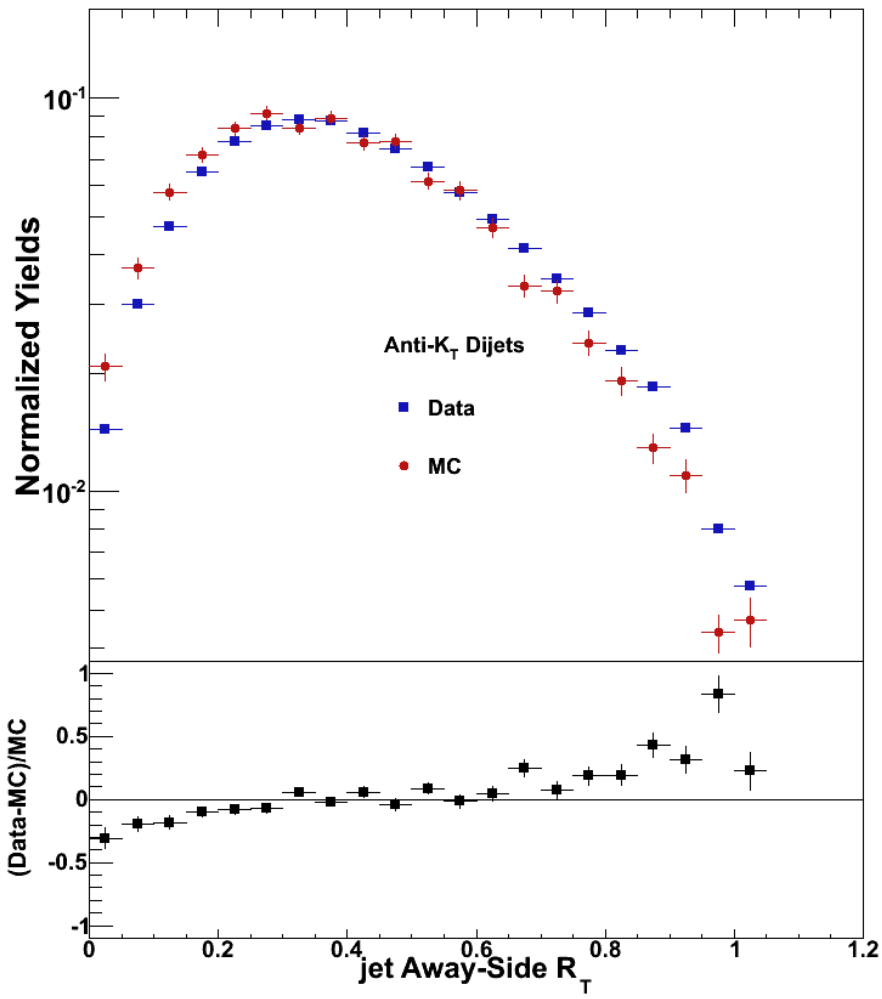

Figure 4.19: **Away-side jet neutral energy ratio** - Comparison of data to simulation for the away-side jet neutral energy ratio using the JP2 trigger

Chapter 5 The Dijet Cross Section

The previous chapter discussed the data and simulation samples that will be used in the dijet cross section calculation. This chapter details the procedure to use that information to unfold from the raw dijet yields to the fully corrected spectrum. The dijet cross section is measured using the 2009 data sample of 8.7 pb^{-1} in proton-proton collisions at $\sqrt{s} = 500$ GeV. The measurement is taken at mid-rapidity, $|y_{max}| \leq 0.8$, as a function of the dijet invariant mass, M_{ij}, in the range of $30 < M_{ij} < 150$ GeV.

5.1 Unfolding

The data collected from any experiment is distorted by both detector limitations and physics effects. The detector will have limited fiducial coverage and a finite resolution and some physics effects include pile-up, background, and the underlying event. In order to extract a meaningful physics observable, one must unfold the measured distribution from all distortions to extract the truth-level distribution. The true distribution represents the measurement if it were made with infinite statistics and an ideal detector. In this section, we will compare several unfolding algorithms used to move from the measured observable to the true physical quantity.

Let A be the simulated folding matrix, which relates the measured distribution to the true distribution. When A acts upon the true distribution, N^{corr}, it returns the measured data distribution N^{raw}

$$A \cdot N^{corr} = N^{raw}. \tag{5.1}$$

In this analysis N^{raw} is a vector representing either the raw dijet invariant mass yields from the data and N^{corr} is the corrected dijet yields at the particle level. In order to compare any observable from different experiments, it is required to correct for the

detector and background effects to obtain a true distribution. To recover the true distribution, N^{corr}, requires using the exact inversion of the folding matrix and applying it to the measured distribution. The matrix A is determined from the embedded simulation sample and relates the known particle level and detector level invariant mass distributions. However, this method assumes the matrix can be inverted, which is unlikely, and may lead to completely unacceptable rapidly oscillating solutions. [52]

Fortunately, there are unfolding methods to extract the true distribution without large oscillations. The starting point for the unfolding process begins with the raw dijet yields measured in $\sqrt{s} = 500$ GeV proton-proton collisions and plotted as a function of the invariant mass. The following equation describes the correction from the measured, N_j^{raw}, to the particle-level/true, N_i^{cor}, dijet invariant mass yields:

$$N_i^{cor} = R_{2i} \sum_j M_{ij} R_{1j} N_j^{raw} \tag{5.2}$$

where i and j are the invariant mass bins of the true and measured distributions, respectively. The R_{2i} term is the dijet reconstruction efficiency, M_{ij} is the response matrix and encapsulates the effects of detector resolution and bin migration, and R_{1j} is "fake" jet finding efficiency. These term will be further examined in subsequent sections.

data measured	data dijets	observed events
measured	detector-level dijets	effect
true	particle-level dijets	cause

Table 5.1: Different unfolding algorithms use different terminology when discussing the types of distributions. This table relates the terminology by row (true distribution = particle level dijets = cause).

5.1.1 Matching Dijets

In order to determine the corrected dijet yields in Eq 5.2 we must first define a "matched" jet. Matching is a vital part in determining R_{2i}, M_{ij}, and R_{1j}. The process starts with the list of the detector level dijets events produced from the embedding sample with all detector and dijet cuts applied. Then for each detector level jet in the dijet pair, loop through all the particle level jets in the event and calculate

$$dR = \sqrt{(\eta_{det} - \eta_{particle})^2 + (\phi_{det} - \phi_{particle})^2}. \tag{5.3}$$

This checks if the jet axis of a particle jet aligns with the jet axis of a detector-level jet of the same event, which is diagramed in Fig 5.1. For this analysis, a matched jet only occurs if $dR < 0.5$. This sets a limit ensuring the detector level jet was caused by the particle level jet. In other words, the particle level jet, the "cause", created the detector level jets, "the effect". To have a matched dijet event, both detector level jets must have a matching particle level jet.

The possibility exists for a detector-level dijet to occur with no corresponding particle-level dijet. This is known as a fake dijet event, since there is an effect with no known cause. The R_1 term from Eq. 5.2 corrects for these false dijet events and can be expressed as

$$R_1 = \frac{\text{number of matched detector-level dijet events}}{\text{number of total detector-level dijet events}}. \tag{5.4}$$

Fortunately, since we are only analyzing a rare high energy observable, the number of fake dijet events is negligible, which makes $R_1 \sim 1$. This can be seen from Fig 5.2 and we can therefore safely ignore the R_1 term and Eq. 5.2 becomes

$$N_i^{cor} = R_{2i} \sum_j M_{ij} N_j^{raw}. \tag{5.5}$$

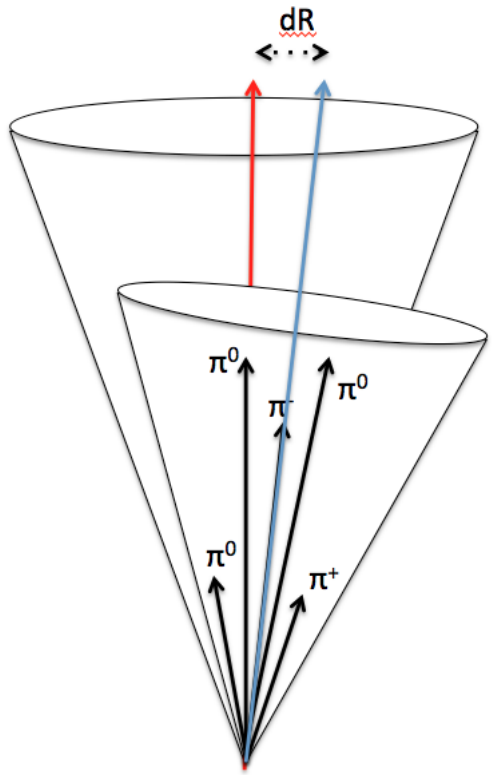

Figure 5.1: **Matching Jets** - Schematic showing the procedure for matching jets.

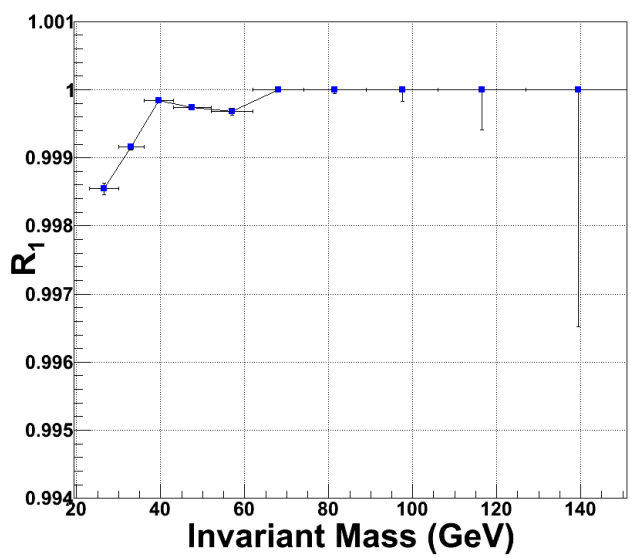

Figure 5.2: **Efficiency of "fake" jets** - R_1: The ratio of matched detector-level dijet events to all detector-level dijet events

Matching also plays a role in creating the response matrix, M_{ij}, which relates the detector level dijet invariant mass spectrum to the particle level invariant mass spectrum. Each bin contains the number of dijet events where a detector dijet invariant mass j is matched to a particle dijet of invariant mass i. It is important to note that no cuts have been placed on the particle dijet events at this point. The only requirements are that the each have a $\mathrm{p}_T > 5$ GeV and match to a detector level dijet. Fig 5.3 displays the distribution of the response matrix with each bin in histogram being an element in the matrix.

Finally, the efficiency calculation, R_{2i} is required to determine the corrected number of dijet yields. The efficiency is expressed as

$$R_2 = \frac{\text{number of particle dijet events}}{\text{number of matched particle dijet events}}. \tag{5.6}$$

It is important to note that in the above ratio the events in the numerator pass all the final dijet cuts, while the denominator only has the matching requirement applied.

Provided the numbers indicated above, R_{2i}, M_{ij}, and R_{1j}, and applying them to the raw dijet yields, the corrected yields could technically be calculated. However, performing this calculation would subject the result to large fluctuations from the low statistics of the off diagonal elements. It would require producing lots of simulated events to get enough statistics to ensure that the uncertainties do not dominate in the unfolding. In order to address this sort of problem with the unfolding we examine three unfolding algorithms: the bin-by-bin, the iterative Bayesian, and Singular Value Decomposition methods.

The C++ code provided by the RooUnfold program [53] will be implemented for the three different unfolding methods. A commonality between all three unfolding methods is the RooUnfoldResponse object, which is initialized with three histograms as follows: RooUnfoldResponse(const TH1* measured, const TH1* truth, const TH2* response) where `measured` is the detector level invariant mass spectrum, `truth` is the

particle level dijet invariant mass spectrum, and `response` is the detector vs particle invariant mass spectrum as shown in Fig 5.3.

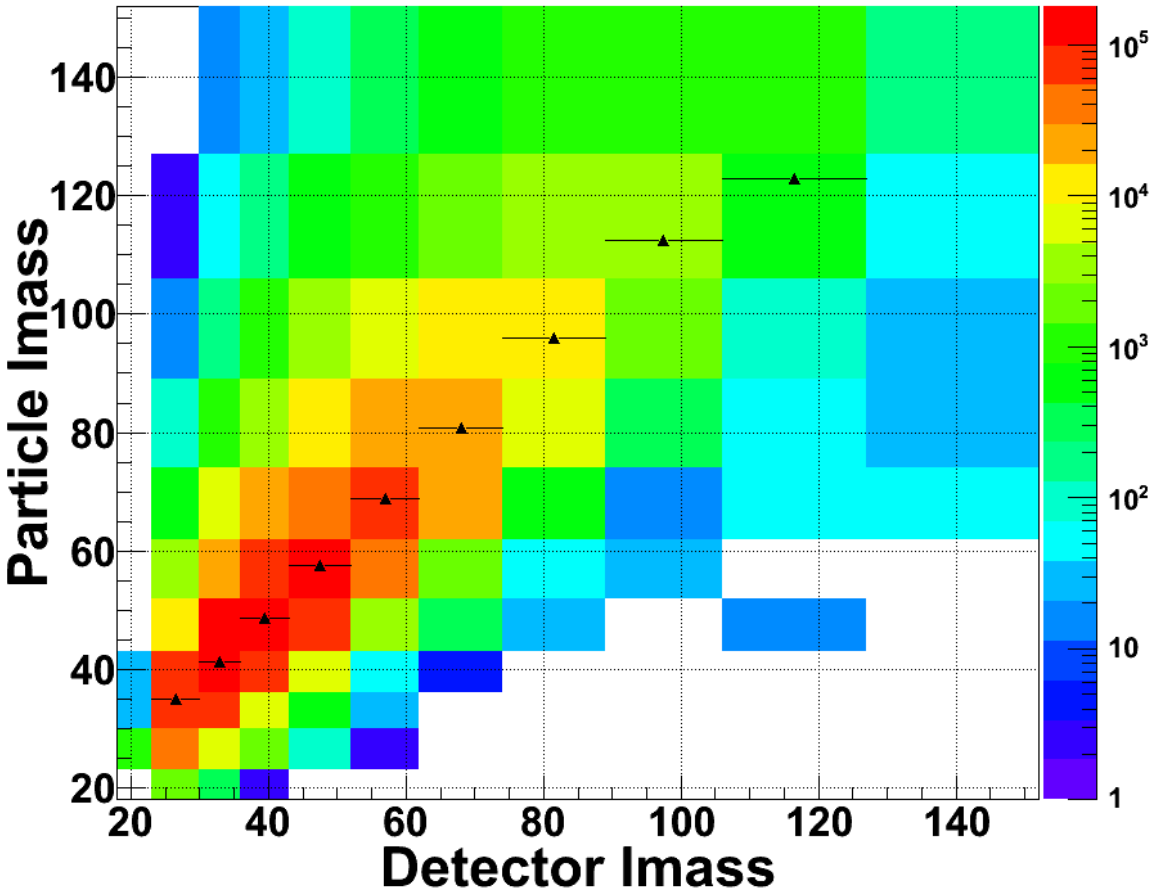

Figure 5.3: **Detector vs Particle Level Invariant Mass Spectra** - The particle-level invariant mass spectrum as a function of the corresponding detector-level dijet invariant mass spectrum. The black dots are the average of the distribution for each bin.

5.1.2 Bin-By-Bin Unfolding Methodology

Many previous STAR analyses implemented the bin-by-bin unfolding procedure to determine the correction factors needed to extract the true distribution of an observable. The bin-by-bin method is often used due to its simplicity and easy implementation.

Let T_i be the expected number of events in bin i of the particle/true level invariant mass spectrum, which is obtained from the embedding sample. Let D_i be the expected number of events in bin i of the detector/measured level invariant mass spectrum, which is also obtained from the embedding sample [54]. The values of T_i come from the `truth` histogram which had all the dijet cuts implemented. The D_i values are obtained from the `measured` histogram, which has all the final state dijet cuts and all detector level cuts . Then let N_i^{raw} be the actual number of events in bin i of the measured invariant mass spectrum.

The correction factor for bin i to the observed invariant mass spectrum is just the following ratio:

$$C_i \equiv \frac{T_i}{D_i}. \tag{5.7}$$

These correction factors, C_i, encapsulates the R_{2i}, M_{ij}, and R_{1j} of the unfolding equation (Eq. 5.2) into one simple factor. The final corrected yields, the true/particle level invariant mass spectrum, for bin i is

$$N_i^{corr} \equiv C_i \cdot N_i^{raw}. \tag{5.8}$$

N_i^{corr} is the estimation of the true-level invariant mass spectrum. When performing this correction, a strong consideration must be taken in the definition of the true-level spectrum. If the number of events of the true-level T_i are derived from the particle-matched dijet events (the y projection of the 2D histogram `response`), then the efficiencies R_{2i} have been disregarded in the unfolding matrix, M_{ij} and must be applied afterwards on each bin. If T_i are derived from the all particle dijet events (the 1-D histogram `truth`), then the efficiencies R_{2i} lie within in the unfolding matrix. This must be carefully expressed when executing any unfolding procedure.

The bin-by-bin method is only valid when there are not large migrations between bins. It does not take into account correlations across bins. These correlations are

not large as long as the kinematic bins are on the order of or larger than the width of the smearing distribution.

5.1.3 Iterative Bayesian Unfolding Methodology

Subjective probability is the foundation of Bayesian concepts. In a Bayesian perspective, once an experiment is conducted and data observed, all knowledge about an observable is contained in the actual observed data and in the prior information about the observable [55]. To stay germane to this analysis, the produced embedding sample inherently contains the subjective opinion of many previous experiments. The Bayes theorem can be expressed by the following equation

$$P\left(C_i|E_j\right) = \frac{P\left(E_j|C_i\right) P_0\left(C_i\right)}{\sum_{\ell=1}^{n_C} P\left(E_j|C_\ell\right) P_0\left(C_\ell\right)}. \tag{5.9}$$

$P\left(C_i|E_j\right)$ represents the probability that the jth effect (E_j) is due to the ith cause (C_i).[56]. In this analysis C_i refers to the particle level dijets reconstructed in the ith kinematic bin and E_j to the detector level dijets reconstructed in the jth kinematic bin. $P_0(C_i)$ is known as the prior distribution and is the initial probability for the ith cause to occur. $P\left(E_j|C_i\right)$ is the probability of the ith cause to produce the effect E_j. Eq. 5.9 can be interpreted as the likelihood of observed event E_j to have been caused by event C_i as proportional to the probability of the cause times the probability of the cause to produce the effect. The denominator in equation 5.9 is the sum over the total number of causes. The information in Eq 5.9 is represented in the response matrix. Each $P\left(C_i|E_j\right)$ corresponds to the jth bin divided by i rows in the jth column. The Bayesian Method properly accounts for correlations between bins and therefore bin migration effects as well.

The expected number of events from each cause C_i, $\hat{n}\left(C_i\right)$, is equal to the number of observed events, $n(E_j)$, from the data times the response matrix, $P(C_i|E_j)$,

summed over all possible observed bins. This can be expressed as follows:

$$\hat{n}\left(C_i\right) = \frac{1}{\epsilon_i} \sum_{j=1}^{n_E} n\left(E_j\right) P\left(C_i|E_j\right) \tag{5.10}$$

where $\epsilon_i \equiv \sum_j^{n_E} P\left(E_j|C_i\right)$ is the efficiency of detecting effects from the cause C_i. This efficiency and the $P(C_i|E_j)$ are just the R_2 and M_{ij} of Eq 5.2, repectively. This can be used to estimate the true total number of events, the final probabilities of the causes and the overall efficiency [56]:

$$\hat{N}_{true} = \sum_{j=1}^{n_C} \hat{n}\left(C_i\right) \tag{5.11}$$

$$\tag{5.12}$$

$$\hat{P}\left(C_i\right) \equiv P\left(C_i|n(E)\right) = \frac{\hat{n}\left(C_i\right)}{\hat{N}_{true}} \tag{5.13}$$

$$\tag{5.14}$$

$$\hat{\epsilon} = \frac{N_{obs}}{\hat{N}_{true}} \tag{5.15}$$

The iterative process for this unfolding methodology can proceed when this initial information is obtained. Begin by choosing an initial distribution $P_0\left(C_i\right)$ for each bin obtained from the embedding sample, which is the `truth` histogram from the RooUnfoldResponse object. The initial number of events is $n_0(C_i) = P_0(C_i)N_{obs}$. The iterative steps described in detail by D'Agostini [56] are summarized as follows:

1. choose the initial distributions $P_0\left(C_i\right)$
2. calculate $\hat{n}\left(C_i\right)$ and $\hat{P}\left(C_i\right)$
3. make a χ^2 comparison between $\hat{n}\left(C_i\right)$ and $n_0\left(C_i\right)$
4. replace $P_0\left(C_i\right)$ by $\hat{P}\left(C_i\right)$ and $n_0\left(C_i\right)$ by $\hat{n}\left(C_i\right)$ and start again. If after the second iteration the value of the χ^2 is "small enough" stop the iteration otherwise go to step 2.

Again, it is important to note that the particle level dijet invariant mass spectrum used for the $P_0(C_i)$ distribution does not require any matching to the detector level and has all the dijet cuts applied. The closer the initial distribution is to the true/particle-level distribution, the better the agreement and fewer iterations needed. Four iterations were performed in order to reach a reasonable χ^2 1 distribution. Also, there was no robust implementation of the errors. The major disadvantage of using the Bayesian method is if a very larger number of iterations are needed, the corrected distribution will have large fluctuations around the true distribution. This results in the exact same problem described by the matrix inversion method.

5.1.4 Singular Value Decomposition Methodology

The SVD procedure uses some basic information, referred to as a regularization condition, about the solution to suppress unphysical oscillations. For example, the regularization can be as simple as requiring the corrected yields to be positive. Singular value decomposition (SVD) methods are based upon the following linear algebra theorem: Any $m \times n$ matrix $\mathbf{A}$ whose number of rows m is greater than or equal to its number of columns n, can be written as the product of an $m \times m$ column-orthogonal matrix $\mathbf{U}$, an $m \times n$ diagonal matrix $\mathbf{S}$ with positive or zero elements (the singular values), and the transpose of an $n \times n$ orthogonal matrix $\mathbf{V}$. This is expressed by the following:

$$A = USV^T \tag{5.16}$$

$$UU^T = U^TU = I \tag{5.17}$$

$$VV^T = V^TV = I \tag{5.18}$$

$$S_{ij} = 0 \text{ for } i \neq j, \tag{5.19}$$

$$S_{ii} \equiv s_i \geq 0. \tag{5.20}$$

The s_i are called singular values of the matrix A and U and V are called the left and right singular vectors. In addition, the singular values s_i are in a non-increasing sequence, which is achieved by simultaneously swapping pairs of singular values and the corresponding columns of U and V. Once the response matrix is in the SVD form, its properties are readily analyzed and manipulated.

Inserting the SVD version of the response matrix into the folded equation, Eq 5.1, we have:

$$USV^T N^{corr} = N^{raw} \tag{5.21}$$

which we rewrite as

$$SV^T N^{corr} = U^T N^{raw}. \tag{5.22}$$

These are ultimately rotations of the of the unknown truth vector and the measured distribution. In order to form a diagonal system of equations we express the above equation as

$$z = V^T N^{corr}, \qquad d = U^T N^{raw} \tag{5.23}$$

which gives

$$Sz = d \qquad \text{and} \qquad z = S^{-1} d. \tag{5.24}$$

Since the matrix S is diagonal, it can be easily be inverted by inverting the singular values. This would be adequate for our needs if all the components of the rotated vector d (or the measured vector b) were statistically significant and if neither of the singular values s_i were too small. However, this exact case is highly unlikely and the addition of the measurement errors causes one to examine the issue with a different approach.

One should consider the weighted method of the least squares problem, which has the following equation minimized:

$$\sum_{i=1}^{n_b} \left(\frac{\sum_{j=1}^{n_x} A_{ij} N_j^{corr} - N_i^{raw}}{\Delta N_i^{raw}} \right)^2 = \min \tag{5.25}$$

where ΔN^{raw} is the error of N_i^{raw}. The general case can be written as

$$(Ax - N^{raw})^T B^{-1} (AN^{corr} - N^{raw}) = \min \tag{5.26}$$

where B is the covariance matrix of the measured vector N^{raw}. After rescaling of the equations according to the covariance matrix and performing a regularization of the expression to minimize oscillations, one can properly unfold the distribution to get a meaningful solution of the true distribution. The SVD method is described in further detail in Ref [52]. The regularization parameter used in this analysis is $k = 5$. This unfolding method provides a loop free algorithm to data-unfolding, considers bin migration effects, suppresses insignificant rapidly oscillating terms and properly determines the correlated errors.

5.1.5 Unfolding Comparisons

This section examines the differences between the unfolding schemes. Three different unfolding methods were implemented to obtain the corrected dijet yields as a function of the invariant mass: the bin-by-bin, the iterative Bayesian, and SVD methodology. In this comparison, the calculated unfolded invariant mass distributions using each method are then divided by the results obtained from using the bin-by-bin unfolding method.

The results are shown in Fig 5.4, where the bin-by-bin is in black, the Bayesian is in red, and the SVD is in blue. Obviously, the bin-by-bin unfolding method values lie at one. The interesting aspects of this analysis are the Bayesian and SVD comparisons, which overall do not deviate from the bin-by-bin unfolding method. This is excepted

since the distribution of the response matrix is very linear, which highlighted by the black points in Fig 5.3. At most, both the Bayesian and SVD methods increase the cross section by $\sim$10% at the lowest invariant mass bins. This also makes sense because the lower invariant mass bins are narrower than the high invariant mass bins and correlations across bins are more likely too occur. The bin-by-bin unfolding method is unable to account for these correlations and therefore under predicts the cross-section at the lowest invariant mass bins.

The SVD unfolding method was selected in extracting the dijet invariant mass spectrum at STAR due to its ability to account of bin correlations without implementing an iterative procedure.

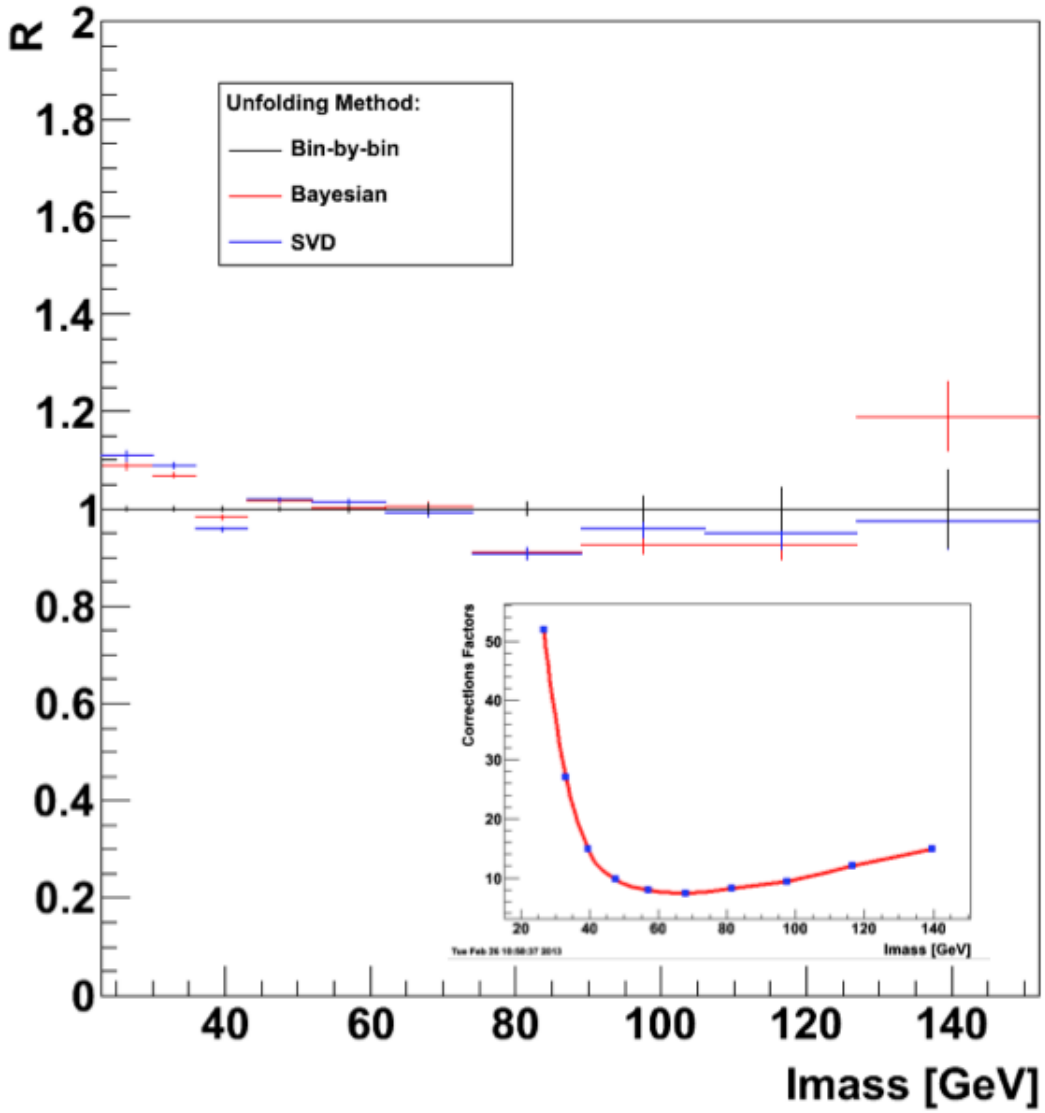

Figure 5.4: **Unfolding Method Comparison** - A comparison of the corrected yields using each unfolding algorithm to the bin-by-bin unfolding algorithm as a function of the dijet invariant mass. The red (blue) is the ratio of the Bayesian (SVD) corrected yields to the bin-by-bin yields. The small inlet on the bottom right shows the correction factors from the bin-by-bin unfolding method as a function of the invariant mass.

5.2 Dijet Cross Section

The formal equation for the dijet cross section is:

$$\frac{d^2\sigma}{dM_{ij}d|y_{max}|} = \frac{1}{\int \mathcal{L}dt} \cdot \frac{1}{\Delta M_{ij}\Delta|y_{max}|} \cdot N^{corr} \tag{5.27}$$

where N^{corr} are the corrected yields, ΔM_{ij} are the invariant mass bins, Δy_{max} is the rapidity range and $\int \mathcal{L}dt = 8.47pb^{-1} \pm 13\%$ is the integrated luminosity for JP2 trigger.

The corrected yields, phase space, and double differential cross sections are listed for each invariant mass bin in Table 5.2. Then using the luminosity values determined in Section 2.4 the dijet cross section is calculated and its values are shown in fifth column. The statistical errors associated with corrected yields and the cross section are indicated in third and sixth columns, respectively. Fig 5.5 plots the dijet cross section as function of the dijet invariant mass with the systematic errors associated with the measurement (hashed bands). The contributing factors to the systematic are discussed in Section 5.3.

ΔM_{ij} [GeV]	N^{corr}	δN^{corr}	PS	σ [μb]	$\delta\sigma^{stat}$
23-30	6.41e+06	±4.17e+04	5.6	1.35e-01	±8.80e-04
30-36	6.16e+06	±2.14e+04	4.8	1.51e-01	±5.27e-04
36-43	2.76e+06	±9.14e+03	5.6	5.83e-02	±1.93e-04
43-52	1.34e+06	±3.93e+03	7.2	2.19e-02	±6.45e-05
52-62	5.26e+05	±1.79e+03	8.0	7.77e-03	±2.64e-05
62-74	2.16e+05	±9.14e+02	9.6	2.66e-03	±1.12e-05
74-89	8.94e+04	±4.64e+02	12	8.81e-04	±4.57e-06
89-106	3.49e+04	±2.31e+02	13.6	3.03e-04	±2.01e-06
106-127	1.48e+04	±1.51e+02	16.8	1.04e-04	±1.06e-06
127-152	5.18e+03	±6.61e+01	20	3.06e-05	±3.90e-07

Table 5.2: The corrected yields, phase space and cross section values as a function of the dijet invariant mass. $\Delta|y_{max}| = 0.8$, PS = phase space = $\Delta M_{ij}\Delta|y_{max}|$, σ represents the double differential cross section and $\delta\sigma$ are the associated errors.

The theoretical dijet cross section values are determined using the CTEQ6 parton distribution functions [] [57]. The systematic errors on the theoretical calculation are

determined by altering the renormalization scale in theory by a factor of 2 and 0.5. The difference between the original theoretical dijet cross section and the altered values sets the width of the systematic errors for the theory. The theoretical calculations for each renormalization scale are shown in Table 5.3. This is the orange band shown in Fig 5.5. It is desirable to estimate the contribution of the non-pertubative effects (i.e. underlying event and hadronization), which occur when transitioning from the parton level to the particle level. Therefore, the data is unfolded to the parton level as well as the particle level. The difference in the calculated dijet cross section at the parton and particle level estimates non-pertubative components. This cross section difference, $\sigma_{particle} - \sigma_{parton}$ is then added to the theoretical calculation and is the cyan band in Fig 5.5. The lowest and highest invariant mass bins are not presented in the final result and are simply used as buffer bins, which are needed to properly account for bin migrations in and out of these bins.

Mass Bin[GeV]	$\sigma_{theory}(\mu)$ [μb]	$\sigma_{theory}(2\mu)$ [μb]	$\sigma_{theory}(0.5\mu)$ [μb]	ue+had
23-30	3.08e-01	2.25e-01	4.44e-01	-4.80e-02
30-36	1.62e-01	1.39e-01	1.82e-01	3.21e-02
36-43	6.15e-02	5.31e-02	6.70e-02	1.50e-02
43-52	2.26e-02	1.95e-02	2.45e-02	4.85e-03
52-62	8.09e-03	6.93e-03	8.91e-03	1.48e-03
62-74	2.98e-03	2.52e-03	3.24e-03	4.56e-04
74-89	1.02e-03	8.62e-04	1.06e-03	1.18e-04
89-106	3.38e-04	2.82e-04	3.73e-04	3.06e-05
106-127	1.03e-04	9.02e-05	1.17e-04	1.41e-05
127-152	2.73e-05	2.23e-05	3.03e-05	4.77e-06

Table 5.3: The calculated theoretical dijet cross section values using a renormalization scale of μ, 2μ, and 0.5μ without UE+HAD added on. The last column is the underlying event and hadronization corrections to the theoretical calculations.

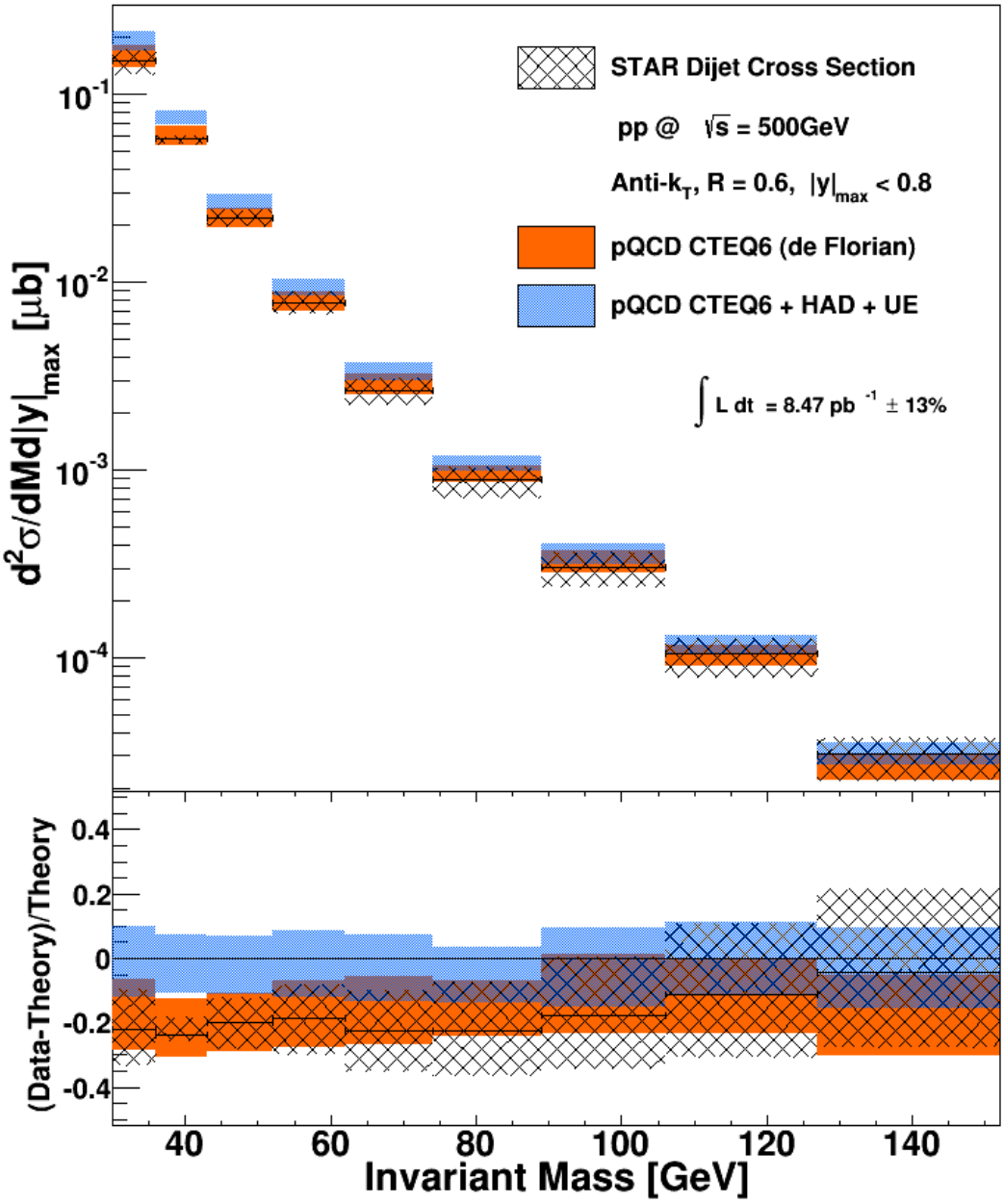

Figure 5.5: **The Dijet Cross Section** - The 2009 dijet cross section measurement for proton-proton collisions at $\sqrt{s} = 500$ GeV shown in the top panel. The bottom panel plots the ratio of the data (hashed) and the pQCD theory (orange) divided by the pQCD theory with the hadronization and underlying event corrections applied. This is not the plot used as the STAR preliminary result.

5.3 Systematic Uncertainty

Four major systematics were examined: the overall luminosity($\pm$13%), the track efficiency ($\pm$7%), track momentum resolution ($\pm$1%), and the tower energy resolution ($\pm$5%). These errors, except for the luminosity, alters the jet energy scale, which is the largest source of uncertainty in the cross section measurement. The size of the systematic errors were estimated by varying each effect by the associated uncertainty and recalculating the cross-section. Using the track momentum as an example, the momentum of each track was increased (decreased) by 1% in the embedding sample and the jet finding algorithm was run on the set of altered tracks. The difference between the new and original cross section determines the range of systematic errors. This process is repeated for the tower energy, luminosity, and track efficiency.

The track momentum systematic of 1% was conservatively estimated from the reconstructed masses of the weak decays. The two major systematics for the BEMC energy are the gain uncertainty and the status table uncertainty. In 2009 pp200 GeV data the uncertainty for the gains and status tables were 0.037 and 0.01 respectively. Added in quadrature makes the BEMC uncertainty 3.8%. In this analysis of the 500 GeV data, for a premliminary result the BEMC uncertainty was set to 5%, which was deemed very conservative approximation. In the 200 GeV inclusive jet analysis the tracking efficiency systematic used were 0%, 4%, and 7%. For this analysis 7% was used a conservative estimate based upon the results of the 200 GeV data [58]. The tracking efficiency randomly removes 7% of the tracks observed in an event to account for the difference in tracking efficiency in the data and embedding. If the embedding accurately reflects the data then it should also reflect lost tracks and this systematic corrects for tracking efficiency effects. Since it is not possible to randomly add 7% of tracks to an event, it is assumed that the systematic is symmetric. The systematics on the luminosity is described in Section 2.4.

The absolute systematic variation to the dijet cross section as a function of the dijet invariant mass is shown in Table 5.4. The first row for each invariant mass bin represents the positive variations (+1%,+5%,+7%,+13%) and the second row is the negative variation (-1%,-5%,-7%,-13%). The total systematic error is sum of all the errors added in quadrature with the exception of the luminosity. The relative change to cross-section due to each systematic uncertainty are shown in Fig 5.6. For each plot in this figure there are artificial crossing points where the relative systematic converge to zero. For the final publication we plan to vary the systematic errors, which will remove the artificial crossing point.

Mass Bin [GeV]	Track p_T	Tower E	Track Eff	Lumi	Total
23-30	-5.77e-03	-3.08e-02	-3.54e-03	-1.692e-02	3.15e-02
	-3.77e-03	4.50e-02	3.54e-03	1.69e-02	4.53e-02
30-36	-3.77e-03	-2.06e-02	-5.541e-03	-1.90e-02	2.17e-02
	-2.20e-05	2.39e-02	5.54e-03	1.90e-02	2.45e-02
36-43	-7.74e-05	-4.03e-05	-1.45e-03	-7.36e-03	1.45e-03
	8.40e-05	-4.02e-03	1.45e-03	7.36e-03	4.27e-03
43-52	2.16e-04	1.94e-03	1.05e-03	-2.76e-03	2.22e-03
	-1.37e-04	-1.92e-03	-1.05e-03	2.76e-03	2.19e-03
52-62	9.50e-05	7.28e-04	7.55e-04	-9.64e-04	1.05e-03
	-9.44e-05	-6.49e-04	-7.55e-04	9.64e-04	1.00e-03
62-74	5.85e-05	2.62e-04	3.29e-04	-3.28e-04	4.25e-04
	-4.75e-05	-2.75e-04	-3.29e-04	3.28e-04	4.31e-04
74-89	2.61e-05	9.56e-05	1.24e-04	-1.08e-04	1.59e-04
	-2.24e-05	-1.14e-04	-1.24e-04	1.08e-04	1.70e-04
89-106	9.26e-06	3.71e-05	4.76e-05	-3.77e-05	6.11e-05
	-9.81e-06	-4.55e-05	-4.76e-05	3.77e-05	6.66e-05
106-127	3.02e-06	1.39e-05	1.82e-05	-1.31e-05	2.31e-05
	-3.84e-06	-1.74e-05	-1.82e-05	1.31e-05	2.55e-05
127-152	9.01e-07	4.40e-06	5.90e-06	-4.02e-06	7.41e-06
	-1.20e-06	-5.61e-06	-5.90e-06	4.02e-06	8.23e-06

Table 5.4: The absolute systematic difference for each systematic error. The luminosity is not included in the overall total systematic. The systematic error range is determined σ_{orig} + $\delta\sigma^{sys}_{pos}$ and σ_{orig} - $\delta\sigma^{sys}_{neg}$, where $\delta\sigma^{sys}_{pos(neg)}$ is the systematic error added in quadrature with positive (negative) variations

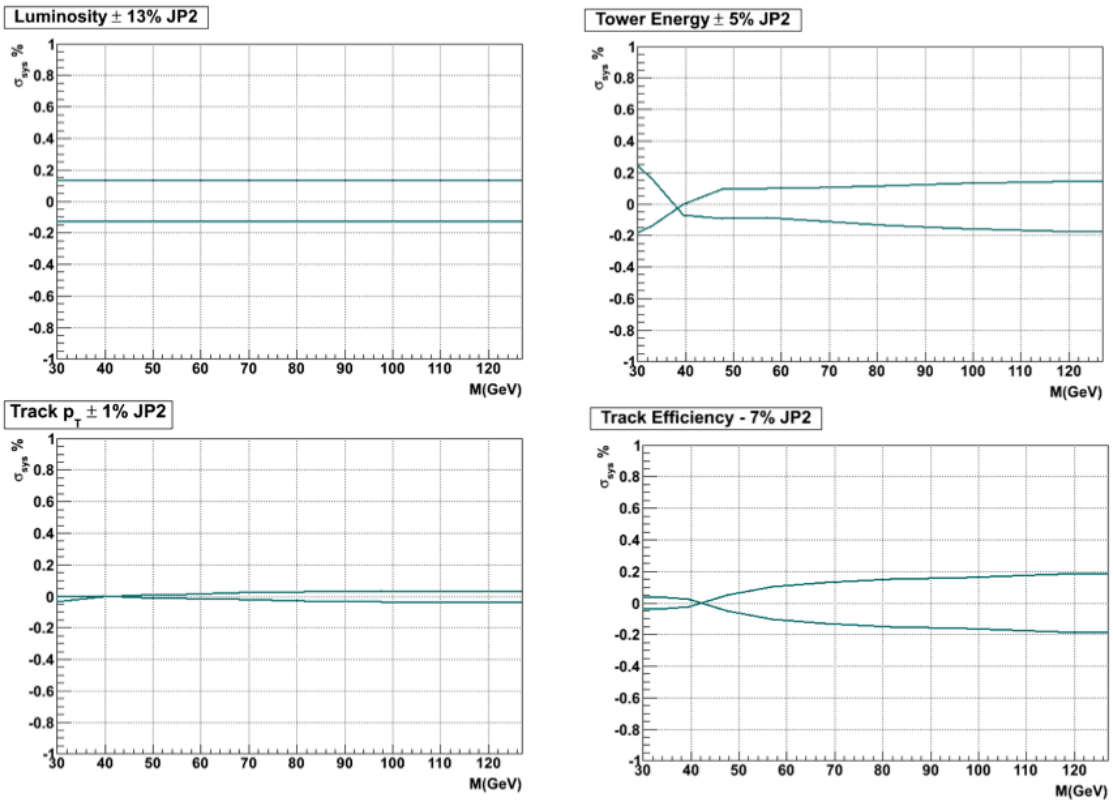

Figure 5.6: **Systematics** - The relative systematic errors on the dijet cross-section

5.4 Jetography

Chapter 3 discussed the differences between two different jet-finding algorithms, the mid-point cone and the anti-k$_T$ algorithms. This analysis deemed the anti-k$_T$ jet algorithm the optimal choice, similar to a photographer choosing the proper camera. The anti-k$_T$ algorithm needs the user to input a jet radius parameter and until now only $R = 0.6$ has been examined. This radius parameter was used in the 2009 pp 200 GeV inclusive jet analysis, which motivated the use of R=0.6 at 500 GeV . A photographer must also determine the optimal exposure time, just as a jet physicist must select the proper jet radius parameter. Therefore, the dijet cross-section analysis was actually calculated using three different radii (R=0.4, R=0.6, and R=0.8) for comparison purposes. The dijet cross-section was determined at the parton level

(before HAD and UE effects) and at the particle level (includes the non-perturbative effects) for each different jet radius. The ratio of the parton and particle level cross-sections as a function of the dijet invariant mass was calculated and is shown in Fig 5.7. At R=0.8 and R=0.6 the energy gained from the underlying event is larger than the losses from hadronization. It is evident that using a jet radius of $R = 0.4$ has a cross section ratio closer to ~ 1, balancing the two effects in such a way to minimize the correction. This means that number of particle level jets produced with the anti-k_T algorithm at R=0.4 are close to the number of parton level jets produced and therefore less sensitive to non-perturbative contributions (UE and HAD). This intuively makes sense because when increasing the center of mass energy from 200 GeV to 500 GeV jets are expected to be more collimated. Therefore, we may pursue several radii in the publication of the dijet cross section result in an effort to study underlying event and hadronization contributions.

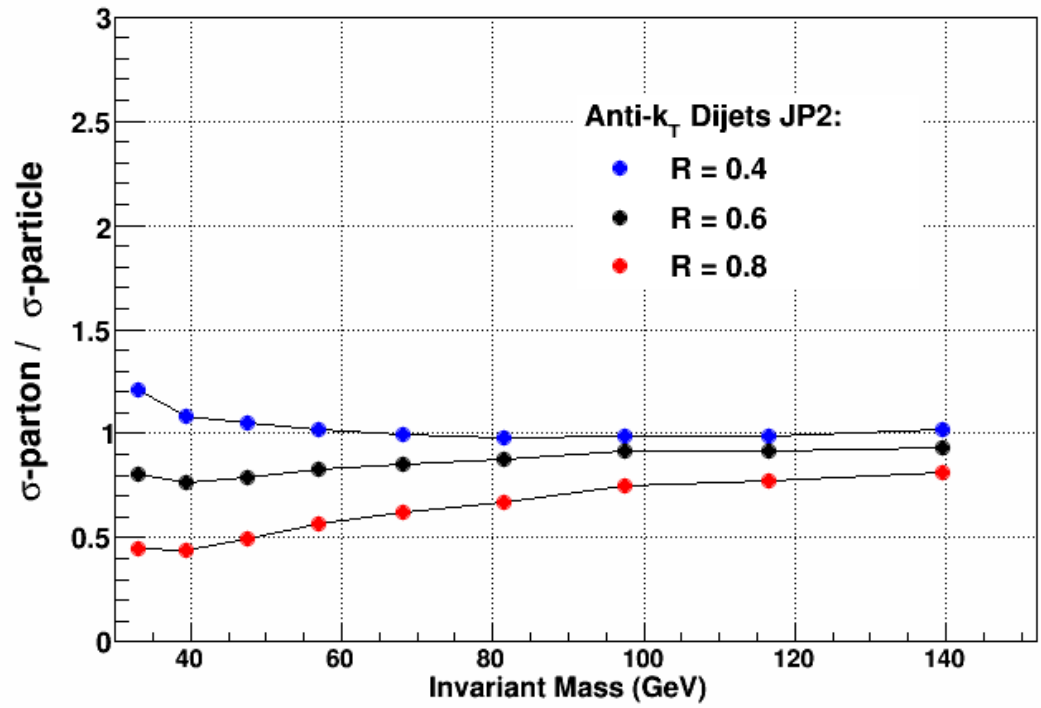

Figure 5.7: **Cross section ratio** - The comparison of the different jet radii of the anti-kT algorithm at the parton and particle levels

Chapter 6 Conclusions

Polarized deep inelastic scattering experiments have played a vital role the exploration of the spin structure of the proton. Fixed target experiments verified that the quarks of the proton are responsible for only a fraction of the spin of the proton. This discovery led to an obvious question. Where does the rest of the proton spin originate? Theorists postulated that the gluon spin and orbital motion of quarks and gluons carry the remainder of the proton's spin

The polarized proton-proton collider at RHIC provides leading order access to the gluon spin distribution through longitudinal double spin asymmetry measurements of inclusive jets, pions, and dijets. The existing jet asymmetry measurements were made at $\sqrt{s} = 200$ GeV and are sensitive to a limited range in Bjorken x (0.05-0.2). It is important to pursue measurements that are sensitive to lower x, not only because it is possible these gluons carry a substantial fraction of the proton spin, but also because the lack of constraints at low x currently drives the uncertainty on ΔG. Sensitivity to the low-x regions can be achieved by exploring measurements in the forward region and by increasing the center of mass energy of the collision at the same average jet transverse momentum.

Inclusive jet measurements provide only a lose correlation between the jet kinematics and the initial partonic kinematics. Dijets measurement, however, serve as a leading order probe to extract the initial partonic kinematics, x_1 and x_2, on an event by event basis. This will reduce the errors on the total integral ΔG by constraining the functional form used in these PDFs

In 2009 RHIC operated, for the first time, at a center of mass energy of 500 GeV, expanding the accessible x range. Spin information is experimentally extracted by fitting asymmetry measurements with theoretically driven pQCD calculations. Cross-

section measurements that are shown to agree with pQCD calculations motivate the use of this theoretical framework to interpret future asymmetry results. This thesis presents the first dijet cross section measurement in proton-proton collisions at the center of mass energy of 500 GeV/c. This result sets the stage for future asymmetry measurements at $\sqrt{s} = 500$ GeV. The measured cross-section agrees with the theoretical calculations within the experimental and theoretical systematic errors, although the theoretical calculations tend to be systematically larger by 10-20%.

Jets are a major tool in particle physics and are used to explore nature at the smallest scales, leading to a better understanding of the visible matter in the universe. As with any tool, jet reconstruction algorithms can be sharpened and honed to improve the accuracy of a measurement and possibly discover new physics. A comprehensive jet analysis was performed to determine the ideal jet algorithm and jet parameters used in $\sqrt{s} = 500$ GeV collisions at the STAR detector. Cross section measurements have been presented for dijets reconstructed with the anti-k_T algorithms using three values of the clustering parameter (R = 0.4, R = 0.6 and R= 0.8). Three different sizes of the jet clustering parameter have been used to probe the relative effects of the parton shower, hadronization, and the underlying event on the jet energy scale. The measurements have been corrected for all detector effects to the particle level so that they can be compared to any theoretical calculation.

Chapter 7 Appendix

7.1 Environment

This section describes the computational environment used to produce the embedding sample. Many of the details are quite technical and are listed here for completeness.

7.1.1 GENERAL

1. Library : SL09g
2. Geometry : y2009d

7.1.2 Starsim Settings

Pythia Version: 6.4.23 Pythia Tune: Perugia 0 accessed using PYTUNE(320)

*** Make the following stable**

MDCY (102,1)=0 ! PI0 111

MDCY (106,1)=0 ! PI+ 211

MDCY (109,1)=0 ! ETA 221

MDCY (116,1)=0 ! K+ 321

MDCY (112,1)=0 ! K_SHORT 310

MDCY (105,1)=0 ! K_LONG 130

MDCY (164,1)=0 ! LAMBDA0 3122

MDCY (167,1)=0 ! SIGMA0 3212

MDCY (162,1)=0 ! SIGMA- 3112

MDCY (169,1)=0 ! SIGMA+ 3222

MDCY (172,1)=0 ! Xi- 3312

MDCY (174,1)=0 ! Xi0 3322

MDCY (176,1)=0 ! OMEGA- 3334

7.1.3 BFC Settings

The following are the settings used in the big full chain (BFC) to reconstruct events in the detector. Since we are executing an embedded request we have three chains

Chain 1 (uses zerobias daqfiles):

`in,magF,tpcDb,NoDefault,TpxRaw,-ittf,NoOutput`

Chain 2 (uses fzd files):

`fzin,gen_T,geomT,sim_T,TpcRS,-ittf,-tpc_daq,nodefault ry2009d`

Chain 3 (creates embedded MuDst files): `DbV20101215 OGGVoltErr pp2009c ITTF VFPPVnoCTB BEmcChkStat beamLine Corr4 OSpaceZ2 OGridLeak3D -dstout -evout TpxClu -VFMinuit VFPPVnoCTB beamLine -hitfilt, Embedding,TpcMixer,GeantOut, MiniMcMk,McAna,-in,NoInput,useInTracker, nodefault, emcSim,EEfs,EEss`

In short, running the BFC code using these parameters embeds the simulated response into a randomly triggered data sample. The zerobias sample then properly estimates the backgrounds in the STAR detector.

7.2 Error Calculations

Any measurement is useless without an error associated with it. Every experiment posses some imperfections and we need to know how well can make a measurement.

An error provides this crucial information.

$$A = B + C \tag{7.1}$$

then

$$(\delta A)^2 = (\delta B)^2 + (\delta C)^2 \tag{7.2}$$

Similarly if

$$A = \frac{B}{C} \tag{7.3}$$

then

$$\left(\frac{\delta A}{A}\right)^2 = \left(\frac{\delta B}{B}\right)^2 + \left(\frac{\delta C}{C}\right)^2 \tag{7.4}$$

7.2.1 Errors on an Inefficiencies

The previous section is based upon the assumption that the numerator and denominator of the division are completely uncorrelated. Complications arise when ones considers the effects of their correlations. Namely when one deals with inefficiencies and the numerator is a complete subset of the denominator or in other words a 100% correlation. To prevent confusion from our previous example we will use different variable names $u = x/z$. The standard method to calculated this error of an inefficiency is described by the following:

$$\left(\frac{\sigma_u}{u}\right)^2 = \left(\frac{\sigma_x}{x}\right)^2 + \left(\frac{\sigma_z}{z}\right)^2 - 2\frac{\mathrm{cov}(x,y)}{xy} \tag{7.5}$$

where the third term accounts for the relationship between the quantities by calculating their covariance $\mathrm{cov}(x,z)$. reference Leo!!!

However, there is a useful trick when dealing with errors of inefficiencies, which makes the calculation simpler. This section will detail the derivation of this helpful trick. We ascertain that the numerator, x, is correlated to the denominator, z, in such a way that values of x satisfy some particular requirement of the full data z.

There also exists events within the data that doesn't meet this condition, we call it this y. Therefore, $z = x + y$ and x and y are uncorrelated with each other and we have

$$u = \frac{x}{z} = \frac{x}{x+y} \tag{7.6}$$

which allows us to calculate the error in the standard method of combining the relative errors.

$$\sigma_u^2 = \left(\frac{\partial u}{\partial x}\right)^2 \sigma_x^2 + \left(\frac{\partial u}{\partial y}\right)^2 \sigma_y^2 \tag{7.7}$$

The simple derivatives are calculated using the quotient rule

$$\left(\frac{\partial u}{\partial x}\right) = \frac{\partial}{\partial x}\left(\frac{x}{x+y}\right) = \frac{(x+y)(1) - x}{(x+y)^2} = \frac{y}{(x+y)^2} \tag{7.8}$$

$$\left(\frac{\partial u}{\partial y}\right) = \frac{\partial}{\partial y}\left(\frac{x}{x+y}\right) = \frac{(x+y)(0) - x}{(x+y)^2} = \frac{-x}{(x+y)^2} \tag{7.9}$$

subbing this back into equation 7.7 and using $\sigma_x = \sqrt{x}$ and $\sigma_y = \sqrt{y}$ we get

$$\sigma_u^2 = \left(\frac{y}{(x+y)^2}\right)^2 x + \left(\frac{-x}{(x+y)^2}\right)^2 y \tag{7.10}$$

which can be re-written as

$$\sigma_u = u^2\sqrt{\frac{y^2}{x^3} + \frac{1}{x^2}} = \frac{u^2}{x}\sqrt{1 + \frac{y^2}{x}} \tag{7.11}$$

Bibliography

[1] J. Beringer *et al.*, "Review of Particle Physics (RPP)," *Phys.Rev.*, vol. D86, p. 010001, 2012.

[2] J. A. *et al.*, "Particle data group," *Phys.Rev.*, vol. D86 010001, 2012.

[3] E. D. Bloom, D. H. Coward, H. DeStaebler, J. Drees, G. Miller, L. W. Mo, R. E. Taylor, M. Breidenbach, J. I. Friedman, G. C. Hartmann, and H. W. Kendall, "High-energy inelastic $e - p$ scattering at 6° and 10°," *Phys. Rev. Lett.*, vol. 23, pp. 930–934, Oct 1969.

[4] W. Hofmann, "The physics of jets," *Nuclear Physics B - Proceedings Supplements*, vol. 3, no. 0, pp. 671 – 713, 1988.

[5] S. Ellis, J. Huston, K. Hatakeyama, P. Loch, and M. Tnnesmann, "Jets in hadron-hadron collisions," *Progress in Particle and Nuclear Physics*, vol. 60, no. 2, pp. 484 – 551, 2008.

[6] J. Ellis, M. K. Gaillard, and G. G. Ross, "Search for gluons in e+e− annihilation," *Nuclear Physics B*, vol. 111, no. 2, pp. 253 – 271, 1976.

[7] R. D. Field, "The Underlying event in hard scattering processes," *eConf*, vol. C010630, p. P501, 2001.

[8] G. Altarelli and G. Parisi, "Asymptotic Freedom in Parton Language," *Nucl.Phys.*, vol. B126, p. 298, 1977.

[9] J. Pumplin, D. Stump, J. Huston, H. Lai, P. M. Nadolsky, *et al.*, "New generation of parton distributions with uncertainties from global QCD analysis," *JHEP*, vol. 0207, p. 012, 2002.

[10] J. Owens, A. Accardi, and W. Melnitchouk, "Global parton distributions with nuclear and finite-Q^2 corrections," *Phys.Rev.*, vol. D87, no. 9, p. 094012, 2013.

[11] A. Martin, W. Stirling, R. Thorne, and G. Watt, "Update of parton distributions at NNLO," *Phys.Lett.*, vol. B652, pp. 292–299, 2007.

[12] A. Cooper-Sarkar, "PDF Fits at HERA," *PoS*, vol. EPS-HEP2011, p. 320, 2011.

[13] F. Halzen and A. D. Martin, *QUARKS AND LEPTONS: AN INTRODUCTORY COURSE IN MODERN PARTICLE PHYSICS*. New York, USA: Wiley, 1984.

[14] G. Altarelli, "Collider Physics within the Standard Model: a Primer," 2013.

[15] J. Gao, M. Guzzi, J. Huston, H.-L. Lai, Z. Li, *et al.*, "The CT10 NNLO Global Analysis of QCD," 2013.

[16] M. e. a. Derrick, "Extraction of the gluon density of the proton at smallx," *Phys.Lett.*, vol. B345, pp. 576–588, 1995.

[17] A. Deur, "private communication," 2014.

[18] D. de Florian, R. Sassot, M. Stratmann, and W. Vogelsang, "Extraction of spin-dependent parton densities and their uncertainties," *Phys. Rev. D*, vol. 80, p. 034030, Aug 2009.

[19] J. A. t. European Muon Collaboration, "A Measurement of the Spin Asymmetry and Determination of the Structure Function g_1 in Deep Inelastic Muon-Proton Scattering," *Phys. Lett. B206*, 1988.

[20] E. Leader, A. V. Sidorov, and D. B. Stamenov, "Determination of Polarized PDFs from a QCD Analysis of Inclusive and Semi-inclusive Deep Inelastic Scattering Data," *Phys.Rev.*, vol. D82, p. 114018, 2010.

[21] J. Blumlein and H. Bottcher, "QCD analysis of polarized deep inelastic scattering data," *AIP Conf.Proc.*, vol. 602, pp. 94–99, 2001.

[22] T. Sakuma and M. Walker, "Dijet Cross Section and Longitudinal Double Spin Asymmetry Measurements in Polarized Proton-proton Collisions at $\sqrt{s}$ =200 GeV at STAR," *J.Phys.Conf.Ser.*, vol. 295, p. 012068, 2011.

[23] P. Djawotho, "Gluon polarization measurements with inclusive jets at STAR," 2011.

[24] E. Aschenauer, A. Bazilevsky, K. Boyle, K. Eyser, R. Fatemi, *et al.*, "The RHIC Spin Program: Achievements and Future Opportunities," 2013.

[25] A. *et* al.. I, "Polarized proton collider at RHIC," *Nucl. Instrum. Meth. A499 392-414.*, 2003.

[26] Z. *et* al.. A, "Optically pumped polarized H^- ion source for RHIC spin physics," *Rev. Sci. Instrum. 73, 888*, 2002.

[27] L. *et* al.. A, "Polarized proton beam acceleration with a Single Siberian Snake in each RHIC ring," 2000.

[28] Jinnouchi, O. and Alekseev, I.G. and Bravar, A. and Bunce, G. and Dhawan, S. and others, "Measurement of the analyzing power of proton-carbon elastic scattering in the CNI region at RHIC," pp. 515–518, 2004.

[29] K. Kurita, "Commissioning of RHIC pC CNI polarimeter," *Nuclear Physics A*, vol. 721, no. 0, pp. C356 – C359, 2003.

[30] H. Okada, I. Alekseev, A. Bravar, G. Bunce, S. Dhawan, *et al.*, "Measurement of the analyzing power A(N) in pp elastic scattering in the CNI region with a polarized atomic hydrogen gas jet target," 2006.

[31] Z. *et* al.. A, "Absolute polarized H-jet polarimeter development, for RHIC," *Nucl. Instr. and Meth. in Phys. Res A536 248-254*, 2005.

[32] M. A. *et al.*, "The STAR time projection chamber: A unique tool for studying high multiplicity events at RHIC," *Nucl. Instrum. Meth. A499*, 2003.

[33] W. Llope, F. Geurts, J. Mitchell, Z. Liu, N. Adams, *et al.*, "The TOFp / pVPD time-of-flight system for STAR," *Nucl.Instrum.Meth.*, vol. A522, pp. 252–273, 2004.

[34] F. B. C. B. *et al.*, "The star detector magnet subsystem," *Nuclear Instruments and Methods in Physics Research Section A: Accelerators, Spectrometers, Detectors and Associated Equipment*, vol. 499, pp. 633 – 639, 2003.

[35] M. B. t. STAR Collaboration, "The STAR barrel electromagnetic calorimeter," *Nucl. Instrum. Meth. A499 725-739*, 2003.

[36] C. Allgower *et al.*, "The STAR endcap electromagnetic calorimeter," *Nucl.Instrum.Meth.*, vol. A499, pp. 740–750, 2003.

[37] J. Kiryluk, "Local polarimetry for proton beams with the STAR beam beam counters," pp. 718–721, 2005.

[38] C. Adler, A. Denisov, E. Garcia, M. J. Murray, H. Strobele, *et al.*, "The RHIC zero degree calorimeter," *Nucl.Instrum.Meth.*, vol. A470, pp. 488–499, 2001.

[39] G. V. B. *et al.*, "Correcting for distortions due to ionization in the STAR TPC," *Nucl. Instrum. Meth. A 566 22-25*, 2006.

[40] F. B. H. C. *et al.*, "The STAR trigger," *Nuclear Instruments and Methods in Physics Research Section A: Accelerators, Spectrometers, Detectors and Associated Equipment*, vol. 499, pp. 766 – 777, 2003.

[41] A. Drees and S. White, "Vernier Scan Results from the First RHIC Proton Run at 250 GeV," *Conf.Proc.*, vol. C100523, p. MOPEC013, 2010.

[42] P. C. *et al.*, "The RHIC Wall Current Monitor System," *Proceedings of the 1999 PAC*, 1999.

[43] R. Corliss, "Measurement of absolute luminosity for STAR BHT3 trigger for p + p collisions at a center of mass of 500 GeV in 2009," *Internal STAR Note*, no. 533, 2009.

[44] L. Adamczyk *et al.*, "Measurement of the $W \to e\nu$ and $Z/\gamma^* \to e^+e^-$ Production Cross Sections at Mid-rapidity in Proton-Proton Collisions at $\sqrt{s} = 500$ GeV," *Phys.Rev.*, vol. D85, p. 092010, 2012.

[45] G. P. S. M. Cacciari and G. Soyez, "The anti-kt jet clustering algorithm," *JHEP **0**804, 063 (2008) [arXiv:0802.1189 [hep-ph]]*, 2008.

[46] G. C. Blazey, J. R. Dittmann, S. D. Ellis, V. D. Elvira, K. Frame, *et al.*, "Run II jet physics," pp. 47–77, 2000.

[47] G. P. S. M. Cacciari and G. Soyez, "FastJet 2.4.1 user manual," *Phys. Lett. B* ***641:57***, 2006.

[48] G. Soyez, "The SISCone and anti-k(t) jet algorithms," p. 178, 2008.

[49] T. Sjostrand, S. Mrenna, and P. Z. Skands, "PYTHIA 6.4 Physics and Manual," *JHEP*, vol. 0605, p. 026, 2006.

[50] P. Djawotho, "Comparison of STAR midpoint cone, CDF midpoint cone, kt and anti-kt jet algorithms," 2012.

[51] S. Agostinelli *et al.*, "GEANT4: A Simulation toolkit," *Nucl.Instrum.Meth.*, vol. A506, pp. 250–303, 2003.

[52] A. Hocker and V. Kartvelishvili, "SVD approach to data unfolding," *Nucl.Instrum.Meth.*, vol. A372, pp. 469–481, 1996.

[53] T. Adye, "Unfolding algorithms and tests using RooUnfold," 2011.

[54] G. Choudalakis, "Unfolding in ATLAS," *arXiv:1104.2962*, 2011.

[55] R. M. S. M. R. Walpole and K. Ye, "Probability and Statistics for Engineers and Scientists -8th ed.," *Pearson Prentice Hall, ISBN 0-13-187711-9*, 2007.

[56] G. D'Agostini, "A Multidimensional Unfolding Method Based on Bayes Theorem ," *Nucl. Instr. and Meth. in Phys. Res. A362*, 1995.

[57] D. de Florian, "Personal Communications,"

[58] P.Djawotho, "2009 inclusive jet double-helicity asymmetry $a_l l$ in polarized p+p collisions at $\sqrt{s} = 200$ gev analysis note version 1.4.1," *Internal STAR Note*, no. PSN0573, 2013.

VITA

Grant D. Webb

Place of Birth:

Eubank, KY
July 8, 1985

Education:

University of Kentucky
Lexington, KY
M.S., Physics
May 2010

Morehead State University
Morehead, KY
B.S., Physics
May 2007

Professional Positions:

University of Kentucky
Research Assistant
December 2007 - Present

University of Kentucky
Teaching Assistant
August 2007 - December 2007

Morehead State University
Research Assitant
August 2006 - July 2007

Publications:

"The Dijet Cross Section Measurement in Proton-Proton Collsions at $\sqrt{s} = 500$ GeV", G. Webb, *PoS*, *DIS2013*, 215, 2013